UNIVERSITÀ
DEGLI STUDI
DI BRESCIA

DOTTORATO DI RICERCA IN

Technology for Health

settore scientifico disciplinare

ING-IND/22 SCIENZA E TECNOLOGIA DEI MATERIALI

CICLO

XXXIII

3D Printed Shape Memory Polymers for Biomedical Applications

Candidato: Nicoletta Inverardi

Relatore: Prof. Stefano Pandini

Esame Finale Anno Accademico 2019/2020

Abstract

Shape memory polymers (SMPs) are stimulus-responsive materials capable of changing their shape in a programmed fashion under the application of an external stimulus. Their shape-shifting feature may allow the achievement of peculiar functionalities in an autonomous and untethered way, that is of utmost importance for several challenging applications in which external and non-mechanical actuation of a device is desirable, ranging from soft robotics to the biomedical field. Furthermore, the growing importance and employment of additive manufacturing techniques has enabled new design flexibility opening new exciting opportunities for SMPs. In fact, the possibility of processing SMPs by 3D printing can broaden and extend their scope and applicability by allowing to obtain more complex and structured shape changes and/or personalized medical devices with tailorable and patient-specific dimensions and geometries. This novel technological platform is widely recognized to hold great potential in the biomedical field. It is considered to be greatly promising in the pharmaceutical and drug delivery fields, however relevant applications have yet to be demonstrated. Therefore, in this thesis a thorough investigation on the shape memory effect and time-dependent actuation mechanisms was performed with specific attention to applications of 3D printed devices in the pharmaceutical field. First, an in-depth experimental campaign was carried out on photo-curable polymeric resins for stereolithography 3D printing. Based on material properties and thermo-mechanical protocols, it was possible to design a non-conventional shape memory response. Self-locking and self-folding structures were thus obtained, which are potentially useful for the development of novel medical devices such as stents. Next, a biocompatible shape memory effect was designed starting from polymers of pharmaceutical grade that can be processed by hot-melt extrusion and FDM (fused deposition modeling) 3D printing. Particular attention was devoted to the design and characterization of a triggering stimulus resulting from the synergistic action of the exposure to moisture and heat, which are compatible with physiological conditions. By designing the shape memory effect and the shape evolutions occurring over time, a retentive device for the treatment of bladder diseases and a gastroretentive drug delivery device were conceived as proof-of-concept prototypes. Finally, a capsule-sized device for long-term engagement with the gastrointestinal tract was designed to be completely autonomous, relying on a hydration- and time-dependent actuator. This gastric resident system may be used in future as an anchor for drug depots and/or sensors for long-term drug release and sensing applications.

Riassunto

I polimeri a memoria di forma sono materiali sensibili a stimoli esterni, in grado di cambiare la loro forma in maniera programmata a seguito dell'applicazione di uno stimolo esterno. La loro capacità di cambiare forma può permettere l'ottenimento di specifiche funzionalità in modo autonomo e da remoto, e ciò è di estrema importanza per diverse applicazioni complesse in cui un'attuazione esterna e non meccanica di un dispositivo è vantaggiosa, nel campo della robotica soft e nel biomedicale. Inoltre, la crescente importanza ed impiego di tecniche di manifattura additiva ha permesso una nuova flessibilità nella progettazione garantendo nuove opportunità interessanti per i polimeri a memoria di forma. Infatti, la possibilità di processare i polimeri a memoria di forma attraverso la stampa 3D può allargare ed estendere il loro ambito e rilevanza permettendo di ottenere cambiamenti di forma più complessi e strutturati e/o dispositivi medici personalizzati con dimensioni e geometrie specifiche e aggiustabili per ogni paziente. Questa nuova piattaforma tecnologica è ampiamente riconosciuta avere un grande potenziale nel campo biomedico. È considerata molto promettente nel campo farmaceutico e del rilascio di farmaci, tuttavia relative applicazioni devono ancora essere dimostrate. Di conseguenza, in questa tesi è stato effettuato un meticoloso studio dell'effetto di memoria di forma e di meccanismi di attuazione dipendenti dal tempo con specifica attenzione verso applicazioni di dispositivi ottenuti attraverso stampa 3D nel campo farmaceutico. In primo luogo, una campagna sperimentale approfondita è stata condotta su resine polimeriche fotocurabili per stampa 3D tramite stereolitografia. Sulla base delle proprietà del materiale e di protocolli termo-meccanici, è stato possibile progettare una risposta a memoria di forma non convenzionale. Strutture auto-chiudenti e auto-ripieganti sono state così ottenute, potenzialmente utili per lo sviluppo di nuovi dispositivi medici quali stents. Successivamente, un effetto a memoria di forma biocompatibile è stato progettato partendo da polimeri di grado farmaceutico che possono essere processati tramite estrusione e stampa 3D per FDM (fused deposition modeling). Speciale attenzione è stata data alla progettazione e caratterizzazione di uno stimolo di attuazione risultante dall'azione sinergica dell'esposizione a umidità e calore, compatibile con condizioni fisiologiche. Grazie alla progettazione dei cambiamenti di forma da compiersi nel tempo, sono state ideati un dispositivo ritentivo per il trattamento di patologie riguardanti la vescica e un dispositivo gastroritentivo per il rilascio di farmaci come prototipi "proof-of-concept".

Infine, un dispositivo dalle dimensioni standard di capsula è stato progettato per ancorare il tessuto gastrointestinale in modo da essere completamente autonomo, affidandosi ad un attuatore con meccanismo di idratazione dipendete dal tempo. Questo sistema potrà essere usato in futuro come un sistema di ancoraggio per depositi di farmaci e/o per sensori per applicazioni di rilascio di farmaco e di monitoraggio tramite sensori, a lungo termine.

Acknowledgments

I would like to sincerely thank my advisor Prof. Stefano Pandini for his encouragement to pursue PhD studies, for the time devoted to my project and for teaching me how to thoroughly carry out scientific research. Thank you for all the discussions and knowledge shared with me on shape memory polymers. My gratitude also goes to my tutor Prof. Fabio Bignotti for representing me in the Technology for Health PhD School and for giving me precious insights on biomaterials and polymer chemistry. I also would like to thank all the members of the Materials Science and Technology Laboratory at the University of Brescia, past and present. In particular, thank you to Isabella Peroni and Gloria Spagnoli for your kindness, continuous support and technical assistance, to Dr. Kamol Dey for sharing with me the PhD journey always with a smile and to some hardworking undergraduate students, Marica Bianchi, Romualdo Raus, Daniel Straub and Giulia Tameni, that have assisted me in some of the work included in this thesis.

I would like to express my deepest gratitude to Prof. Robert Langer and Prof. Giovanni Traverso for giving me the fantastic chance to join their groups at the Massachusetts Institute of Technology and for making me feel an integral member of their research teams. Furthermore, many thanks to Prof. Traverso for his inspired mentorship, for the trust given to me and for always finding time to support me. His energy and creativity have always pushed me to do my best and I will treasure this for my future. I also wish to sincerely thank Dr. Sahab Babaee for being a reference point for me at MIT and for his precious help, for letting me free to experiment under his wise guidance and for broadening my horizons on new research fields. I would like to thank all the group members for precious discussions, support and for contributing to make the Langer and Traverso labs such unique and amazing places to perform research. I am especially thankful to Declan Gwynne, Grace Ingalls, Dr. Ameya Kirtane, Dr. Ying Li, Dr. Gary Liu, Seokkee Min, Dr. Jan-Georg Rosenboom, Jacob Wainer, Adam Wentworth, the Animal Team and the Gates Team for all the insightful discussions, advices and collaboration. The support of the Bill and Melinda Gates Foundation is also kindly acknowledged. I also wish to thank the Technology for Health PhD School and the Academic Board for supporting my research experience abroad.

I sincerely thank all of the members of the other research teams who have contributed to the work here presented by enriching it and by creating a collaborative and valuable interdisciplinary approach. Many thanks

to the Biopharmaceutics and Pharmaceutical Technology Laboratory of the University of Milano, in particular to Dr. Alice Melocchi, Marco Uboldi, Prof. Alessandra Maroni, Prof. Lucia Zema and Prof. Andrea Gazzaniga for his vision and for believing in the collaboration with engineers. Many thanks to the Computational Mechanics and Advanced Materials group of the University of Pavia, in particular to Dr. Giulia Scalet, Dr. Stefania Marconi and Prof. Ferdinando Auricchio for his encouragement, constant availability, experience and precise and significant suggestions.

To Alice and Giulia: you truly are role models and source of inspiration for my future career; thanks for your endless support.

Special thanks also to Prof. Francesco Baldi (University of Brescia) and Prof. Francesco Briatico-Vangosa (Politecnico di Milano) for their help in deeper understanding some concepts in the polymer science field, to Prof. Massimo Messori (University of Modena and Reggio Emilia) and Prof. Maurizio Toselli (University of Bologna) for interesting discussions on 3D printing and polymer chemistry, to Dr. Silvia Agnelli and Prof. Luciana Sartore (University of Brescia) for allowing me to be part of some of their projects on soft polymeric materials for tissue regeneration, and to Dr. Davide Battini (University of Brescia) for his precious help in developing some characterization methods described in this thesis.

Finally, most importantly, I am extremely grateful to my parents, Liliana and Fabrizio, for always being at my side, teaching me to always follow my dreams with their endless support and love.

Table of contents

Chapter 5

Chapter 1

Introduction

Shape memory polymers are smart materials capable of large shape changes under the application of an external, non-mechanical stimulus, and upon properly developed thermo-mechanical histories. More in details, in the most known "one-way" shape memory effect, they can be deformed into a temporary shape which can be maintained unaltered without any applied constraints until the application of an external stimulus triggers the recovery of the permanent shape[1,2]. By way of example, in Figure 1.1 one of the first demonstration of the shape memory effect in a poly(ε-caprolactone) dimethacrylate polymer network, as proposed by Lendlein and Langer[3], is presented.

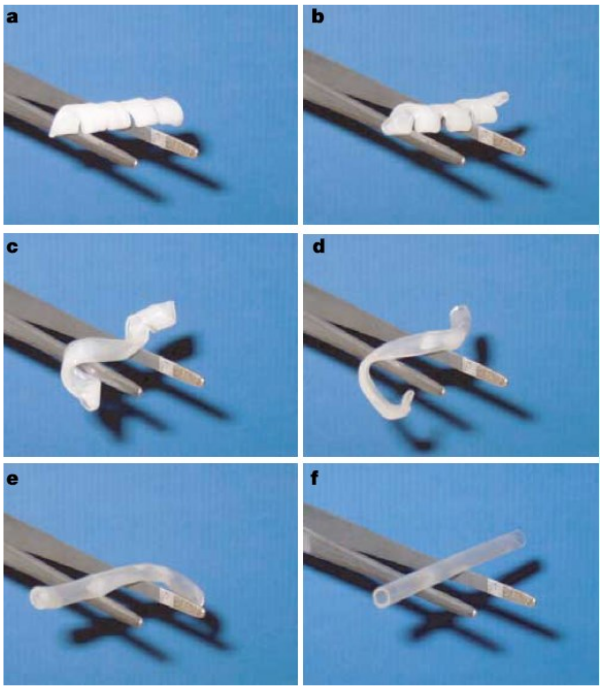

Figure 1.1. Sequence of shape recovery performed at 50 °C in 10 s from the temporary flat helix to the permanent tube geometry[3].

The external stimulus can be of different nature, according to the chemistry of the material, and it usually involves the exposure of the material to either direct or indirect heat, to solvents, to difference in pH or to light.

During the recovery process, if the temporary shape is kept constrained while applying the triggering stimulus, it is possible to obtain the generation of stress. In fact, the material, which would recover its permanent shape under strain-free conditions, is forced in its temporary shape and its deformations are hindered; thus stresses can be produced, and they can be rationally leveraged in specific applications, for example to expand a blood vessel, in the case of cardiovascular stents.

The shape memory effect can be explained as a consequence of the viscoelastic behavior and of the entropic elasticity of polymer chains in the rubber state. Therefore, it can be obtained by a rational use of thermomechanical cycles exploiting the different macromolecular mobility characterizing polymers in different states. In particular, cooling steps can be used to fix a temporary shape and heating steps to activate the shape memory response at specific transition temperatures which depend on the structure of the material. In fact, the shape memory effect is optimized for those structures in which so-called "soft domains" coexist with "hard domains". The former ones can be considered as the thermal switchers of polymeric chain mobility, whose transition temperature T_{sw} enables the deformation and subsequent fixity of a temporary shape. These can be represented by a crystalline phase which upon melting/crystallization gain/lose mobility or likewise by amorphous chain undergoing the glass transition. Conversely, the hard domains consist of either physical or chemical crosslinking points, that prevent the flow of polymeric chains, ensuring in this way the recovery of the permanent shape[4]. In order to exploit and characterize the effect, a thermomechanical cycle based on the characteristic temperatures and structure of the material has to be designed. A typical cycle involves a first step, called "programming" in which a material specimen is heated above its transition temperature, a deformation is applied and cooling under the applied deformation is performed to fix the temporary shape. This is followed by unloading and by the recovery stage traditionally initiated by heating above the transition temperature. To do so, at the same time stresses, deformations, and temperatures have to be monitored and the gold standard is represented by the use of the dynamic mechanical analyzer.

Shape memory polymers have been known from decades, but recently they received renewed attention thanks to the advent of 4D printing. Indeed, 4D printing stems from the application of additive manufacturing technologies to smart active materials, thus enabling a dynamic active, usually complex sequential shape change of the 3D printed material over time, which is considered as the fourth dimension[5]. One of the possible approach to incorporate a time-dependent behavior in 3D printed parts consists in using responsive hydrogels which can reversibly swell or shrink according to environmental conditions such as temperature or pH value. The term 4D printing was in fact coined in 2014 by Skylar Tibbits, the founder of the Self-Assembly Lab at MIT, by developing novel self-folding structures, as the one shown in Figure 1.2, exploiting the different swelling behavior of multiple 3D printed materials[6,7].

Figure 1.2. Example of a 2D-to-3D self-folding process, designed at the Self-Assembly Lab (MIT)[7].

Alternatively, it is possible to employ shape memory polymers to provide the 3D printed part with a programmable shape change over time. The key point is that both the temporary shape and the permanent one, as well as the triggering mechanisms, can be arbitrarily designed and governed through the material structure and the manufacturing conditions. Since 2013, the research groups led by Jerry Qi, Martin Dunn and Qi Ge reported the achievement of several different shape-shifting designs by starting from a multimaterial 3D printing approach involving different thermoset materials to be carefully deposited at specific locations so as to create active hinges to enable origami folding patterns or to control sequential self-folding structures[8-10].

Therefore, the applications of shape memory polymers can be wider and more promising if processed by 3D printing to obtain stimuli responsive devices, with complex and customized geometries. In fact one of the great advantages of using additive manufacturing techniques concerns the possibility of obtaining more complicated shape transformations than those traditionally studied until now for shape memory polymers. With specific interest for the biomedical field, it would be possible to obtain biomedical devices perfectly fitting the patient's "dimensions": by taking anatomical information, *e.g.* through computerized tomography (CT) scan and/or magnetic resonance imaging (MRI), a custom-tailored device can be prepared.

1.1 Applications of 3D printed shape memory polymers in the biomedical field

Shape memory polymers have been widely employed in the biomedical field, due to their capability to be stored and delivered to the patient in a temporary compact shape and to revert, as a consequence of the application of a triggering stimulus, to a deployed permanent shape, which should be functional to a specific need[2]. They have mainly been proposed and patented for the development of medical devices for minimally-invasive surgery, *e.g.* self-tightening sutures[11,12], self-expandable biodegradable stents[13], thrombectomy devices[14] and embolization plugs[15-18].

In the following paragraphs, their employment for additive manufacturing techniques is described, with particular attention to the cases of the design of new biomedical devices, the development of scaffolds and bio-manufactured grafts for tissue engineering and tissue repair applications and their prospective applications in the pharmaceutical field.

Medical devices

The employment of smart active materials and 3D printing techniques can be of tremendous impact for the design of customized and patient-specific medical devices. One of the clearest examples is represented by the case of stents, *i.e.* tubular devices, often characterized by a wire-mesh geometry, used to treat stenosis (abnormal narrowing of a tubular organ) in different fields such as for cardiovascular applications, for the management of tracheobronchial and ureteral obstructions and for pathologies affecting the esophageal and gastrointestinal tract[19]. In fact, 3D printing could be beneficial in order to obtain complex geometries and geometry evolutions, which otherwise would require multiple, complex and time-consuming manufacturing steps in the case of traditional subtractive manufacturing methods[20]. Furthermore, the use of shape memory polymers as a base material of the stent might add a programmed time-dependent shape-shifting response which could be advantageous for the device placement, by delivering the stent in a compact shape suitable for minimally invasive procedures, and for the device management, such as in order to avoid the issue of stent migration[19]. From a manufacturing perspective, in 2016 Ge *et al.*[20] described one of the first approaches to obtain programmable stents that can be deformed in a compressed temporary state in which the strain field is

characterized by local large deformations. They showed as a proof-of-concept the fabrication of various wire-mesh stents varying the number of joints, the diameter of the ligaments and the angle between them, by employing a high resolution projection microstereolithography technique. The size scale was in the order of cm, with the diameter of the stent equal to approximately 5 mm and the minimum features of 200 μm, as shown in Figure 1.3a. Further improvements led to the fabrication of shape memory polymer-based stents also at the microscale, as reported by de Marco and co-authors[21], with minimum features of 5 μm, as illustrated in Figure 1.3b.

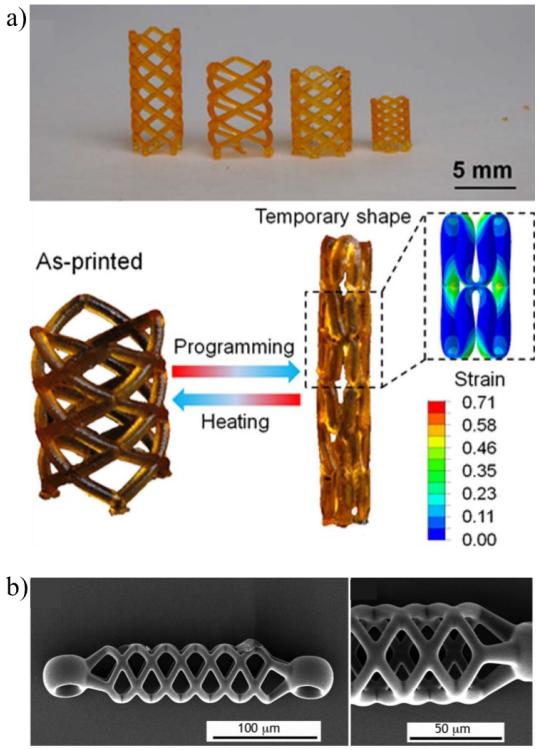

Figure 1.3. Prototypes of stents obtained by 4D printing with minimum features a) of 200 μm[20] and b) of 5 μm[21].

Meanwhile, advances in materials research allowed to obtain inks for 3D printing resulting in highly stretchable (up to 600%) shape memory materials[22], overcoming one of the commonly found issues in using photocrosslinkable resins which, upon printing and curing, result in a highly crosslinked network and thus in a brittle behavior. Furthermore, the achievement of such flexible and soft shape memory polymers could be beneficial for applications at the interface with soft tissues, as in the case of wearable and biomedical devices. With respect to the application scenario, there is still room for

improvements and demonstration of the translational capability of shape memory polymer-based biomedical devices. An impactful application was introduced for the treatment of pediatric tracheobronchomalacia (TBC), a conditions characterized by an excessive collapse of the airways during respiration, for which, in its most severe form, no adequate intervention is available. A patient-specific tracheobronchial splint was designed and manufactured using polycaprolactone (PCL), which thanks to its expansion *in vivo* helped in accommodating the natural tissue growth while degrading over time and resulting in the resolution of life-threatening complications for 3 pediatric patients with severe TBC[23]. Moving to studies less focused on the translationability and approached from a materials science perspective, a thorough shape memory characterization for an *ad hoc* synthesized PCL-based resin was conducted by Zarek *et al*.[24]. They used their material platform to develop a prototype for a tracheal stent which potentially can overcome the issue of stent migration by exploiting the shape expansion of the device occurring after thermal activation of the recovery. An alternative solution for a 4D printed tracheal stent involved an indirect Curie-regulated heat-driven actuation promoted by the exposure of the shape memory material including magnetic fillers to an alternating magnetic field leading to the generation of heat inside the material[25]. As previously mentioned, the working concept presented for the aforementioned tracheal stents may be useful also for other areas of treatment, as in the case of cardiovascular diseases. Self- expandable prototypal vascular stents based on the shape memory effect are also being investigated[26,27], however the translation to clinical practice is for now still far and limited, due to the manifold challenges to be faced, mainly related to the achievement of robust mechanical properties, needed to assure reliability and safety of such a critical component.

Tissue engineering and biomanufacturing

More recently with respect to the field pertaining to the development of medical devices, shape memory polymers have been exploited also for tissue engineering and biomanufacturing in order to obtain self-deploying grafts[28,29] and to provide dynamic electrospun scaffolds for cell culture with a topological control based on the shape evolution of the substrate[30-32].

One of the first examples towards 4D bioprinting regarded a biomimetic printing approach, proposed in 2016 by the Lewis group[33]. They used a purposely developed hydrogel ink to target bio-inspired shape-morphing sequences, as shown in Figure 1.4, actuated by anisotropic swelling deriving from the orientation of cellulose fibrils within the printed material.

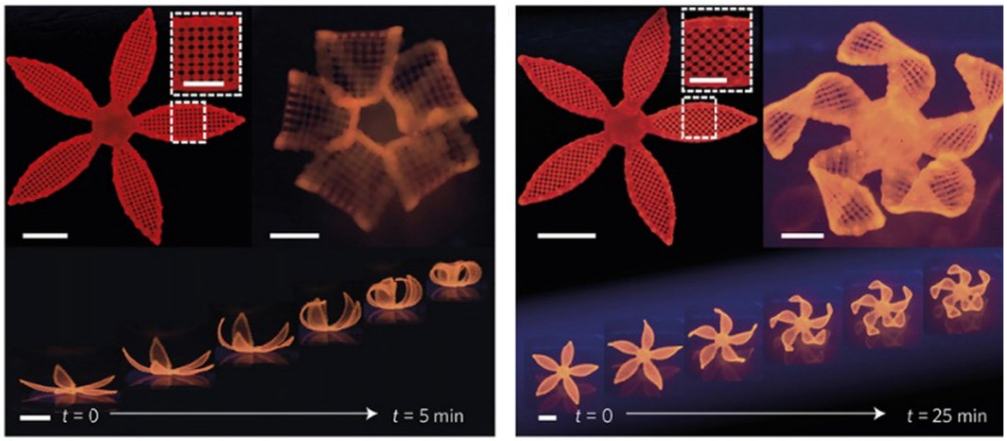

Figure 1.4. Bioinspired shape-morphing sequences actuated by anisotropic swelling[33].

In fact, for applications with living cells, a significant hurdle regards the simultaneous achievement of an effective processability by 3D printing, of a maintenance of cell viability during culture and of a cytocompatible actuation of shape transformations; consequently, stimuli-responsive hydrogels are often preferred to shape memory polymers for such applications. By way of example, this is the case of the recently reported 4D bioprinted silk fibroin hydrogel for which the shape morphing of the sheet into a trachea-like structure occurs during cell culture in culture medium[34]. Indeed, for hydrogels, it is possible to print a bio-ink containing the cells, whereas for 3D printed shape memory polymers, usually cell seeding is performed after printing and after programming of the temporary shape so as to avoid potentially harsh conditions for cell viability. To this respect, Hendrickson *et al.*[35] showed the development and characterization of a shape memory polyurethane scaffold featuring a glass transition temperature of about 32 °C. Cells were seeded after programming of the temporary shape and it was shown that the shape recovery process influenced the morphology of the cells, inducing cell stretching. However, further studies will still be needed to evaluate the potential cell damage occurring during shape recovery, as it is known to occur during printing through small nozzles, *i.e.* conditions in which the cells are subjected to large stresses.

This field is fairly new and developments in materials science and manufacturing process are expected to provide soon new opportunities and rapid progress.

Drug delivery

The use of shape memory polymers for the development of drug delivery systems (DDSs) has been proposed only in few pioneering works[36-39]. Interestingly, in 2009 Neffe *et al.* demonstrated that, by synthesizing *ad hoc* hydrolytically degradable shape memory polymer networks, they were able to decouple the diffusion-controlled release kinetics from the degradation one. Additionally the shape recovery was proved not to affect the drug release[40]. Recently, with the advent of 4D printing, the field has revalued the potentialities of active materials for the delivery of therapeutics at the desired anatomical location and at the needed time, in light of the new avenues provided by the design flexibility characterizing additive manufacturing techniques[41]. In fact, in an editorial published in 2019 on *Expert Opinion on Drug Delivery*[42], the authors pointed out the promising future ahead of 4D printing for example towards the aim of encapsulating and releasing drugs or cells in a programmable fashion and of designing novel soft robotic capsules capable of delivering the payload inside the human body.

In general, promising applications of 3D printed shape memory materials in the drug delivery field are those for which a shape evolution is essential for different purposes, mainly to retain the DDS in a targeted organ so as to i) increase the bioavailability of the conveyed drug, ii) treat local diseases, and iii) prolong the drug release in order to reduce the dosing frequency and consequently to increase patient adherence to the therapeutic regimen[43-45]. It is believed that these goals will be positively approached and potentially accomplished by 4D printing, since it enables the fabrication of devices with complex design, capable of shape-shifting over time under the application of an external non mechanical stimulus, suitable for demanding applications inside the human body.

In conclusion, the whole and, up to now, hidden potentialities of 3D printed shape memory polymers for the pharmaceutical field have yet to be explored in depth.

1.2 Motivation and outline of the thesis

This thesis was motivated in light of the tremendous research efforts currently being pursued in the materials science and manufacturing fields towards the aim of designing novel active materials and shape-shifting devices to be used for several applications, *e.g.* in the soft robotics and/or biomedical fields. Especially, biomedical applications, as previously described, might hugely benefit from the employment of materials featuring complex shape changes, remotely activated by the exposure to stimuli compatible with physiological conditions. Therefore, in this thesis a comprehensive study was performed starting by a careful investigation of the response of 3D printed shape memory materials and gradually moving to the development of applicative prototypes, with an increased design complexity.

Chapter 2 describes the study of a non-conventional shape memory effect, found for commercial resins for 3D printing. Obtained results may be useful for the design of sequentially-activated shape changes for medical devices featuring complex shapes. Furthermore, it was shown that additional functionalities can be provided by designing not only the shape memory material but also the structure and architecture in which it is printed. In this way, shape memory metamaterials can be achieved and resulted in exotic properties, as in the case of the negative Poisson's ratio obtained for the auxetic structure presented.

In Chapter 3 and Chapter 4 special attention was given to the design of a biocompatible shape memory effect for the design of an intravesical retentive device and a gastroretentive drug delivery platform, respectively. An investigation of the water-induced shape memory effect for the actuation of the devices was performed, together with a design activity for the selection of promising shapes and relevant shape evolutions to fulfil the requirements of easy and "minimally invasive" administration of the platform and of recovery of a bulky configuration enabling retention in the target organ.

Finally, on the basis of the huge potential held by long-term gastric resident devices, in Chapter 5 the design of a novel capsule-sized milli-gripper for the gastrointestinal tract is presented. This research activity was performed as part of a visiting period at the Massachusetts Institute of Technology, MIT (Cambridge, MA, US) and it is covered by a provisional application for patent.

1.3 References

1. A. Lendlein, S. Kelch, *Angew. Chem. Int. Ed.* 2002, 41, 2034-2057.
2. M. Behl, A. Lendlein, *Mater. Today* 2007, 10, 20-28.
3. R. Langer, D.A. Tirrell, *Nature* 2004, 428, 487-492.
4. Q. Zhao, H.J. Qi, T. Xie, *Prog. Polym. Sci.* 2015, 49-50, 79-120.
5. F. Momeni, S.M.M. Hassani N., X. Liu, J. Ni, *Mater. Des.* 2017, 122, 42-79.
6. S. Tibbits, *Archit. Des.* 2014, 84, 116-121.
7. S. Tibbits, C. McKnelly, C. Olguin, D. Dikovsky, S. Hirsch, *Proceedings of the 34th Annual Conference of the Association for Computer Aided Design in Architecture (ACADIA)* 2014, 539-548.
8. Q. Ge, H.J. Qi, M.L. Dunn, *Appl. Phys. Lett.* 2013, 103, 131901.
9. Q. Ge, C.K. Dunn, H.J. Qi, M.L. Dunn, *Smart Mater. Struct.* 2014, 23, 094007.
10. Y. Mao, K. Yu, M.S. Isakov, J. Wu, M.L. Dunn, H.J. Qi, *Sci. Rep.* 2015, 5, 13616.
11. A. Lendlein, R. Langer, *Science* 2002, 296, 1673-1676.
12. A. Lendlein, R. Langer, US 8,303,625 B2 2012.
13. C.M. Yakacki, R. Shandas, C. Lanning, B. Rech, A. Eckstein, K. Gall, *Biomaterials* 2007, 28, 2255-2263.
14. W. Small IV, T.S. Wilson, W.J. Benett, J.M. Loge, D.J. Maitland, *Opt. Express* 2005, 13, 8204-8213.
15. A.J. Boyle, T.L. Landsman, M.A. Wierzbicki, L.D. Nash, W. Hwang, M.W. Miller, E. Tuzun, S.M. Hasan, D.J. Maitland, *J. Biomed. Mater. Res. B* 2016, 104, 1407-1415.
16. J.P. Bearinger, D.J. Maitland, D.L. Schumann, T.S. Wilson, Patent No. US 8,882,786 B2 2014.
17. R. Kunkel, D. Laurence, J. Wang, D. Robinson, J. Scherrer, Y. Wu, B. Bohnstedt, A. Chien, Y. Liu, C.-H. Lee, *J. Mech. Behav. Biomed.* 2018, 88, 422-430.
18. T.L. Landsman, R.L. Bush, A. Glowczwski, J. Horn, S.L. Jessen, E. Ungchusri, K. Diguette, H.R. Smith, S.M. Hasan, D. Nash, F.J. Jr. Clubb, D.J. Maitland, *J. Mech. Behav. Biomed.* 2016, 63, 195-206.
19. T.R. Yeazel, M.L. Becker, *Biomacromol.* 2020, 21, 3957−3965.
20. Q. Ge, A.H. Sakhaei, H. Lee, C.K. Dunn, N.X. Fang, M.L. Dunn, *Sci. Rep.* 2016, 6, 31110.
21. C. de Marco, C.C.J. Alcântara, S. Kim, F. Briatico-Vangosa, A. Kadioglu, G. de Bernardis, X. Chen, C. Marano, B.J. Nelson, S. Pané, *Adv. Mater. Technol.* 2019, 4, 1900332.

22. X. Kuang, K. Chen, C.K. Dunn, J. Wu, V.C.F. Li, H.J. Qi, *ACS Appl. Mater. Interfaces* 2018, 10, 7381−7388.
23. R.J. Morrison, S.J. Hollister, M.F. Niedner, M. Ghadimi Mahani, A.H. Park, D.K. Mehta, R.G. Ohye, G.E. Green, *Sci. Transl. Med.* 2015, 7, 285ra64.
24. M. Zarek, N. Mansour, S. Shapira, D. Cohn, *Macromol. Rapid Commun.* 2017, 38, 1600628.
25. W. Zhao, F. Zhang, J. Leng, Y. Liu, *Compos. Sci. Tech.* 2019, 184, 107866.
26. H. Jia, S.-Y. Gu, K. Chang, *Adv Polym. Technol.* 2018, 37, 3222–3228.
27. X. Wan, H. Wei, F. Zhang, Y. Liu, J. Leng, J. Appl. Polym. Sci. 2019, 48177.
28. R.M. Baker, L.-F. Tseng, M.T. Iannolo, M.E. Oest, J.H. Henderson, J.H., Biomaterials 2016, 76, 388-398.
29. A. Pandey, G. Singh, S. Singh, K. Jha, C. Prakash, J. Mech. Behav. Biomed. 2020, 108, 103781.
30. L.-F. Tseng, P.T. Mather, J.H. Henderson, *Acta Biomater.* 2013, 9, 8790-8801.
31. T. Gong, K. Zhao, G. Yang, J. Li, H. Chen, Y. Chen, S. Zhou, *Adv. Healthc. Mater.* 2014, 3, 1608-1619.
32. J. Wang, A. Quach, M.E. Brasch, C.E. Turner, J.H. Henderson, *Biomaterials* 2017, 140, 150-161.
33. A.S. Gladman, E.A. Matsumoto, R.G. Nuzzo, L. Mahadevan, J.A. Lewis, Nat. Mater. 2016, 15, 413-419.
34. S. Hee Kim, Y. Been Seo, Y. Kyu Yeon, Y. Jin Lee, H. Sang Park, Md. Tipu Sultan, J. Min Lee, J. Seung Lee, O. Joo Lee, H. Hong, Hanna Lee, O. Ajiteru, Y. Ji Suh, S.-H. Song, K.-H. Lee, C. Hum Park, *Biomaterials* 2020, 260, 120281.
35. W.J. Hendrikson, J. Rouwkema, F. Clementi, C.A. van Blitterswijk, S. Farè, L. Moroni, *Biofabrication* 2017, 9, 031001.
36. C. Wischke, A.T. Neffe, S. Steuer, A. Lendlein, *J. Control. Release* 2009, 138, 243-250.
37. C. Wischke, A. Lendlein, A., *Pharm. Res.* 2010, 27, 527–529.
38. Y. Xiao, S. Zhou, L. Wang, X. Zheng, T. Gong, *Compos. Part B-Eng.* 2010, 41, 537-542.
39. M. Balk, M. Behl, C. Wischke, J. Zotzmann, A. Lendlein, *Adv. Drug Deliver. Rev.* 2016, 107, 136-152.
40. A.T. Neffe, B.D. Hanh, S. Steuer, A. Lendlein, *Adv. Mater.* 2009, 21, 3394–3398.
41. J. Firth, S. Gaisford, A.W. Basit In: Basit A., Gaisford S. (eds) 3D Printing of Pharmaceuticals. *AAPS Advances in the Pharmaceutical Sciences Series,* 2018, 31. Springer, Cham.
42. I. Lukin, S. Musquiz, I. Erezuma, T.H. Al-Tel, N. Golafshan, A. Dolatshahi-Pirouz, G. Orive, *Expert Opin. Drug Del.* 2019, 14, 953-956.

43. S. Babaee, S. Pajovic, A.R. Kirtane, J. Shi, E. Caffarel-Salvador, K. Hess, J.E. Collins, S. Tamang, A.V. Wahane, A.M. Hayward, H. Mazdiyasni, R. Langer, G. Traverso, *Sci. Transl. Med.* 2019, 11, eaau8581.
44. A.R. Kirtane, O. Abouzid, D. Minahan, T. Bensel, A.L. Hill, C. Selinger, A. Bershteyn, M. Craig, S.S. Mo, H. Mazdiyasni, C. Cleveland, J. Rogner, Y.-A.L. Lee, L. Booth, F. Javid, S.J. Wu, T. Grant, A.M. Bellinger, B. Nikolic, A. Hayward, L. Wood, P.A. Eckhoff, M.A. Nowark, R. Langer, G. Traverso, *Nat. Commun.* 2018, 9, 2294.
45. A.M. Bellinger, M. Jafari, T.M. Grant, S. Zhang, H.C. Slater, E.A. Wenger, S. Mo, Y.-A.L. Lee, H. Mazdiyasni, L. Korgan, R. Barman, C. Cleveland, L. Booth, T. Bensel, D. Minahan, H.M. Hurowitz, T. Tai, J. Daily, B. Nikolic, L. Wood, P.A. Eckhoff, R. Langer, G. Traverso, *Sci. Transl. Med.* 2016, 8, 365ra157.

Chapter 2

3D printing of shape memory polymers: exploration of a non-conventional effect for customized shape-shifting motions

The work here reported has been already partially published in:

- **N. Inverardi**, S. Pandini, F. Bignotti, G. Scalet, S. Marconi, F. Auricchio, Sequential Motion of 4D Printed Photopolymers with Broad Glass Transition, *Macromol. Mater. Eng.* 2020, 305, 1900370
- S. Pandini, **N. Inverardi**, G. Scalet, D. Battini, F. Bignotti, S. Marconi, F. Auricchio, Shape memory response and hierarchical motion capabilities of 4D printed auxetic structures, *Mechanics Research Communications* 2020, 103, 103463

2.1 Introduction

4D printing is a vibrant scientific community in which significant contributions come from various research fields involving different disciplines such as design and manufacturing, materials science and machine learning.

Pioneering works were focused on demonstrating quite complex shape-shifting motions, enabled by the design flexibility peculiar of 3D printing manufacturing techniques. Specifically, the problem was approached from a design perspective and multi-material 3D printing was leveraged to achieve "composite" structures, in which different inks/materials were carefully deposited in different locations of the structure. In this way, it was possible to obtain sequential motions, by activating motions at different sections/hinges of the structure at different time, thanks to the presence of multiple materials each one with its own thermal and thermo-mechanical properties. Examples can be found in the early works from Ge and Qi[1,2], who defined the concept of "printed active composites", *i.e.* soft composites obtained by printing shape memory polymeric fibers into an elastomeric matrix. They first studied the mechanical and shape memory behavior of printed lamina with prescribed volume fractions and orientations of the fiber, afterwards they designed hinges made out of the active composite to realize self-folding boxes[1] and origami[2] as shown in Figure 2.1.

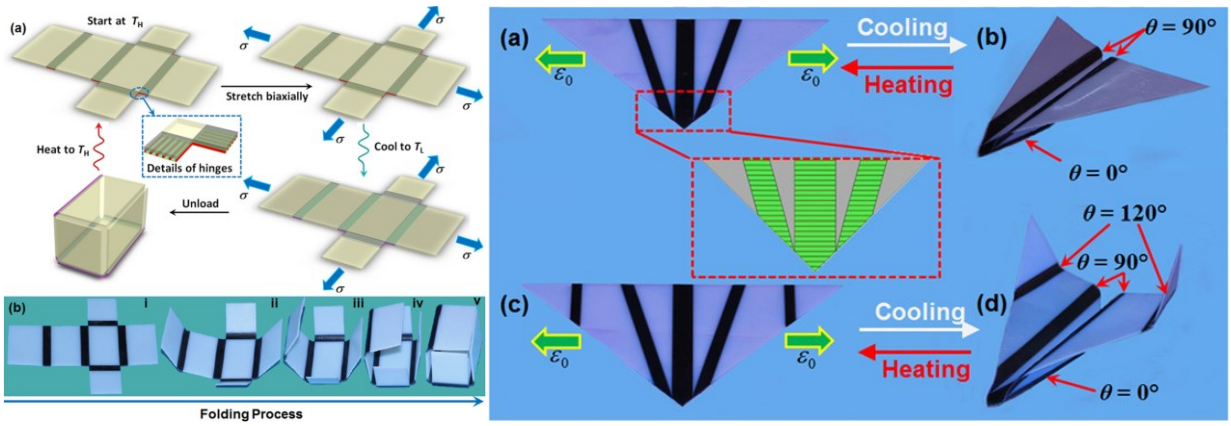

Figure 2.1. 4D printed origami and self-folding objects[1,2].

Later, the concept was refined by embedding the term "digital materials", *i.e.* resins for 3D printing formed by the mixture of two base materials at various ratios and deposited in specific locations guided by a digital voxelized domain[3,4]. The various compositions achieved by the use of only two base materials allowed to obtain a broad selection of shape memory materials each one with its own specific property profile, to be printed in the same structure at different sections, as shown in Figure 2.2.

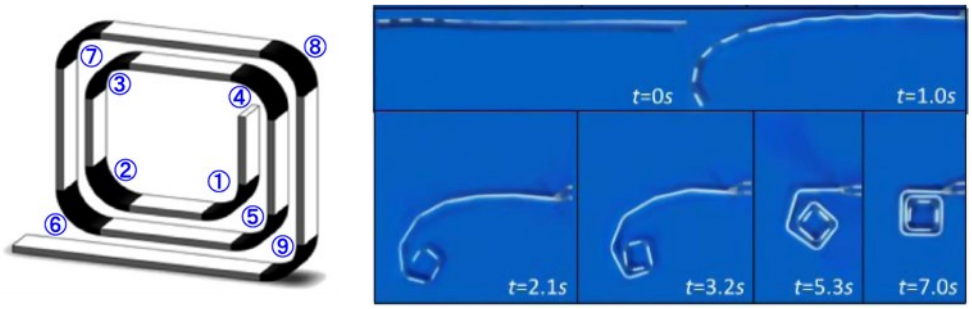

Figure 2.2. Multi-material rectangular spiral and its shape changes at subsequent time points[3].

Each digital shape memory polymer can be considered as a building block resulting in a library of available materials from which machine learning algorithms and computational models can draw to guide the design process and optimize the localization/printing of multiple materials for achieving the target shape[5-7]. This strategy is based on an inverse-design approach, by which the shape to reach represents the goal and the task of the design is to identify the parameters/materials/starting geometries leading to it, as outlined in Figure 2.3 in the case of a multi-material structured lattice[8,9].

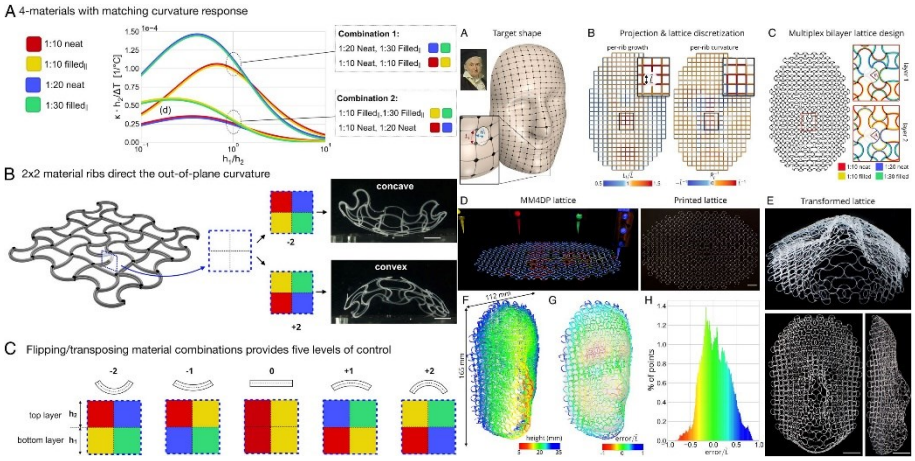

Figure 2.3. Shape-shifting multi-material lattices[8].

Another interesting multi-material approach used to achieve sequential shape-shifting motions focused on a slightly different triggering stimulus that is by employing light-induced selective heating to promote shape changes[10]. In this case, building on previous works which leveraged differential optical absorption of differently colored patterned inks onto a pre-stretched plastic sheet[11,12] as shown in Figure 2.4a, Jeong *et al.* used variously colored digital shape memory polymers. These materials have a similar glass transition temperature, however when exposed to light of a certain wavelength they change their temperature with a

kinetics depending on their color, thus ensuring different actuations and potential sequential shape changes, as those reported in Figure 2.4b and 2.4c.

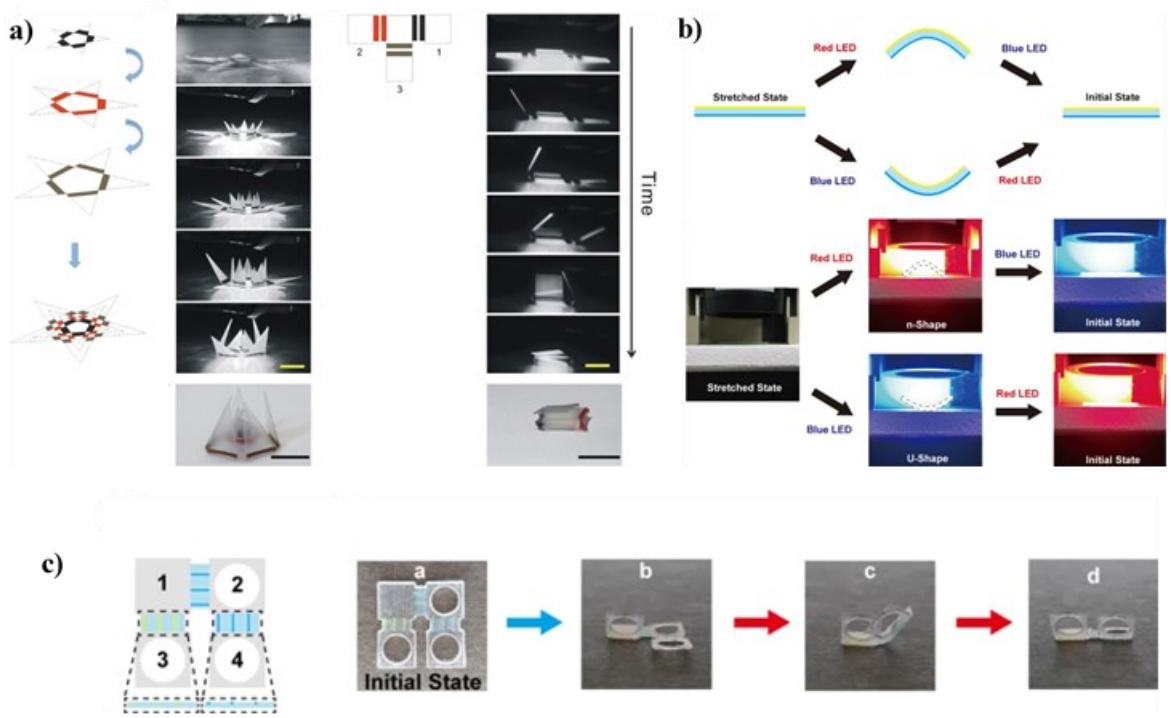

Figure 2.4. Light-activated shape changes for a) 2D polymeric sheets with laserjet-printed colored hinges[11]; b) 3D printed colored shape memory polymer[10]; c) 3D printed variously colored shape memory polymer with sequential motion capability.

It is clear that multi-material 3D printing holds a great potential to design and realize complex shape-shifting structures, however, from a materials science point of view, little is known about exploiting more refined shape memory effects to obtain customized shape changes[13-15]. Indeed, having the possibility to control the shape changes from a macromolecular perspective could open new avenues including achieving multiple and/or reversible shape changes by using tailored materials. In fact, shape memory polymers can be designed to exhibit multiple shape memory effects by either relying on more than one reversible transformation temperature or on a single broad transition region. With the former approach, blends or copolymers embedding various phases, each one triggered by a specific transformation temperature (*i.e.* the glass transition temperature, T_g or the melting temperature, T_m), can be used to obtain distinct shape memory transitions[16,17]. On the basis of the latter strategy, polymers with a single broad transition corresponding to either a melting[18,19] or a glass transition region[20] can be designed by controlling their structures[21,22], their network architectures[23,24],

or their supramolecular interactions[25]. For these systems specifically it is possible to exploit the so-called "temperature-memory effect" (TME), by which the activation of recovery processes occurs on distinct thermal regions depending on the thermo-mechanical programming history, and in particular on the deformation temperature lying in the broad transition region identified. Thanks to the TME, by performing the programming of the temporary shape(s) in multiple steps, each one carried out at a given temperature, it is possible to achieve sequential shape-shifting motions.

Therefore, the focus of this chapter is on applying 3D printing to material systems capable of exhibiting non-conventional shape memory effects for the aim of obtaining 4D printed structures featuring relatively complex shape changes.

The work presented in this chapter was carried out in collaboration with Dr. Giulia Scalet, Dr. Stefania Marconi and Prof. Ferdinando Auricchio from the Computational Mechanics and Advanced Materials group of the University of Pavia and with Dr. Davide Battini (University of Brescia).

2.2 Design Concept

The focus in this chapter was on applying a materials science approach to the design problem, commonly found in the 4D printing research field, of achieving complex shape-shifting motions, including sequential shape-folding and self-locking. This aim was reached by starting with a wide screening of both *ad hoc* synthesized and commercially available polymeric materials, eventually leading to the selection and application of most promising material candidates to proof-of-concept prototypal devices and structures.

The inspiration for the proof-of-concept structures was found by taking into account both the scientific background and potentially useful applications.

A first device was conceived on the basis of a sequential self-locking mechanism commonly used in the 4D printing community to prove sequential shape-shifting behavior[3]. In fact, the mechanism shown in Figure 2.5 is very suitable to highlight the importance of achieving distinct motions on the time scale: the locking tab has to close only after the movements of all the other hinges and additionally it does not have to collide with the structure, yet it has to insert in the proper gap.

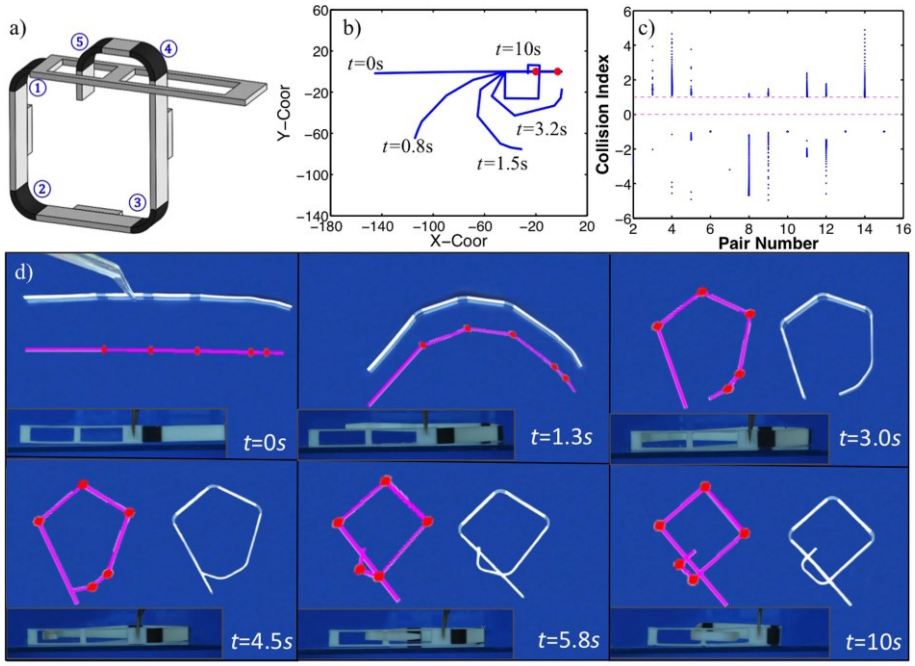

Figure 2.5. 4D printed self-locking clamp based on digital shape memory polymers[3].

Likewise, other structures of high interest are shape-morphing metamaterials[26,27], for instance as those shown in Figure 2.6, which can target and approximate various shapes thanks to potential coupling/decoupling of in-plane and out-of-plane deformations. Adding the capability of non-mechanical stimuli-responsiveness to such metamaterials could lead to the achievement of untethered structures promising for applications in various diverse research fields*, e.g.* from soft robotics to medical devices design and development; for this reason they are receiving growing attention[28,29] .

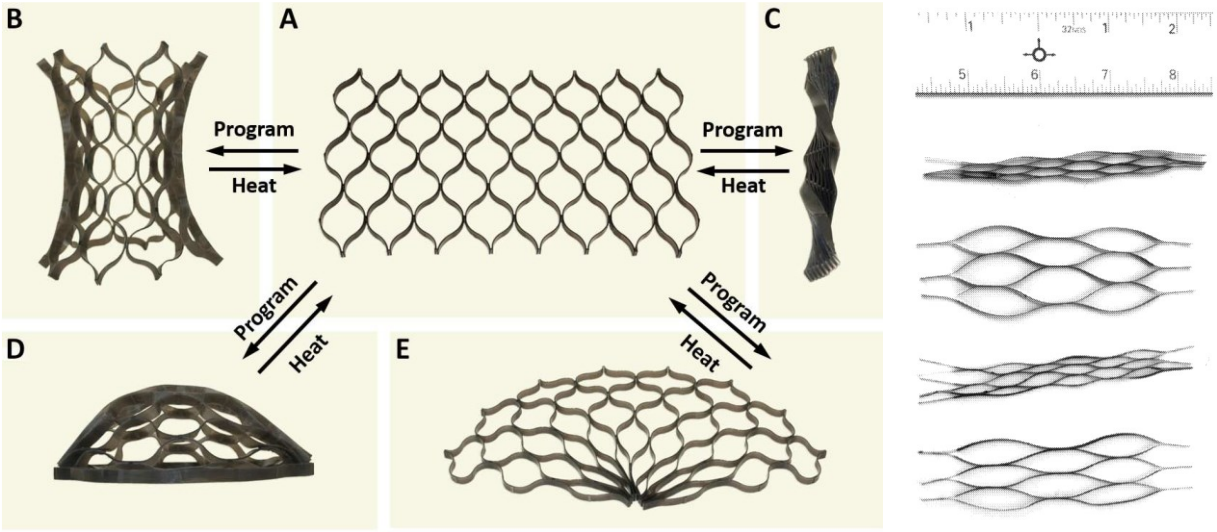

Figure 2.6. Lattices capable of complex shape-shifting motions under the application of an external stimulus[26,27].

The novelty proposed in this chapter consisted in leveraging non-conventional shape memory effects to obtain sequential shape-shifting capabilities for two purposely designed structures: i) a self-locking clamp and ii) an auxetic structure.

The design for the self-locking clamp is reported with a 3D view and its drawings in Figure 2.7a. The goal set was to obtain sequential motions similar to what is represented in Figure 2.7b.

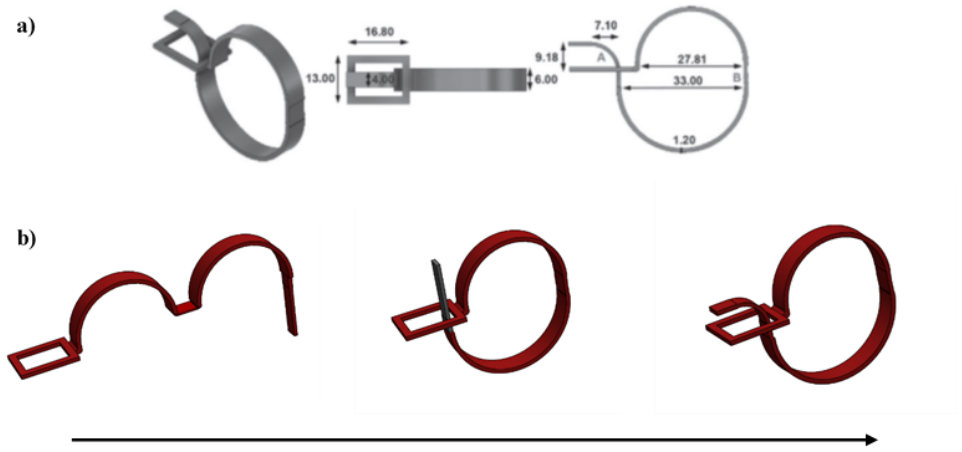

Figure 2.7. Design 1: single-material self-locking clamp. In a) 3D view and 2D drawings with dimensions; in b) targeted sequential shape-shifting motion from the first temporary shape (left) to the permanent one (right).

The design for the auxetic-based metamaterial is shown in Figure 2.8a with a focus on the geometric parameters for its unit cell. A potential interesting shape change to target could be the one represented in Figure 2.8b for which the planar structure is first folded into a cylindrical shape and then axially stretched. Heating would eventually promote the recovery of the flat planar auxetic structure, by first contracting in the axial direction.

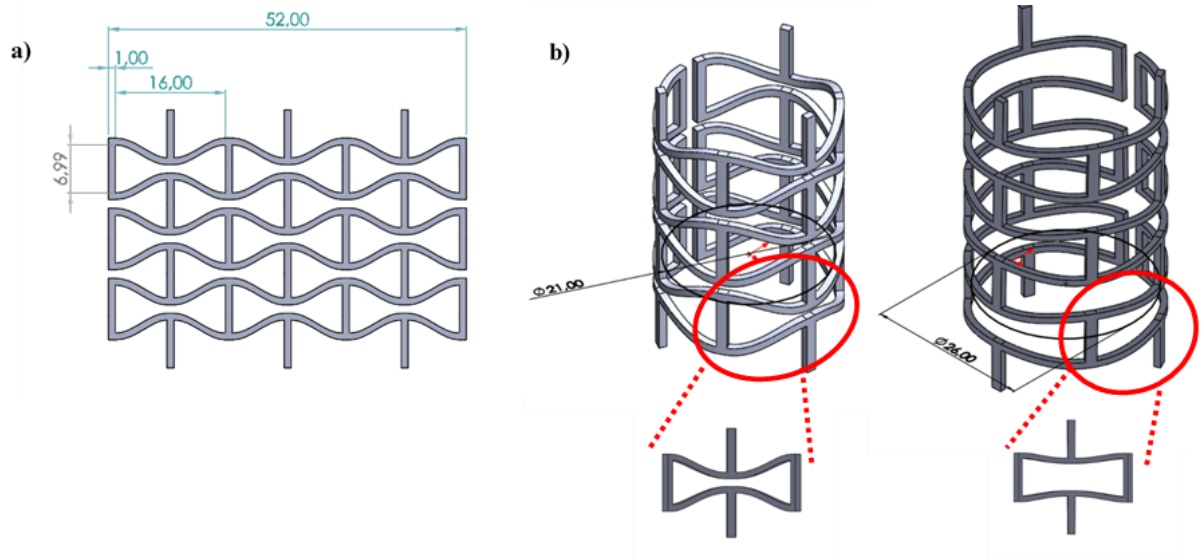

Figure 2.8. Design 2: auxetic structure. In a) permanent shape; in b) programmed temporary shapes achieved by wrapping the sheet in a cylindrical configuration and then axially stretching it thus promoting also a radial expansion. The red circles highlight a single unit cell during the deformation.

2.3 Materials

A library of commercially available materials was screened in terms of their potentiality to exhibit the shape memory effect.

To narrow down the window of materials to characterize, the design requirement that guided the selection concerned a specific macromolecular architecture, known to provide optimal shape memory capabilities, namely crosslinked networks. In fact, it is know that the shape memory effect is optimized for those structures in which the "hard domains" consist of chemical crosslinking points. Chemical crosslinking points are more effective than physical crosslinks to the aim of ensuring complete recovery of the permanent shape, due to their higher likelihood to remain stable throughout all the shape memory cycle.

As a consequence, also the choice of the 3D printing technique to use was guided by the necessity of obtaining a crosslinked network, proper of a thermoset resin. 3D printing techniques suitable for thermoset resins are those ones starting with a liquid resin which undergoes crosslinking reactions upon exposure to light of a specific wavelength. These manufacturing techniques are generally classified under the name of vat photopolymerization 3D printing and include for instance stereolithography (SLA) and digital light processing (DLP), depending on the component used as a source of light, *i.e.* a laser or a projector, for SLA and DLP respectively.

The 3D printing technique finally selected was SLA and the hardware employed was the Formlabs Form 2 3D printer (Formlabs, Massachusetts, US). This desktop-sized 3D printer has a building volume of 145 × 145 × 175 mm^3 and it is equipped with a UV laser (405 nm violet laser) of 250mW of power and with a spot of 140 μm. CAD models of specimens and structures were drawn using the software SolidWorks (Dassault Systèmes), exported in .stl format and finally the software PreForm (Formlabs) was used to orient the models and to add the support structures. 3D printed samples and structures were cleaned in a bath of isopropyl alcohol for 20 minutes in order to wash away any residue of uncured resin and finally the support structures were manually removed.

The resins selected were the Clear FLGPCL02 and the Flexible FLFLGR02 from Formlabs, in order to screen materials within a wide window of mechanical properties.

The Clear resin belongs to the standard portfolio of Formlabs resins: it's a rigid and transparent plastic suited for designing internal features/channel for applications in optics, moldmaking and fluidics. From a chemical point of view, it is made out of a mixture of methacrylic acid esters and photoinitiators, working upon the exposure to a 405 nm light source[30,31]. The resin can be photopolymerized in layers with different thicknesses ranging from 25 (corresponding to the maximum resolution) to 100 (corresponding to the minimum resolution) μm.

The Flexible resin is sold among the engineering resins and it is supposed to simulate a 80A durometer rubber and TPU. It is composed of urethane dimethacrylate, methacrylate monomers and photoinitiators working upon the exposure to a 405 nm light source[30,32]. The minimum layer thickness allowed when using the Formlabs Form 2 3D printer is 50 μm.

For both the resins, a post-curing treatment is suggested and can be carried out by employing the Form Cure (Formlabs), which is a station for heat and light assisted post-curing, with a heating chamber reaching a maximum temperature of 80 °C and equipped with 13 405 nm LEDs, following the settings (*i.e.* curing time and temperature) suggested by the manufacturer. Alternatively, it is possible to perform a thermal-induced post-curing by exploiting only the effect of the temperature. In this work, this latter kind of post-curing treatment was chosen and carried out inside a laboratory oven using time and temperatures parameters (namely 1 hour at 200 °C) derived from preliminary thermal characterizations of the materials.

2.4 Methods

The experimental methodologies utilized to characterize the materials are here presented. Both the Clear and the Flexible resins underwent a preliminary characterization with thermal, thermo-mechanical and mechanical tests.

Differential scanning calorimetry analyses

Differential scanning calorimetry (DSC) analysis was performed with a DSC Q100 calorimeter (TA Instruments), employing nitrogen as purge gas on specimens (about 10 mg) from 3D printed materials in as printed or post-cured conditions. The specimens were subjected to three scans: i) a first heating from −80 °C to 200 °C at 10 °C/min; ii) a cooling from 200 °C to −80 °C at 10 °C/min; iii) a second heating from −80 °C to 200 °C at 10 °C/min. In order to evaluate the extent of reaction in the as printed photocrosslinked system, additional DSC tests were run on a DSC 1 STARe System (Mettler Toledo) on the as printed material and on the starting unreacted resin. These tests consisted of a heating from 40 to 230 °C at 10 °C/min. Prior to the DSC scan, for the liquid unreacted resin, the solvent contained in the resin was evaporated under vacuum (100 °C for 1 h). These conditions were selected to ensure solvent evaporation without the onset of crosslinking.

Dynamic mechanical analyses

Dynamic mechanical analysis (DMA) tests were carried out by means of a DMA Q800 analyzer (TA Instruments) under tensile configuration on bar-shaped specimens (gauge length: 15–18 mm). The tests were performed scanning a region between −50 and 200 °C at 1 °C/min with an applied displacement amplitude equal to 10 μm and at a frequency equal to 1 Hz. For the testing following a multifrequency approach, the bar-shaped specimen was subjected to a strain-controlled test with an applied displacement amplitude of 15 μm, along a heating ramp at 0.5 °C/min on a region between -50 °C and 140 °C and a frequency sweep between 0.4 Hz and 100 Hz.

Mechanical characterization

Tensile tests were carried with the dynamic mechanical analyzer DMA Q800 analyzer (TA Instruments) on bar-shaped specimens (gauge length: 15–18 mm) both at room temperature and at a temperature equal to about T_g + 40 °C, with a load ramp equal to 0.1 N/min, until fracture.

Compression tests were performed by means of an electromechanical dynamometer (Instron, Mod. 3366) equipped with a thermal chamber at various temperatures ranging from room temperature to 120 °C. Cubic specimens (4x4x4 mm^3) were compressed up to a value of 40% nominal strain with a crosshead speed equal to 1 mm/min.

On the Clear resin an in-depth shape memory characterization was performed in order to investigate and characterize the temperature-memory effect.

Investigation of the temperature-memory effect found for the Clear resin

The shape memory characterization is divided into two parts: in the first one, the so-called “programming”, the temporary shape is set by a proper use of heating and cooling steps above and below the transition temperature of the material; secondly, the recovery of the permanent shape is triggered either applying heating ramps, following the so-called thermally stimulated recovery (TSR), or under isothermal conditions. The deformation conditions applied during the programming are strictly dependent on the recovery conditions chosen, so that in the following paragraphs, each programming condition is described in relation to its relevant recovery.

Thermally stimulated recovery (TSR)

Single-step programming

Cubic specimens were set in a compressed temporary shape by applying a compressive strain value equal to 40% at various deformation temperatures T_{def} ranging from room temperature, T_{room} to 120 °C

by using the dynamometer. To fix the compressed shape, the specimens were allowed to cool for at least 30 minutes, while under the applied displacement, kept by fixing the crosshead. Afterwards, the specimens were removed from the dynamometer and stored at -20 °C in a refrigerator prior to the recovery. In order to test the recovery and monitor the evolution of the specimen height as a function of temperature, TSR tests were carried out by using the dynamic mechanical analyzer DMA Q800, applying a heating ramp at 0.5 °C/min from T_{room} up to 125-150 °C, according to the material system, under the application of a small load (0.02N).

The results were represented in terms of the recovery ratio R_r and the recovery rate, defined in Equation 1 and 2 respectively as:

$$R_r(\%) = \frac{h - h_{prog}}{h_0 - h_{prog}} \times 100 \quad (1)$$

where h is the actual height of the specimen, h_{prog} is the height after the programming step, and h_0 is the original height of the specimen;

$$Recovery\ rate = \frac{dR_r}{dT} \quad (2)$$

Multi-step programming

Multi-step programming histories were applied to specimens of different shapes (cubes, bars) under different deformation conditions (compression, folding).

Two-step compression

An as printed cubic specimen was first compressed at a temperature equal to 100 °C, called T_{high}, up to a nominal strain equal to 20% , kept constant during the following cooling to T_{room}. Afterwards, the specimen was heated up to a temperature of 40 °C, called T_{low}, and compressed of an additional 20% of nominal strain. The compressed specimen was finally cooled down under fixed strain to T_{room}. The TSR test was carried out following the same protocol previously described.

Two-step folding

An as printed bar-shaped specimen was first deformed by bending one side with a 180° angle at T_{high} and cooled under the applied deformation to T_{room}; then, also the other side was deformed by a 180° bending at T_{low}, cooled under the bent configuration and the double-folded bar was eventually stored in a refrigerator at -20 °C before the TSR test.

The TSR test was carried out inside a laboratory oven with a transparent glass window, heating up the folded specimen from T_{room} to T_{high} at a rate of 1 °C/min. The recovery process was recorded with a camera (Nikon D700) placed in front of the oven window, with a frame rate of 1 picture/30 s and the temperature was measured with a thermocouple placed near the sample. The shape changes were quantified by measuring the angle of the arms, α, with a digital image analysis software (ImageJ) and the recovery ratio $R_{r,angle}$ was evaluated in Equation 3 as follows

$$R_{r,angle}(\%) = \frac{\alpha_{prog} - \alpha}{\alpha_{prog}} \times 100 \quad (3)$$

where α_{prog} is the angle of the arms after the programming ($\alpha_{prog} \approx \pi$) and α is the actual angle, being all the angles measured in rad.

Isothermal recovery tests

Double-folded bars were obtained similarly to what described previously, by a 180° bending of their two extremities, both for as printed and post-cured specimens. The deformations were carried out following three different programs so as to achieve three differently programmed specimens: 1) specimens with both arms folded at T_{high}; 2) specimens with both arms folded at T_{low}; 3) specimens with one arm folded at T_{high} and one at T_{low}. In this last case, one side was deformed at T_{high}, then cooled to T_{room} under the deformation applied and later the other side was bent at T_{low} and cooled under fixed strain to T_{room}. For as printed specimens T_{high} is equal to 100 °C and T_{low} to 40 °C, whereas for

post-cured specimens T_{high} is 120 °C and T_{low} is 70 °C. All the programmed specimens were kept at -20 °C in a refrigerator prior to the recovery tests.

Isothermal recovery tests were carried out as a sequence of 30-minute step at a given temperature, following a progressive increase of temperature from step to step. More in details, two specimens programmed in the same fashion were subjected to two different temperature sequences, the first one comprising T_{room}, 50, 70, 90 and 110 °C, whereas the second one covering the temperatures of 40, 60, 80, 100 and 120 °C. The recovery was followed with a camera (Nikon D700) and evaluated with the recovery ratio $R_{r,angle}$ defined in Equation 3. An attempt to construct a master curve for the recovery ratio of both the extremities was carried out by applying a time-temperature superposition scheme, at the reference temperature T_{ref} of 60 °C.

Sequential self-folding clamp

The self-locking clamp mechanism shown in Figure 2.7 was first programmed by opening the locking tab at T_{high} and cooling under the deformed configuration; then, the general hinge of the mechanism was deformed and opened at T_{low}, followed by cooling. The sequential recovery of the mechanism was studied in isothermal conditions, by placing the structure inside a thermoregulated water bath at 60 °C.

Mechanical and shape memory characterization on the auxetic structure

The auxetic structure was characterized for its thermal, mechanical and shape memory properties.

A DSC analysis was performed on a piece of about 10mg cut from the 3D printed structure employing the DSC Q100 calorimeter (TA Instruments) and using nitrogen as a purge gas. The scans consisted of a first heating, a cooling and a second heating runs spanning over the temperature window from -80 to 110 °C at 10 °C/min.

The mechanical characterization was carried out by means of the electromechanical dynamometer (Instron Mod. 3366) under uniaxial tensile conditions at room temperature, with a crosshead speed

equal to 20 mm/min up to 10 mm of maximum displacement. The structure was sputtered with black markers on its knots and the whole test was recorded with a camera (Nikon D700) acquiring pictures at a rate of 1 frame/s. Prior to each test, a picture for a calibration grid was taken. Data relevant to the positions of the markers during the test were analyzed with a purposely developed Labview code by Dr. Davide Battini in order to obtain displacement and strain outputs.

A basic shape memory and temperature memory characterization was repeated on the structure in addition to the one already performed for the printed bar-shaped and cubic specimens. In the here described case of the printed structure, the specimen used for the shape memory cycles was the single unit cell cut from the whole structure. The unit cell was clamped inside the dynamic mechanical analyzer by using tensile grips and with this configuration four sets of tests were carried out.

- The first set of test consisted in the application of a single programming carried out at T_{high} (equal to 100°C) with the application of 3.5 mm of displacement and with the consequent cooling, followed by a modified TSR test with visual sampling of the partially recovered shapes for different temperatures inside the heating ramp. More in details, heating was applied up to a given temperature at 1 °C/min under quasi stress-free conditions to promote partial recovery, and cooling to room temperature was imposed to fix the shape and to take a picture of the specimen configuration at this extent of the recovery. This step was repeated for different temperatures, progressively increasing, until full recovery was achieved.
- The second set of test consisted in the application of the following thermo-mechanical protocol: i) thermal equilibration at a given temperature T_{def}, equal to 20, 40, 60, 80 and 100 °C (in each test a single temperature was chosen and a total of 5 tests were performed); ii) application of a tensile displacement equal to 3.5 mm (reaching about the 90% of the elongation required to open up the unit cell, without wall distortions); iii) cooling down to -15 °C under the applied displacement; iv) application of a heating ramp at 1 °C/min from -15 to 110 °C under quasi stress-free conditions (*i.e.* a constant load of 0.001N was applied just to maintain the contact and to monitor the cell tensile displacement).

- The third set of test consisted in the application of a two-step programming under the same deformation conditions: first, the sample was heated up to T_{high} (equal to 100°C) and a tensile displacement equal to 1.75 mm, corresponding to the half of the total maximum displacement applied in the first set of test, was applied. Cooling under fixed displacement was then applied down to -20 °C to fix the deformation. Afterwards, a second displacement equal to 1.75 mm was applied at T_{low} (equal to 40 °C), followed by cooling under fixed strain down to -20 °C. Finally the recovery was studied in a TSR test with a heating ramp at 1 °C/min up to 110 °C under quasi stress-free conditions.
- The fourth set of test consisted in the application of a two-step programming under different deformation conditions. First, an out-of-plane bending was manually applied at T_{high} (equal to 100 °C) and then cooling was applied down to -15 °C under the deformed configuration. Afterwards, a tensile elongation equal to 3.5 mm was applied inside the dynamic mechanical analyzer at T_{low} (equal to 40 °C). Finally the sample was cooled down to -15 °C under the final deformed configuration. The TSR test was conducted inside the dynamic mechanical analyzer by applying a heating ramp at 1 °C/min up to 110 °C under quasi stress-free conditions. The heating ramp was repeatedly interrupted cooling to room temperature to fix a temporary shape corresponding to that instantaneous partial recovery, opening the DMA furnace in order to take a picture of the partially recovered shape corresponding to that given temperature reached. The recovery was then continued by closing the furnace and restarting the heating ramp.

The shape memory performances were quantified by means of the following parameters, defined in Equation 4, 5, 6, 7 and 8 as:

$$Normalized\ displacement, \Delta_{norm}(\%) = \frac{\Delta l}{\Delta l_{app}} \times 100 \quad (4)$$

$$Strain\ fixity, SF\ (\%) = \frac{\Delta l_{unload}}{\Delta l_{app}} \times 100 \quad (5)$$

$$Strain\ recovery, SR\ (\%) = 100 - \left(\frac{\Delta l_{final}}{\Delta l_{app}} \times 100\right) \quad (6)$$

$$Recovery\ rate\ \left(\frac{\%}{^{\circ}C}\right) = \frac{d\left(\frac{\Delta l}{\Delta l_{app}}\right)}{dT} \times 100 \quad (7)$$

$$Normalized\ width, W_{norm}(\%) = \frac{\Delta W}{\Delta W_{app}} \times 100 \quad (8)$$

where $\Delta l = l - l_0$; $\Delta l_{app} = l_{app} - l_0$; $\Delta l_{unload} = l_{unload} - l_0$; $\Delta l_{final} = l_{final} - l_0$; $\Delta W = W - W_0$; $\Delta W_{app} = W_{app} - W_0$; l is the distance between the clamps during the test; l_0 is the initial clamp distance; l_{app} is the clamp distance corresponding to the applied displacement; l_{unload} is the clamp distance at load removal; l_{final} is the clamp distance at the end of the heating ramp; W is the specimen overall width, measured frontally, during the test; W_0 is the initial overall width; W_{app} is the specimen overall width, measured frontally after bending.

2.5 Results and discussion

The preliminary activities performed allowed to identify materials systems promising with respect to the potentiality of exhibiting the shape memory effect. This characterization eventually led to the selection of one material candidate for a more thorough shape memory characterization. In the following paragraphs, obtained results are presented.

Two different materials with significantly different mechanical behavior, as indicated by the manufacturer, were initially chosen: the stiff Clear resin and the elastomeric-like Flexible resin, both by Formlabs. Their thermal and thermo-mechanical properties were investigated by means of DSC, whose results are reported in Figure 2.9a, and by DMA, as shown in Figure 2.9b and 2.9c. The materials were tested both in their as printed state and after a thermal treatment simulating a post-curing one.

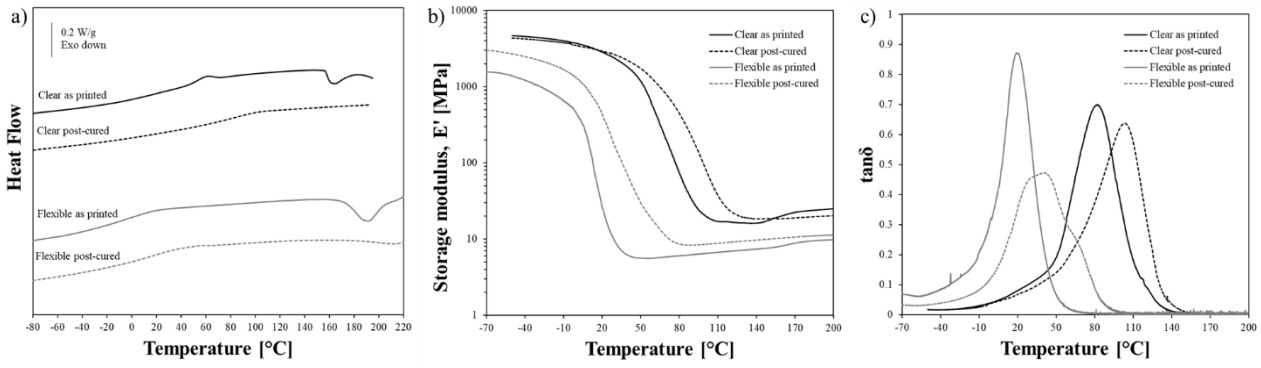

Figure 2.9. Thermal and thermo-mechanical characterization for the Clear and Flexible resins. In a) DSC traces for the as printed (1st heating scan) and for the post-cured (2nd heating scan) systems; b) storage modulus and c) loss factor (tan δ) traces as a function of temperature for the as printed and the post-cured systems.

The DSC traces, reported in Figure 2.9a as 1st heating scan, revealed for the as printed systems a widely distributed glass transition region, spreading over a temperature interval between 30 °C and 70 °C for the Clear system and between -40 °C and 20 °C for the Flexible system. Furthermore, they revealed the presence of an evident exothermal signal, at temperatures higher than 150 °C (well above the material T_g). The exothermal trace is not present in a second heating scan (not shown here), and for this irreversible nature is ascribed to the presence of reactive moieties, in all likelihood due to a non complete crosslinking process.

These results suggested to subject the material to a thermal treatment, carried out by heating the material at 200 °C for 1h, followed by a slow cooling, with the aim of increasing the crosslinking extent. After the application of the treatment, further DSC analyses were carried out on these post-cured systems showing an increase of the T_g for both systems, and a further broadening of the glass transition process, particularly evident in the case of the Clear system.

The DSC results were further confirmed by DMA tests, as it can be seen in Figure 2.9b and 2.9c, in which the storage modulus and tan δ traces of the Clear and Flexible systems in their as printed state are compared to those in their post-cured state.

The evidence of the thermally activated crosslinking can be seen in the sudden increase of the modulus at about 150 °C for the as printed systems, as a consequence of the progressive increasing network density; interestingly, after the thermal treatment the systems do not show any further property changes in the rubbery region. In addition, the increase of the crosslinking extent is strictly correlated to the broadening of the tan δ peak, which is particularly evident for the Flexible system, in the post-cured systems with respect to the as printed ones, as already suggested in literature[33].

The values of T_g, as evaluated by DSC and by the peak of the loss modulus E'' (here not shown) from DMA analyses, are reported in Table 2.1.

System	T_g from DSC [°C]	T_g from DMA [°C]	$E'_{r,min}$ [MPa]	n [mol m^{-3}]
Flexible, as printed	-5	-2	5.5	672
Flexible, post-cured	3	10	8.3	918
Clear, as printed	53	32	15.9	1560
Clear, post-cured	84	53	18.3	1720

Table 2.1. Glass transition temperature evaluated by DSC and DMA, rubbery modulus $E'_{r,min}$, and crosslink density of the resin n evaluated by the rubber theory with Equation 9.

Crosslink density was evaluated for all the systems by an approximate application of the rubber theory with the Equation 9

$$E'_{r,min} = 3nRT \quad (9)$$

where $E'_{r,min}$ is the rubbery modulus, taken as the minimum value of the storage modulus E' in the rubbery plateau, n is the crosslink density, R is the gas constant, and T is the absolute temperature in correspondence of $E'_{r,min}$.

The results, shown in Table 2.1, allow to quantify the increase in crosslink density after the treatment and to evaluate for all the materials, also for the Flexible resin, a high value of crosslink density. Specifically for the Clear system, the post-curing treatment induced a 10% increment of the crosslink density.

On the basis of these results, the Clear system is found to be in its glassy state at room temperature for both the conditions tested, whereas the nominal value of T_g for the Flexible resin is smaller than T_{room}. With the aim of exploring shape transformation occurring for temperatures equal or greater than T_{room}, the Clear resin was selected and further characterized.

An additional DSC scan was carried out on the starting liquid unreacted resin and it was compared to the first scan of the as printed system in Figure 2.10a and 2.10b.

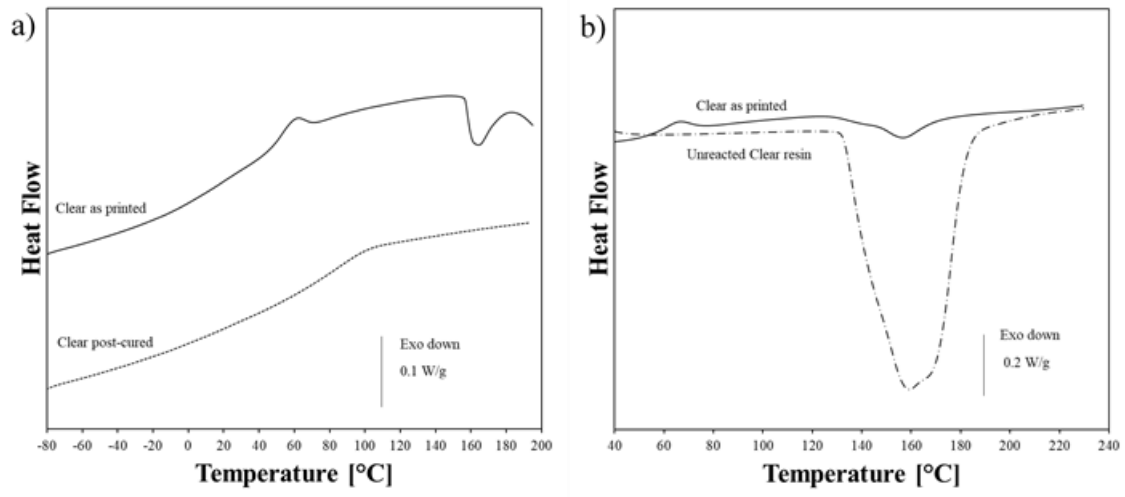

Figure 2.10. Comparison of the DSC scans a) between Clear as printed and Clear post-cured; b) between the starting unreacted resin and the Clear as printed.

Thanks to the additional DSC scans, the extent of the photocrosslinking reaction in the as printed state, *i.e.* after the 3D printing process, with respect to that one characteristic of the neat resin, was evaluated by means of Equation 10

$$Extent\ of\ the\ reaction\ (\%) = \frac{\Delta H_{resin} - \Delta H_{3Dprinted}}{\Delta H_{resin}} \times 100 \quad (10)$$

where $\Delta H_{3Dprinted}$ refers to the area evaluated from the exothermal peak found in the 1st heating scan of the

3D printed samples and ΔH_{resin} to the area corresponding to the exothermal peak found in the heating scan of the starting unreacted resins. The extent of the reaction may be estimated as about 95%. Eventually, the material in its post-cured state resulted in a fully crosslinked network, achieved by a combination of the prominent role of the photopolymerization occurring during the printing process and a minor contribution given by the reactions induced by the thermal treatment.

Testing on DMA was also carried out by applying a multifrequency approach. Its first aim was to determine, through an empirical application of a time-temperature superposition scheme, the time-dependency in terms of master curve and, furthermore, the distribution of the relaxation spectrum over the corresponding frequency of the master curve, obtained according to Equation 11

$$H(\omega) = -\frac{d|E'(\omega)-E_e|}{dln\omega} \quad (11)$$

where E_e represents the relaxed modulus, taken as the minimum value of E' in the rubbery plateau and the frequency ω is expressed in rad/s.

The results are reported in Figure 2.11a, as isothermal curves from frequency sweeps (inset of the Figure 2.11a), and as the master curve, represented for a reference temperature, T_{ref} = 45 °C, for the Clear system in its as printed state. The approach was applied also on the Clear post-cured and in Figure 2.11b the master curves are represented at the same reference temperature of that of Clear as printed (T_{ref} = 45 °C), while their relaxation spectra are reported in the inset of Figure 2.11b, with a solid line superimposed to better highlight the shape of the curves.

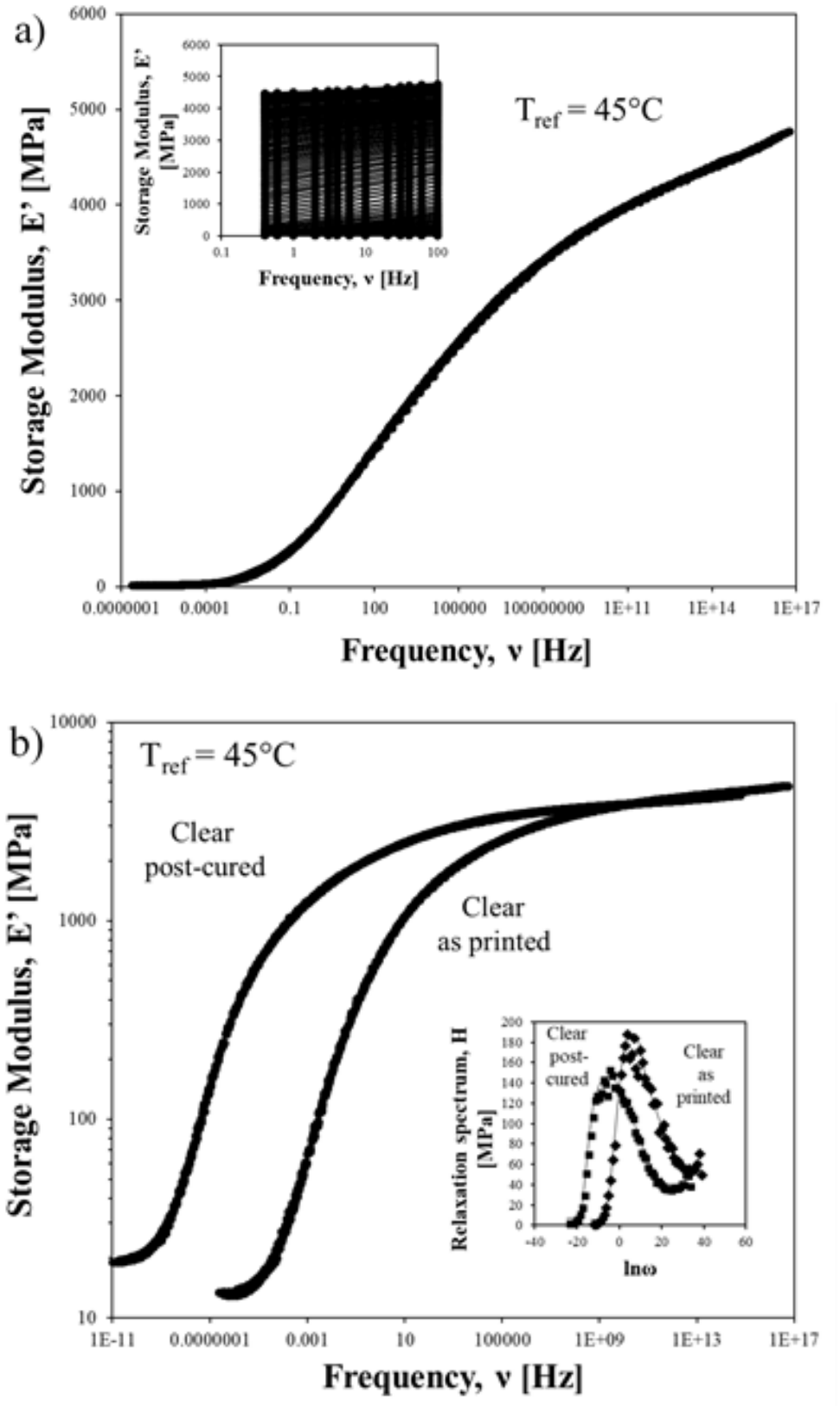

Figure 2.11. a) Master curve of the storage modulus measured on the Clear system in the as printed state for a reference temperature T_{ref} = 45°C; in the inset isothermal curves from the frequency sweeps. b) Master

curves of the storage modulus for the Clear systems in the as printed and treated states and represented for T_{ref} = 45°C; in the inset relaxation spectra as function of the natural logarithm of the angular frequency.

The result shows for both curves a similar behavior, with a closely resembling dependency on time, located at lower frequency (or higher relaxation times) in the case of the post-cured material, consistently with its increase in T_g. Moreover, the broadening of the relaxation process is also appreciable from the shape of the relaxation spectra, with the post-cured system displaying a broader relaxation spectrum, supporting the results obtained by the single-frequency DMA tests and the DSC data obtained, similarly to what proposed by Laukkanen *et al*. for glass-forming liquids in correlating calorimetric and viscoelastic broadening of glass transition[34].

Preliminary mechanical tests under tensile conditions revealed a brittle behavior both at room temperature and above the T_g. The results of tensile tests are reported in Figure 2.12a and 2.12b.

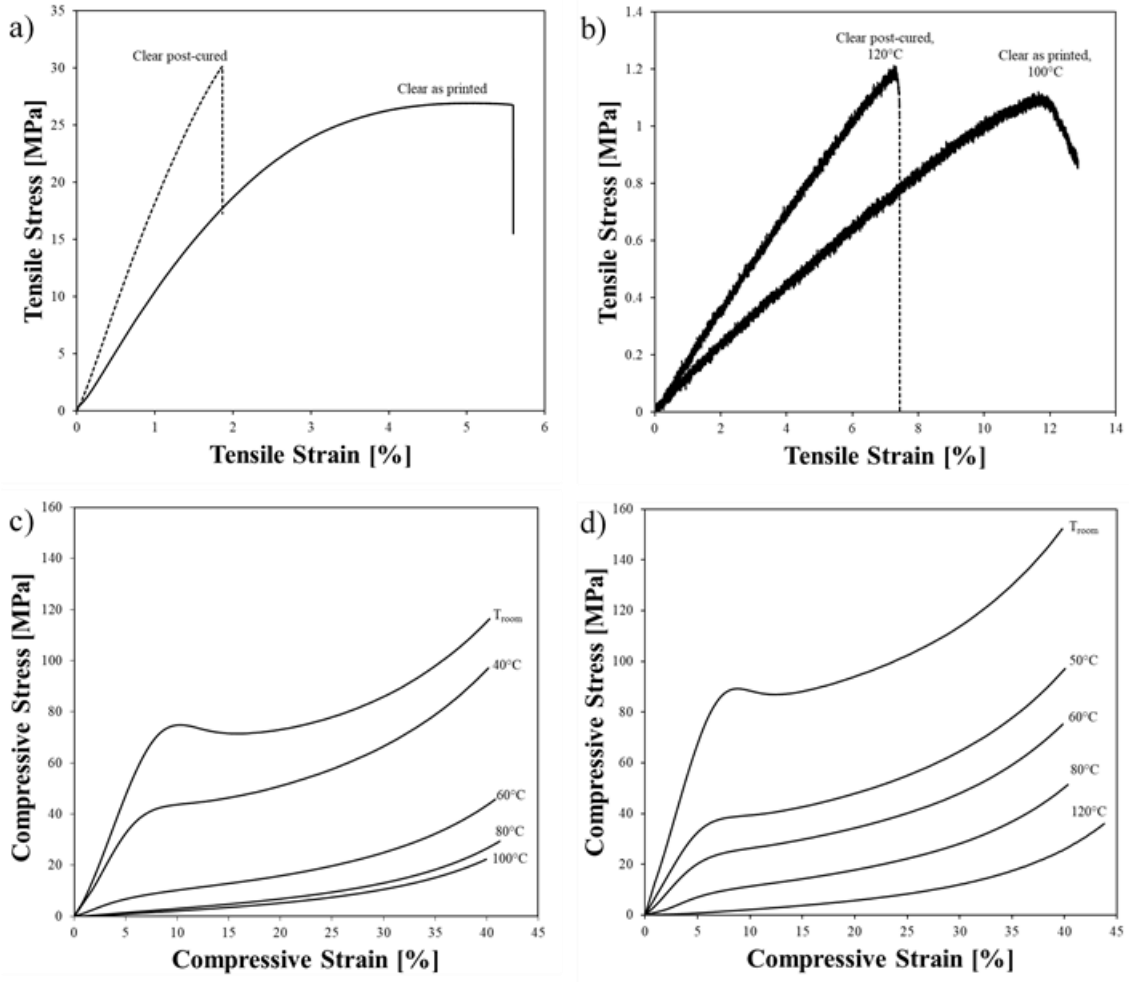

Figure 2.12. Results of mechanical testing carried out in tensile and compressive conditions for the Clear as printed and post-cured. In a) stress-strain response measured at T_{room}; b) stress-strain response measured

above T_g, both in tensile conditions. In c) stress-strain response measured at various deformation temperatures for Clear as printed under compression; d) stress-strain response measured at various deformation temperatures for Clear post-cured under compression

Due to the high crosslink density, the materials behave in a brittle manner, both at room temperature (strain at break <10% for the Clear as printed) and become even more brittle at temperatures above T_g.
Conversely, under the more damage tolerant compressive conditions, it was possible to apply a significant and practically relevant strain level (ε_{app} = 40%) for temperatures both above and under T_g, as shown in Figure 2.12c and 2.12d, for the as printed and the post-cured systems respectively. The Clear system in the as printed state (Figure 2.12c) displayed different mechanical response, corresponding to very different deformational regimes, as temperature increases. More specifically for temperatures up to T_g, an evident elasto-plastic behavior is suggested, with a well evidenced yield point and a softening region before the final hardening; for slightly higher temperatures (60 °C) the occurrence of yielding is only slightly suggested, whereas above this temperature the behavior becomes that typical of an elastomeric material. A similar dependence on temperature was found also for the post-cured system (Figure 2.12d).

Investigation of the temperature-memory effect for the Clear resin

The shape memory ability was studied following a typical programming and recovery cycle. The programming was carried out on cubic specimens at temperatures ranging from room temperature to temperature proper of the rubbery region of the system, deforming them up to ε_{app} under compressive conditions and cooling them under fixed strain to room temperature; programmed specimens were later heated above T_g to stimulate the recovery process. After cooling under fixed strain, for all the Clear systems a large part (around 65%) of the applied deformation is fixed. The remaining part is lost due to the thermal contraction of the dynamometer compression equipment during cooling under fixed strain. The results of the TSR curves are reported in Figure 2.13a for the as printed system and in Figure 2.13b for the post-cured one.

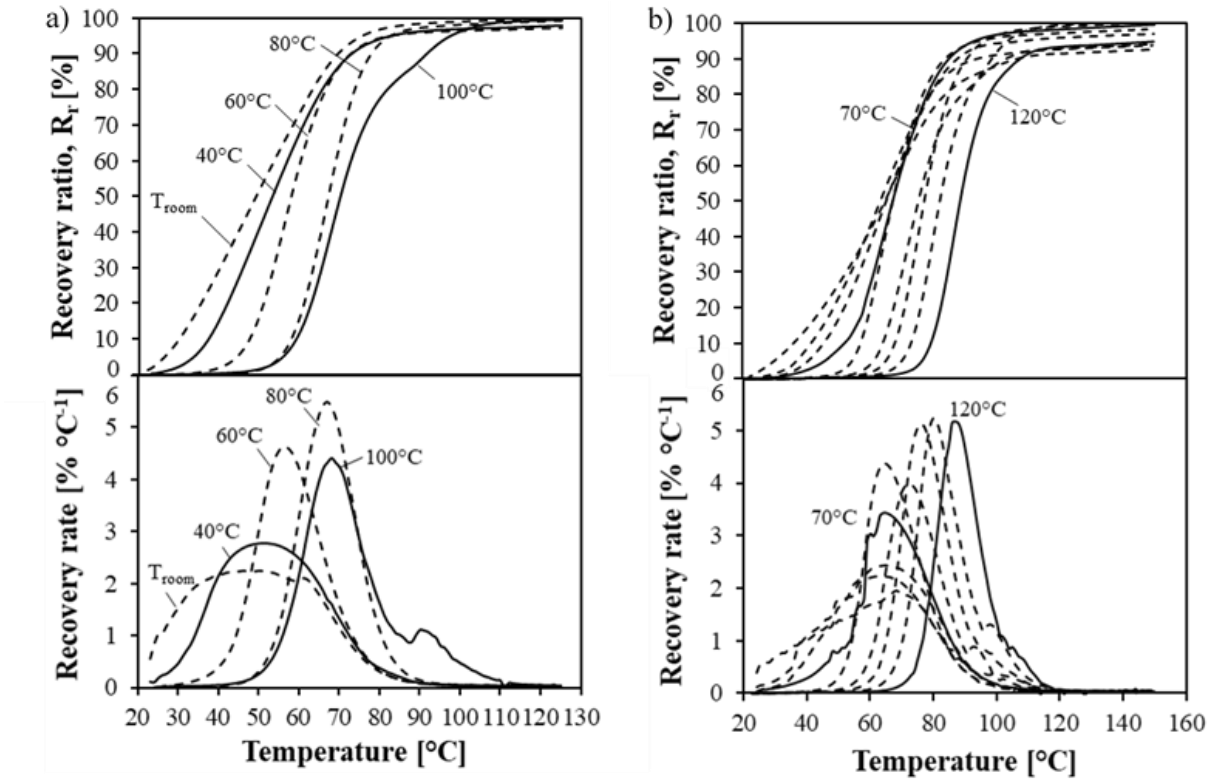

Figure 2.13. Recovery ratio and recovery rate, as evaluated with Equation 2 and 3 respectively, for a) as printed and b) post-cured specimens deformed at various temperatures.

The recovery behavior is shown in the plot both in terms of recovery ratio (*i.e.* the percentage of recovery taking place as temperature increases) and in terms of recovery rate (*i.e.* the temperature derivative of the recovery ratio). The results of the two Clear systems clearly show that both the systems, independently from their partially or fully cured state, are seen to undergo practically full recovery of the original shape (with a final value of R_r = 98-99% for the Clear as printed, whereas slightly smaller values are found for Clear post-cured, yet above 90%). In addition, the recovery behavior is strongly influenced by the deformation temperature, and it takes place on a different temperature region depending on the deformation temperature. In particular, both the onset and the end of the recovery process move to higher temperatures as the deformation temperature increases. For deformations in the sub-T_g region, this could be expected because of the incorporation of slower chain motions in the glassy region further than those ascribed to the main relaxation process. Conversely, such a dependence is usually not shown at higher T_{def}, since for higher temperature recovery usually takes place always at T_g. In particular it may be seen that for higher temperatures (T_{def} from 60 °C for the as printed system, and from 80 °C for the post-cured one) the recovery occurs with a similar narrow trend, but is shifted to higher temperatures as the deformation temperature increases. This results is

interpreted as a consequence of the broader distribution of the segmental relaxation motions activating recovery, and suggest that, as a consequence of the broad glass transition region, T_{def} may be used to control the transformation temperature, with a behavior that closely reminds the typical temperature memory effect.

The recovery rate curves, shown in the bottom of Figure 2.13a and 2.13b, are usually reported to better describe the distribution of the recovery process along the temperature scale. All deformation temperatures are associated to distributed recovery processes, thus leading to a partial overlapping of the peaks; this is partly due to the slow recovery kinetics, as typical of shape memory polymers whose recovery is triggered by T_g. However, this representation offers the possibility to identify deformation temperatures of minimum overlapping: for the Clear as printed material the recovery of specimens deformed at 40 °C and 100 °C displays the least, and only partial, overlapping of the curves, whereas for the Clear post-cured 70 °C and 120 °C are, among those tested, the T_{def} values of minimum overlapping.

One of the potential applications of the temperature memory effect may regard the possibility to obtain multiple or sequential transformations, as a consequence of a proper thermo-mechanical history. To evaluate the possibility to exploit this effect, two experiments were set up on the Clear as printed systems.

The first type of experiment is based on the TSR protocol here employed, but applies a different programming sequence. The programming is based on the two temperatures that have shown to provide minimum overlapping in the recovery rate curves. The specimen is in fact subjected to a double sequential compression, with i) the first step consisting in a deformation at the high temperature T_{high} (100 °C) up to a strain equal to 20%, followed by cooling to a lower temperature (40 °C) under fixed strain conditions; ii) a subsequent step in which an additional deformation of 20% is applied at the low temperature T_{low} (40 °C), and finally iii) the specimen is cooled to room temperature under fixed strain conditions. The thermally stimulated recovery test that followed programming revealed the recovery rate and recovery ratio traces shown in Figure 2.14a.

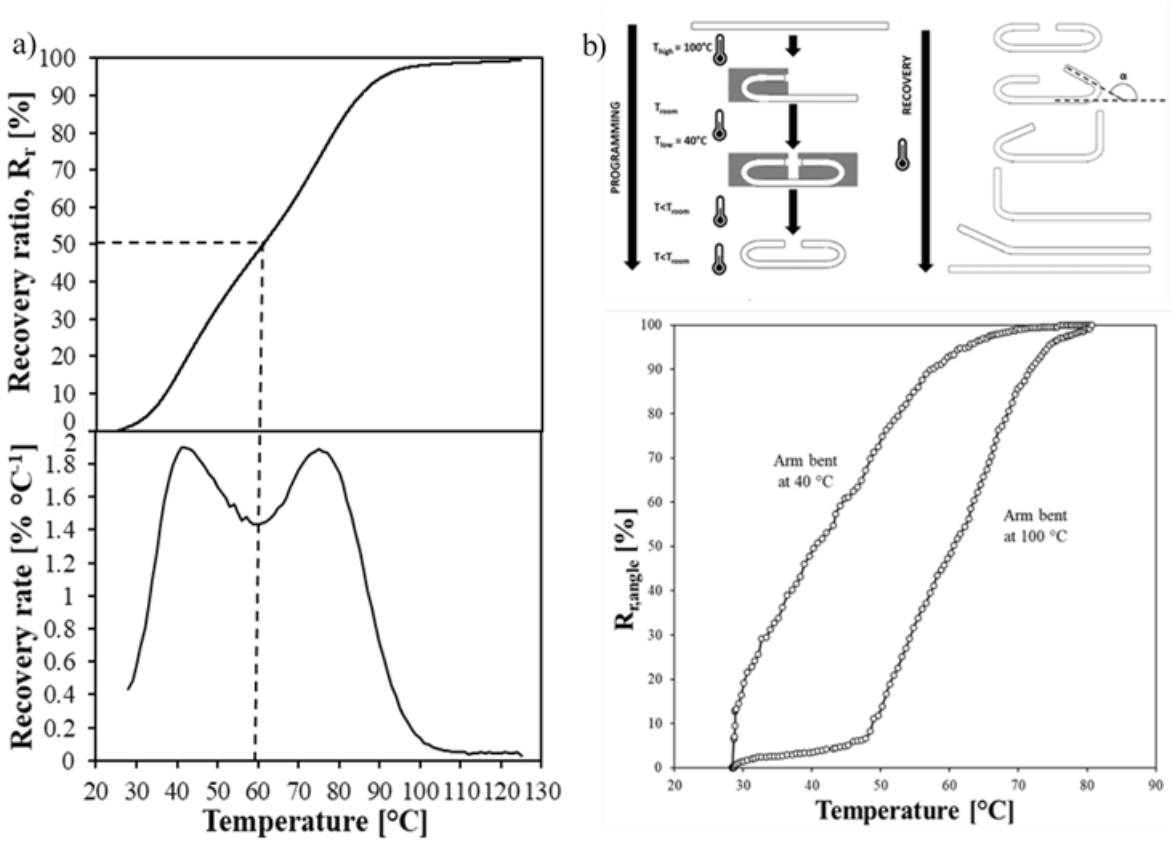

Figure 2.14. Results of two-step programming. In a) two-step compression: results of the TSR test for the as printed material subjected to a sequential double compression history shown as recovery ratio, Rr and recovery rate as a function of temperature. Dashed line: construction line to schematically distinguish the two recovery processes. In b) two-step folding: outline of the programming and of the recovery stage and results for the recovery along a heating ramp of a bar-shaped specimen in its as printed state, with one arm folded at T_{high} = 100 °C and at the other at T_{low} = 40 °C, expressed as the evolution of $R_{r,angle}$.

It can be seen that the recovery process takes place as a function of temperature and is subdivided in two sub-processes that occur in different thermal regions. It is described by two sigmoidal trends, the first one starting at the beginning of the recovery and slowing at 60 °C where the second process begins, as suggested by the relative minimum in the middle of the recovery rate trace. The process leads to a decrease of strain within two smooth steps, each one that may be considered about half of the entire recovery process.

This kind of double-programming suffers from intrinsic difficulties in the experimental setup of the test, especially considering the thermal history to which the material is subjected during the cooling between the high temperature and the programming at the lower temperature. In this stage, the specimen is heated at the

T_{low} and kept for a certain time to allow the sample to equilibrate, thus some stresses can be released. For more complex thermo-mechanical histories, it may be difficult to obtain a clear description of the two peaks in the recovery rate curve of TSR tests, with the possibility of occurrence of a single broader peak hiding in itself the two parts of the recovery.

Therefore a second experiment was designed aiming at giving a better description evidencing the two recovery processes and testing the possibility of sequential deployment and opening sequence that a device made with these materials may display. The extremities of a printed bar were bent at different temperatures so as to monitor the temperature-dependent recovery of the two distinct arms in a temperature-triggered recovery test at a heating ramp approximately of 1 °C/min. The result in terms of $R_{r,angle}$, defined as in Equation 3, *versus* temperature is reported in Figure 2.14b. The two processes are seen to onset, along this ramp, at different temperatures, the second starting with a lag of about 20 °C with respect to the first one, and showing to be practically not leading to any changes on a temperature region on which the other recovers more than 70%. Furthermore, this lag is approximately kept constant within the whole recovery process until the end. This behavior demonstrates that the material is promising for a sequential thermally triggered shape variation.

The possibility to achieve sequential deployment was further studied under isothermal conditions so as to quantify the process rates as a function of time for both the Clear systems.

Isothermal recovery tests, to be reasonably carried out in the time-scale of a lab, were designed with subsequent short isothermal sections (each one 30 minutes long) on the same bent specimen and by increasing the temperature of the observation passing from a section to the subsequent one. This procedure allowed to obtain the evolution of the recovery ratio for an angular motion, as defined in Equation 3, in the time scale for both the extremities bent. By way of example, the typical plot produced is shown in Figure 2.15 for the case of a Clear as printed bar, with an arm bent at 40 °C (Figure 2.15a) and the other one at 100 °C (Figure 2.15b).

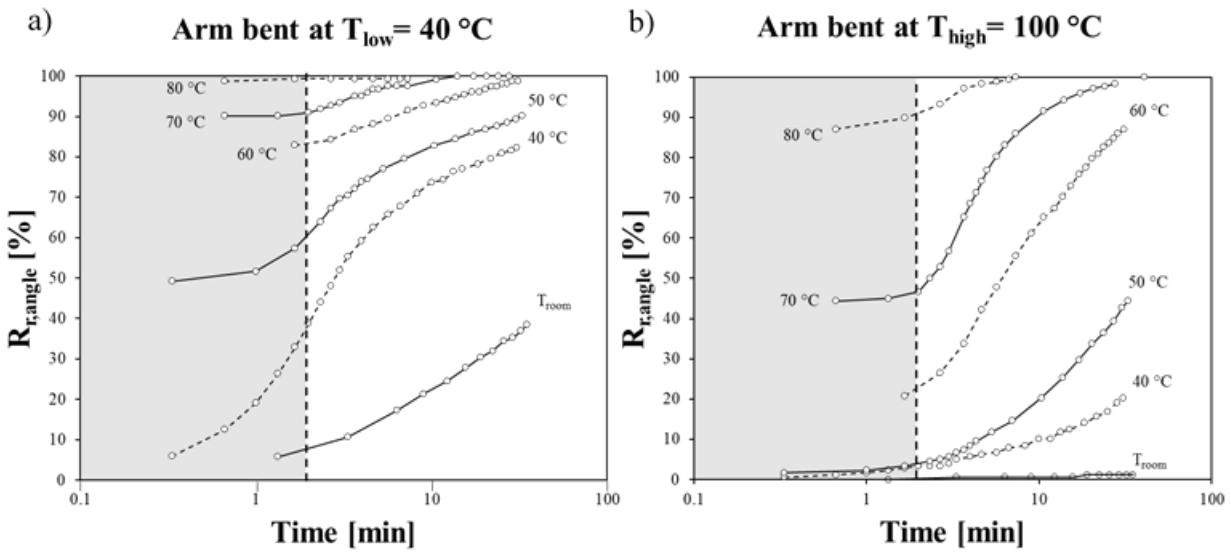

Figure 2.15. Isothermal recovery curves for the arms of double folded as printed bar-shaped specimens: a) extremity bent at T_{low} = 40 °C; b) extremity bent at T_{high} = 100 °C. Solid line: first set of recovery temperatures (T_{room}, 50 °C, 70 °C); dashed line: second set of recovery temperatures (40 °C, 60 °C, 80 °C).

It can be clearly noticed that the same isothermal section produces significantly different effects when looking at the response of the arm bent at T_{high} or the arm bent at T_{low}. Actually, the isothermal segment at room temperature implies a quick and important recovery (about 40% at the end of the 30 minutes) for the arm bent at T_{low}, whereas the same temperature segment does not cause any appreciable effect for the arm bent at T_{high}, as expected. Furthermore, the isothermal segment featuring the highest slope of the recovery ratio combined with the highest percentage of deformation recovered, can be identified with that one at 40 °C for the arm bent at the same temperature, otherwise with that one of 60 °C for the other arm, confirming the lag of 20 °C, already found for the sequential recovery test carried out as function of temperature.

In order to extend the time range within which a description of the evolution of the recovery ratio is possible, towards smaller (10^{-2}) and higher (10^{3}) times (expressed in minutes) covering 5 decades, a time-temperature superposition scheme was applied starting from an isothermal segment corresponding to the chosen reference temperature T_{ref} = 60 °C. This approach is an approximation since the here investigated conditions are far from being considered in the small strain linear viscoelastic regime, however this attempt can be supported by the findings described in literature, both recently, with a similar approach applied for shape memory materials[35] and in the framework of the investigation of the energy storage phenomenon for highly deformed polymers in

the glassy state[36]. This latter approach was extended here and applied also for the case of deformation carried out along and above the glass transition.

The results in terms of master curves for both the Clear as printed system and the post-cured one are reported in Figure 2.16 with full dot markers and with superimposed solid lines to evidence the sigmoidal shape of the curves.

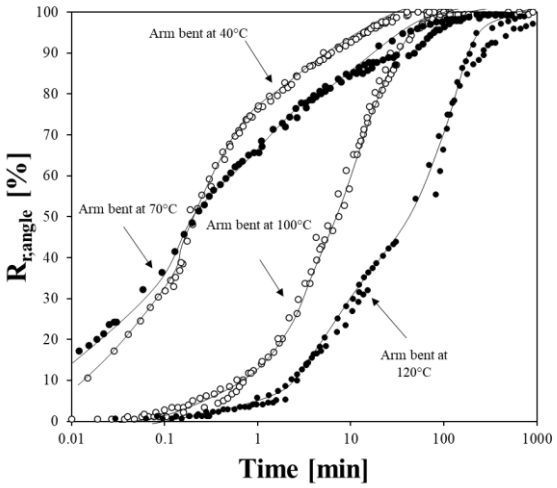

Figure 2.16. Recovery master curves (built at T_{ref} = 60 °C) for the arms of double-folded specimens of the as printed (○) and post-cured (•) resin (solid lines superimposed). In both cases, one arm was bent at T_{low} and the other at T_{high}.

The master curves of the recovery process referring to the two arms are located on well distinguished time scales, onsetting at fractions of a minute for the arms bent at T_{low} and at longer times for the arms bent at T_{high}. In particular, if the delay between the two recovery processes is evaluated in correspondence to the inflection point of the sigmoidal curves, the longer process may be roughly evaluated as 30 times slower than the earlier one for the as printed system, and an even more pronounced delay (about 100 times in correspondence to the inflection point) is found for the post-cured one. This finding, supported by the widening of the glass transition zone after thermal treatment, suggests the possibility to reduce the overlap of two temperature-triggered movements through a post-curing treatment.

Furthermore, the curves shown in Figure 2.16 may be used as a first design tool for the programming of a sequential shape-shifting process based on the herein explored temperature memory effect, for more complicated geometries and structures.

In fact, these results were used to prove the achievement of the sequential self-folding/self-locking clamp introduced in the Design Concept section in Figure 2.7.

The structure in its as printed state was subjected to a two-step programming at the two deformation temperatures previously characterized. The first part consisted in applying a rotation around hinge A to obtain a straight tab at T_{high} = 100°C (Figure 2.17e); then the structure was cooled at T_{room} under the imposed shape. The second part consisted in performing a rotation at the point called hinge B at T_{low} = 40 °C to obtain the second temporary shape (Figure 2.17f). Finally the structure was cooled down to −20 °C. The recovery was studied in isothermal conditions by immersion of the structure in a water bath at the reference temperature for the construction of the recovery ratio master curves (60 °C). As displayed in the sequence of images in Figure 2.17g, at 60 °C the recovery of the double-programmed clamp includes two separate motions along the time scale, allowing, through rotation of hinge B, the end-tab to enter in the hole before rotating to ensure the locking feature. In particular, the first recovery, related to the deformation carried out at T_{low}, takes place within 10 s of the immersion in hot water, whereas the recovery of the second rotation (related to the programming at T_{high}) can be appreciated starting from 20 s of immersion and ending within 5 min, thus being about 30 times slower than the first motion, in fair agreement with the master curve prediction (Figure 2.16).

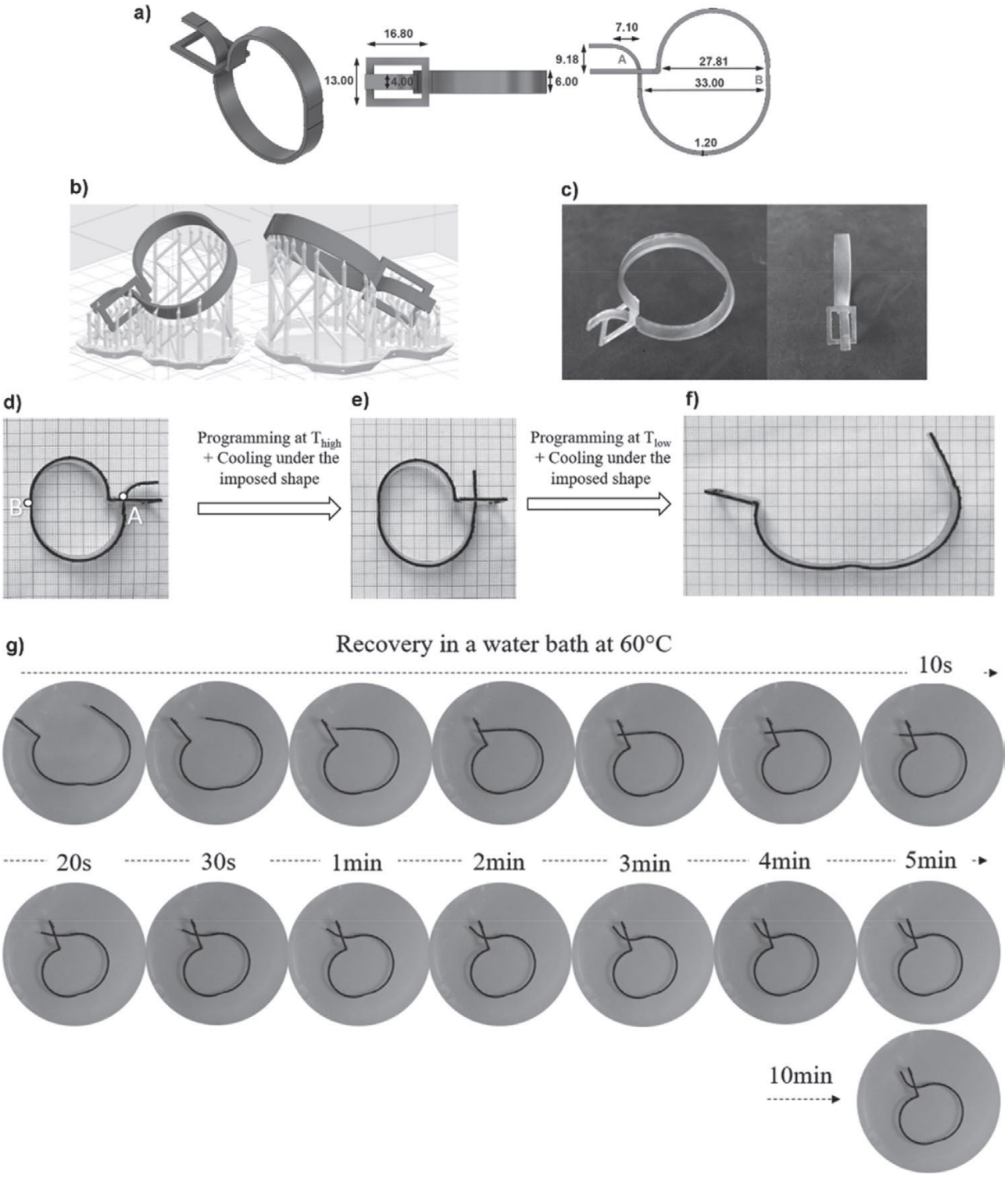

Figure 2.17. Programmable self-locking clamp. a) CAD model; b) orientation on the building plate and support structure generation, and c) 3D printed model. All dimensions are given in mm. Programming of the self-locking clamp: d) permanent shape; e) temporary shape after programming at T_{high}; f) temporary shape after programming at T_{low}. g) Sequence of images during the recovery in a water bath at 60 °C.

The application of the temperature memory effect was proved to be effective also to achieve the sequential shape-shifting capabilities envisioned in the Design concept section also for the auxetic structure of Figure 2.8.

The structure was 3D printed including also grids at its top and its bottom to ease the clamping inside the dynamometer for the basic mechanical characterization regarding the whole structure, as show in Figure 2.18a and 2.18b. Further testing related to the shape memory characterization was performed on the single unit cell represented in Figure 2.18c, chosen to be the sample representative of the structure.

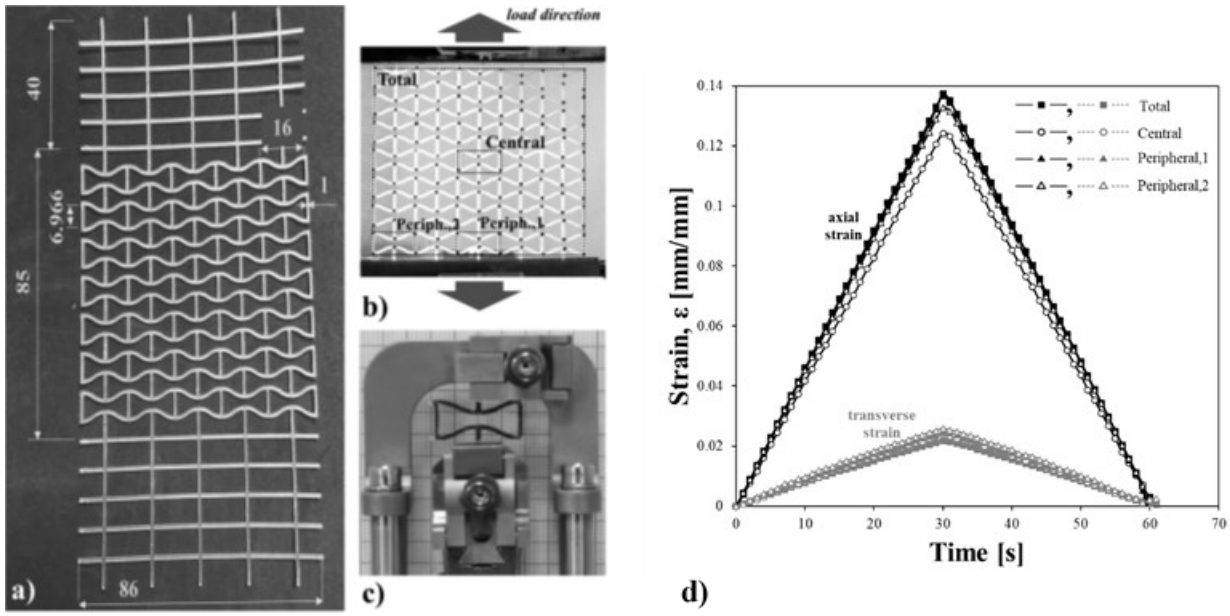

Figure 2.18. a) Investigated 3D printed structure, where thickness is equal to 0.8 mm and all dimensions are given in mm; b) specimen configuration in the tensile tests, with load direction and position of the reference cells; c) specimen configuration in the shape memory test. d) Axial (*i.e.* parallel to the load direction) and transverse (*i.e.* perpendicular to the load direction) strain as a function of time along a loading-unloading test as measured on the whole auxetic structure (Total) and on single cells in various positions (Central; Peripheral,1, Peripheral,2).

In Figure 2.18d the results of loading-unloading test are represented in terms of axial and transverse strain as function of time along the deformation ramp up to a maximum displacement equal to 10 mm. The curves refer to the strain measured for the whole structure (labelled as Total), and for single cells in peculiar positions: the cell in the center of the structure (labelled as Central), and two peripheral cells, one on the outer border and on the major symmetry axis (labelled as Peripheral, 1), the other one on the outer border and on the corner of the

structure (labelled as Peripheral, 2). The curves for the various cells and for the whole structure show an expansion-contraction response during the loading-unloading cycle with a similar trend for all the sampled areas, suggesting an overall homogeneous response on the local and global scale. A fairly linear correlation between axial and transverse deformations was found allowing to measure the Poisson's ratio, which displays a value equal to about -0.18.

A similar investigation on the effect of the deformation temperature on the shape memory response to what was already performed for cubic specimens and reported in Figure 2.13 was carried out on the auxetic unit cell clamped in the DMA under tensile conditions. In this latter set of experiments, it was possible to perform the whole shape memory cycle inside the same machine (the DMA), rather than subdividing the programming and the recovery into two physically different steps in two machines, as it was necessary for the cubic specimens. This protocol allowed to apply a more controlled heating and cooling history, from an experimental point of view, and to more precisely evaluate the shape memory response in terms of the capability of fixing the temporary shape, by measuring the strain fixity index, in addition to the capability of recovering the permanent one, by measuring the strain recovery index.

First of all, in order to visually design and describe the shape memory process taking place in the DMA, a single cell was deformed accordingly to the typical shape memory testing conditions, *i.e.* deforming the specimen well above T_g and cooling below T_g under fixed deformation. The recovery was promoted by progressively heating the specimen up to various temperatures, and suddenly cooling to fix the shape and capture the deformed specimen configuration. The visual control of the whole shape memory cycle allowed to check the deformation conditions employed that regarded the application of an axial elongation to the unit cell equal to 3.5 mm. This value was chosen to induce a significant opening of the cell, *i.e.* the 90% of the value needed for the complete opening without distortions.

The result of the recovery is reported in Figure 2.19 and shows the progressive reduction of the normalized displacement and the deformed configuration for each isothermal sampling step.

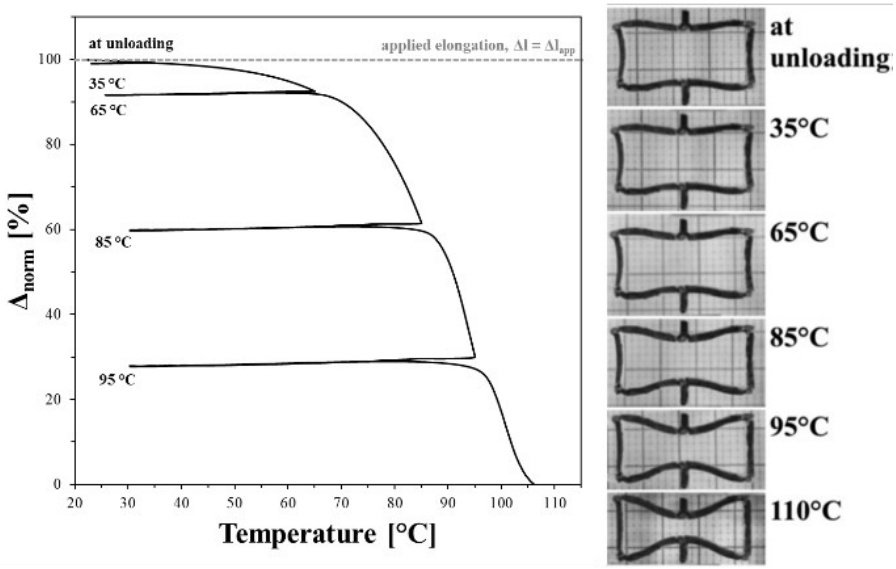

Figure 2.19. Shape memory response of the cell after a deformation at T_{def} = 100 °C in the recovery step, with sampling of the specimen shape at various temperatures in order to have visual representation of the effect.

Figure 2.19 suggests the possibility to fix a fully deployed shape at unloading and to maintain the shape practically unchanged up to 65°C. After, the recovery process occurs through a contraction of the cell, with a process gaining its maximum speed at 95 °C, finally leading to full recovery, and to an overall area contraction of about 42%.

The results of the recovery step for the various deformation temperature employed in the range of T_{room} to 100 °C on as printed unit cells are shown in Figure 2.20a and 2.20b (black and grey solid lines), in terms of the evolution of the normalized displacement and recovery rate as a function of temperature, as evaluated by Equation 4 and 7, respectively.

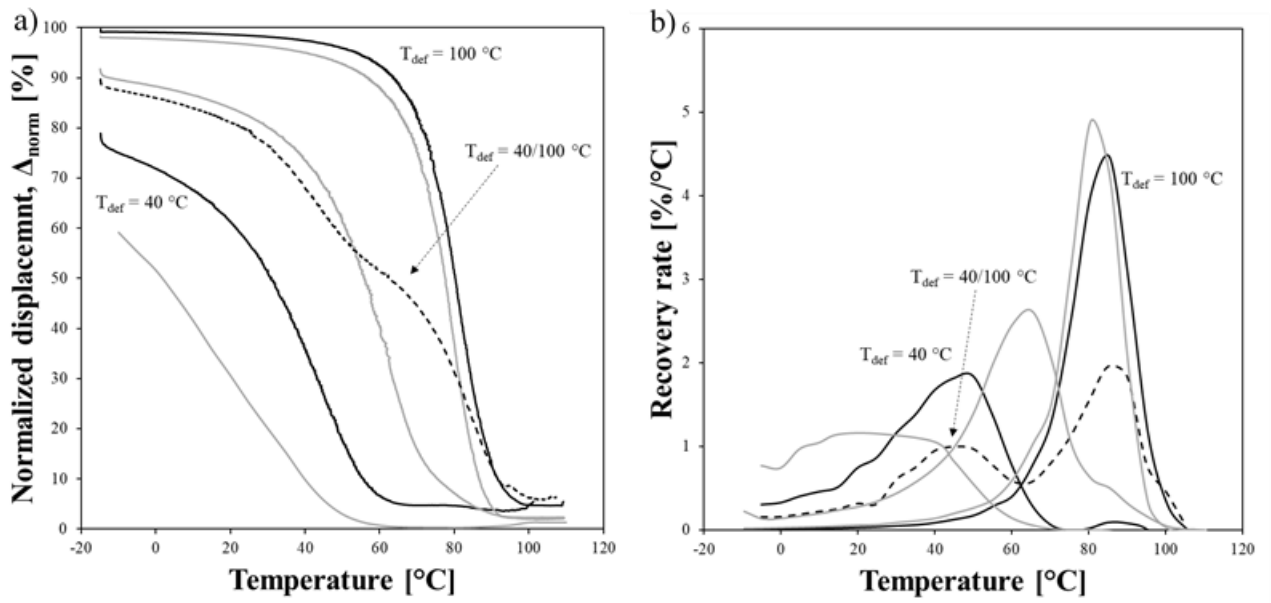

Figure 2.20. a) Normalized displacement, Δ_{norm}, and (b) recovery rate *versus* temperature curves for specimens deformed up to the full opening of the cell at various T_{def} from T_{room} to 100 °C (black lines: 40 °C and 100 °C; dashed black lines: two-step deformation history, half at 100 °C and half at 40 °C; grey lines: T_{room}, 60 °C, 80 °C).

A first effect of the deformation temperature regards the effectiveness of fixing the applied strain. In fact, after cooling, a portion of strain may be recovered during unloading. The strain fixity values, quantified in Table 2.2, show that only deformation temperatures close or above T_g allow full fixation of the deformed configuration, while for deformation temperatures below T_g lower fixity values are found as temperature decreases. Deformation at room temperature still allows to fix more than half of the applied strain, and, interestingly, a slightly higher temperature (T_{def} = 40 °C) allows to fix up to about 80% of the applied deformation.

T_{def} [°C]	Strain fixity, SF [%]	Strain recovery, SR [%]	T_{flex} [°C]
20	59	100	25
40	77	95	47
60	90	98	65
80	98	98	82
100	99	95	85

Table 2.2. Effects of the deformation temperature (T_{def}) on strain fixity, overall strain recovery and on the inflection point temperature of the sigmoidal recovery (T_{flex}), as measured on specimens subjected to a same amount of elongation (Δl_{app} = 3.5 mm).

The results also show that for all the deformation conditions the applied elongation is almost fully recovered (*i.e.* strain recovery between 95% to 100%), the residual portion being presumably partly related to slipping in the DMA machine grips and to some flexural setting of the cell in a more stable shape. The recovery is confirmed also for this geometry to take place on a different temperature region depending on the deformation temperature, in the fashion of the temperature memory effect. All the curves follow a sigmoidal trend, whose inflection points are defined by the inflection temperature, T_{flex}, listed in Table 2.2. T_{flex} values ranged from 25 °C to 85 °C and in particular, they are strictly related and almost coincident to the corresponding deformation temperature. Furthermore, deformation temperatures below T_g are associated with a broader recovery process which incorporates slower chain motions in the glassy region further than those ascribed to the main relaxation process; by contrast deformation close or above T_g determines a narrow recovery process driven by entropic forces that become effective when chains mobility increases on the basis of the main relaxation process, *i.e.* gaining its fastest rate at T_g.

In Figure 2.20a and 2.20b it is represented also the third set of test (dashed lines) consisting in the application of a two-step stretching deformation performed at the two temperatures providing the biggest separation of the recovery processes (100 °C and 40 °C). The recovery process occurred as two sequential sub-processes. Each process led to a recovery of about half of the whole recovery process and followed sigmoidal trend. In particular, as confirmed by the peak locations, each sub-process showed a distribution very similar to the one shown by the single stretched system deformed at the corresponding T_{def}. Furthermore, also the strain fixity value is at the halfway between the one characteristic of the deformation at 40 °C and the one related to the deformation at 100 °C.

Finally, another two-step deformation history was applied by taking inspiration from the sequence of shape changes presented in the Design Concept section, as illustrated in Figure 2.8. For an easier and improved characterization of the shape memory performances as well as for consistency with the previous

characterization methods, the out-of-plane bending carried out at 100 °C and the in-plane stretching at 40 °C were performed on the unit cell, as illustrated in Figure 2.21a. The results of the recovery process are presented in Figure 2.21b, as a sequence of snapshots taken at different temperature points, and in Figure 2.21c with the evolution of two deformation variables related to the in-plane and out-of-plane recovery. The contraction of the cell, measured with the normalized displacement, occurs at low temperature, onsetting right after unloading and being completed at about 60 °C, while the flattening of the cell, measured by the normalized width, onsets around 50 °C and is completed around 90 °C. The two recovery processes are thus well separated on the temperature scale, allowing for sequential motions of a certain complexity and that might be applied easily also to the whole auxetic structure.

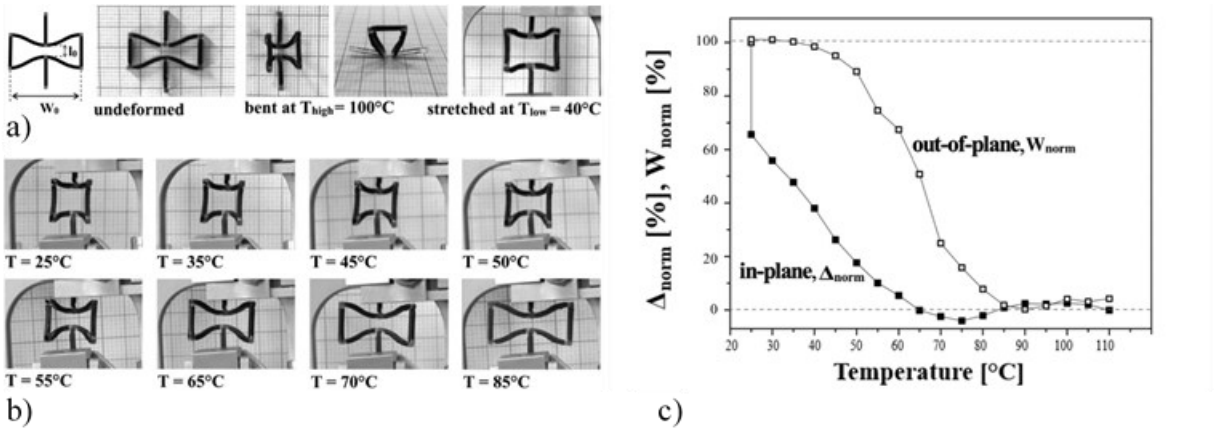

Figure 2.21. a) Two-step deformation, b) shape recovery, and c) recovery curves for a single cell subjected to a two-step programming consisting of an early out-of-plane bending at T_{high} = 100 °C and a subsequent stretching at T_{low} = 40 °C.

To conclude, 3D printing of shape memory polymers is a research field in which a significant quantity of contribution was presented in these recent years from several points of view, ranging from manufacturing to computational design and materials science. In this chapter, a new approach from a materials science perspective based on the temperature memory effect was introduced and explored in depth. However, there's still room for improvements on the chemistry of shape memory polymers for 3D printing and also on the development of new applications which leverage non-conventional shape memory effects, such as the sequential and multiple effects here presented.

Further studies will be carried out in collaboration with the University of Pavia and with Dr. Davide Battini, and will involve the constitutive modeling of 3D printed materials for an effective and optimal design. The modeling activity will be based on the employment of thermoviscoelastic models calibrated on experimentally derived master curves of storage and loss moduli and implemented in a finite element environment. Various testing conditions will be simulated to validate the model to be later employed as an assistive tool to design optimized shape-shifting motions.

In particular, the design phase will be focused on targeting auxetic structures and metamaterials. These will be studied in terms of their deformation behavior as a consequence of the application of mechanical cues and of shape memory protocols. For the first aim, the digital image correlation technique will be employed to gain insight on the deformation mechanisms of the structure of interest; for the second topic, interesting shape changes will be investigated and identified with particular respect to prospective applications in the biomedical field. For instance, some advantages correlated to metamaterials, such as enhanced stretchability, large dimensional changes and coupling of in-plane stimulus to out-of-plane deformations or vice versa might be leveraged to design self-expanding stents and/or devices for drug delivery, *i.e.* to inject active principles in a controlled fashion after the application of a mechanical or non-mechanical stimulus.

2.6 References

1. Q. Ge, H. J. Qi, M. L. Dunn, *Appl. Phys. Lett.* 2013, 103, 131901.

2. Q. Ge, C. K. Dunn, H. J. Qi, M. L. Dunn, *Smart Mater. Struct.* 2014, 23, 094007.

3. Y. Mao, K. Yu, M. S. Isakov, J. Wu, M. L. Dunn, H. J. Qi, *Sci. Rep.* 2015, 5, 13616.

4. J. Wu, C. Yuan, Z. Ding, M. Isakov, Y. Mao, T. Wang, M. L. Dunn, H. J. Qi, *Sci. Rep.* 2016, 6, 24224.

5. G. Sossou, F. Demoly, H. Belkebir, H.J. Qi, S. Gomes, G. Montavon, *Mater. Design* 2019, 175, 107798.

6. G. Sossou, F. Demoly, H. Belkebir, H.J. Qi, S. Gomes, G. Montavon, *Mater. Design* 2019, 181, 108074.

7. M.A. Skylar-Scott, J. Mueller, C.W. Visser, J.A. Lewis, *Nature* 2019, 575, 330-335.

8. J.W. Boley, W.M. van Rees, C. Lissandrello, M.N. Horenstein, R.L. Truby, A. Kotikian, J.A. Lewis, L. Mahadevan, *P. Natl. Acad. Sci. USA* 2019, 116, 20856-20862.

9. J.A. Lewis, L. Mahadevan, J.W. Boley, W.M. van Rees, US20200130261A1

10. H.Y. Jeong, B.H. Woo, N. Kim, Y.C. Jun, *Sci. Rep.* 2020, 10, 6258.

11. Y. Liu, B. Shaw, M.D. Dickey, J. Genzer, *Sci. Adv.* 2017, 3, e1602417.

12. Y. Liu, J.K. Boyles, J. Genzer, M.D. Dickey, *Soft Matter* 2012, 8, 1764-1769.

13. M. Bodaghi, A. R. Damanpack, W. H. Liao, *Smart Mater. Struct.* 2018, 27, 065010.

14. K. Yu, M. L. Dunn, H. J. Qi, *Extreme Mech. Lett.* 2015, 4, 9.

15. B. Peng, Y. Yang, K. Gu, E. J. Amis, K. A. Cavicchi, *ACS Materials Lett.* 2019, 1, 410.

16. J. Zhao, M. Chen, X. Wang, X. Zhao, Z. Wang, Z.-M. Dang, L. Ma, G. H. Hu, F. Chen, *ACS Appl. Mater. Interfaces* 2013, 5, 5550.

17. S.-M. Lai, P.-Y. You, Y. T. Chiu, C. W. Kuo, *J. Polym. Res.* 2017, 24, 161.

18. K. Kratz, S. A. Madbouly, W. Wagermaier, A. Lendlein, *Adv. Mater.* 2011, 23, 4058.

19. M. Behl, K. Kratz, U. Noechel, T. Sauter, A. Lendlein, *Proc. Natl. Acad. Sci. USA* 2013, 110, 12555.

20. P. Miaudet, A. Derré, M. Maugey, C. Zakri, P. M. Piccione, R. Inoubli, P. Poulin, *Science* 2007, 318, 1294.

21. T. Xie*, Nature* 2010, 464, 267.

22. T. Xie, K. A. Page, S. A. Eastman, *Adv. Funct. Mater.* 2011, 21, 2057.

23. Y. Bai, X. Zhang, Q. Wang, T. Wang, *J. Mater. Sci.* 2014, 49, 2252.

24. J. Li, T. Liu, Y. Pan, S. Xia, Z. Zheng, X. Ding, Y. Peng, *Macromol. Chem. Phys.* 2012, 213, 2246.

25. T. Ware, K. Hearon, A. Lonnecker, K. L. Wooley, D. J. Maitland, W. Voit, *Macromolecules* 2012, 45, 1062.

26. Z. Ding, C. Yuan, X. Peng, T. Wang, H.J. Qi, M.L. Dunn, *Sci. Adv.* 2017, 3, e1602890.

27. S.J.E. Tibbits, A. Papadopoulou, J.S. Laucks, US10549505B2.

28. M. Wagner, T. Chen, K. Shea, *3D printing and Additive Manufacturing* 2017, 4, 133-142.

29. M. Lei, W. Hong, Z. Zhao, C. Hamel, M. Chen, H. Lu, H.J. Qi, *ACS Appl. Mater. Interfaces* 2019, 11, 22768–22776.

30. Materials data sheet, https://archive-media.formlabs.com/upload/XL-DataSheet.pdf (accessed: November 2020).

31. Clear: photoreactive resin for Formlabs 3D printers—safety data sheet, https://archive-media.formlabs.com/upload/Clear__Resin_SDS_EU.pdf (accessed: November 2020).

32. Flexible: photoreactive resin for Formlabs 3D printers—safety data sheet, https://formlabs-media.formlabs.com/datasheets/Safety_Data_Sheet_EN_-_Flexible.pdf (accessed: November 2020).

33. K. Bandzierz, L. Reuvekamp, J. Dryzek, W. Dierkes, A. Blume, D. Bielinski, *Materials* 2016, 9, 607.

34. O.-V. Laukkanen, H.H. Winter, H. Soenen, J. Seppälä, *J. Non Cryst. Solids* 2018, 483, 10-17.

35. C. Azra, C. J. G. Plummer, J.-A. E Manson, *Smart Mater. Struct.* 2011, 20, 082002.

36. R. Quinson, J. Perez, M. Rink, A. Pavan, *J. Mater. Sci.* 1996, 31, 4387.

Chapter 3

Design and development of a retentive intravesical drug delivery device based on shape memory polymers

The work here reported has been already published in:

A.Melocchi*, **N. Inverardi***, M. Uboldi, F. Baldi, A. Maroni, S. Pandini, F. Briatico-Vangosa, L. Zema, A. Gazzaniga, Retentive device for intravesical drug delivery based on water-induced shape memory response of poly(vinyl alcohol): design concept and 4D printing feasibility, *Int. J. Pharm.* 2019, 559, 299-311

*co-first author

3.1 Introduction

Retentive intravesical drug delivery devices are biomedical platforms loaded with a drug payload supposed to be inserted into the bladder and to safely reside *in situ* for a prolonged period of time (ideally in the order of few weeks) while releasing the drug in a controlled and extended fashion[1]. The development of such devices has received growing interests for the treatment of several bladder diseases, *e.g.* overactive bladder, interstitial cystitis/painful bladder syndrome and bladder cancer[2,3].

In general, there exist two therapeutic approaches for the treatment of bladder diseases, one consisting in oral or systemic administration of the active and the other one regarding the direct instillation of the drug through a catheter in the bladder[4-6]. The former approach, which benefits from an easy way of administration, either orally or intravenously, suffers of issues related to low bioavailability of the active and potentiality of side effects. In fact, when a medication is administered via the oral route, only a fraction of the administered dose reaches the systemic circulation due to incomplete absorption and to the first-pass effect, which is a drug metabolism process, generally exerted by the liver and the gut, resulting in a reduced fraction of the drug available for circulation[5]. By way of example, lidocaine, commonly used as local anesthetic for overactive bladder, experiences a significant first-pass effect. Conversely, by definition, intravenously administration provides the 100% of bioavailability, being the whole amount of the drug available in the systemic circulation; however, ways of administration involving the whole circulation system might cause toxicity and side effects, as in the case of oxybutynin used for overactive bladder[3,4,7,8] or of chemotherapeutic for bladder cancer[9]. Furthermore, systemic therapy might be less efficient when targeting the bladder due to the poor vascularization present in the urothelium, *i.e.* the lining of the urinary bladder[10].

On the other hand, intravesical instillation of therapeutic agents may help in solving some of the aforementioned issues. In fact, it generally requires a lower drug dose, leading to a reduction of possible systemic side effects and it provides site-specific drug delivery which theoretically should increase the exposure of the tissue to the drug[1,3,5]. However, the urothelium, being a protective layer with a lipophilic nature, offers low permeability and reduced cellular uptake for hydrophilic drugs[10]; furthermore the occurrence of drug dilution processes, caused by the continuous urine production at a rate of about 40-80 mL/h, lowers the drug bioavailability and additionally wash-out phenomena happen on urination within a few hours, resulting

in the excretion of the drug. All these considerations lead to the need of multiple and repeated drug instillations in order to prolong the residence time of the drug and to improve its absorption across the urothelium by increasing the drug concentration; simultaneously the practice of serial catheterization poses challenges related to patient discomfort and to an enhanced infection risk[1,3]. In this framework, various strategies have been proposed in order to keep effective concentrations of the bioactive molecules within the bladder, relying on the use of bioadhesive liposomes and polymers, floating hydrogels or thermo-sensitive hydrogels[5,6,10]. The former materials usually consist of formulations with mucoadhesive properties, for example based on chitosan[11], capable of remaining attached to the bladder walls even after urine voiding, whereas the latter systems display a liquid-gel transition upon reaching the temperature of human body resulting in the formation of a drug depot floating on the urine to prevent obstruction[12] or attached to the bladder wall. Also in the case of these systems there are still limitations concerning the residence time, up to a maximum of about 8 h, and limited drug loading capability.

The development of intravesical retentive devices, also called as indwelling devices, might be very helpful in providing direct release of the drug to the bladder over a prolonged period of time, requiring only a maximum of two medical procedures, in correspondence of the insertion and of the removal – if the device is not biodegradable - throughout all the treatment period.

A first retentive drug delivery device was proposed by Situs Corporation under the name of UROS in the early 2000[7,13]. This platform consisted of a void deflated tube of about 10 cm in length and 0.6 cm in diameter that can be inserted into the bladder through a cystoscope. Once *in situ*, a drug solution can be infused into the reservoir of the device through a septum, and released from the cystoscope, leading to a change in the shape of the device upon unfolding. The shape changes are shown in Figure 3.1 as reported in the relevant patent, which displayed the achievement of a crescent shape, which can be retained into the bladder and allowed the controlled release of the drug through a pressure-responsive valve.

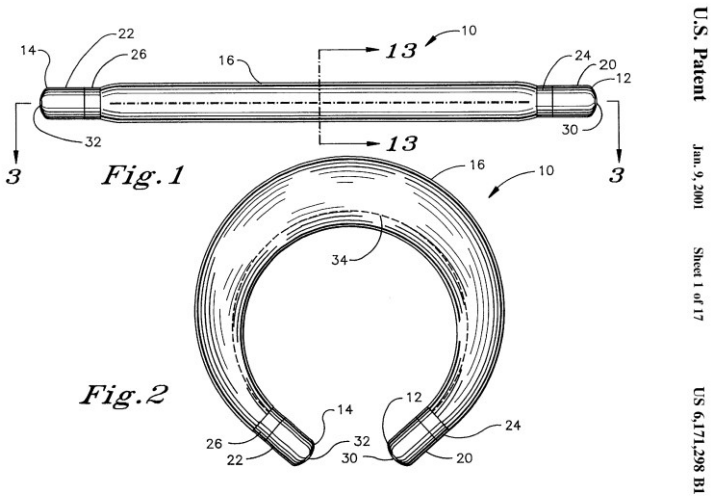

Figure 3.1. The UROS (Situs Corporation) pump in its shape for delivery through a cystoscope (top row) and in its bladder-retentive shape (bottom row)[13].

The device was tested in phase I/II trials in the US involving 16 female subjects, either healthy or diagnosed with overactive bladder. The former group received the device filled with a saline solution as a control and the latter group had delivered the pump filled with oxybutynin, a drug known to block bladder contraction. In spite of the good results obtained in the first clinical trials, further clinical investigation and development was halted without any explanation, suggesting the onset of unexpected issues, perhaps related to the large dimensions characterizing the device.

A second more successful device was designed and tested at the Massachusetts Institute of Technology and later further developed by TARIS Biomedical under the name of LiRIS (lidocaine-releasing intravesical system)[14]. This device is made out of two connected medical-grade silicone tubes, one of them acting as a drug reservoir unit and the other one ensuring the bladder-retentive function. A picture of the device in its bladder-retentive shape is shown in Figure 3.2a.

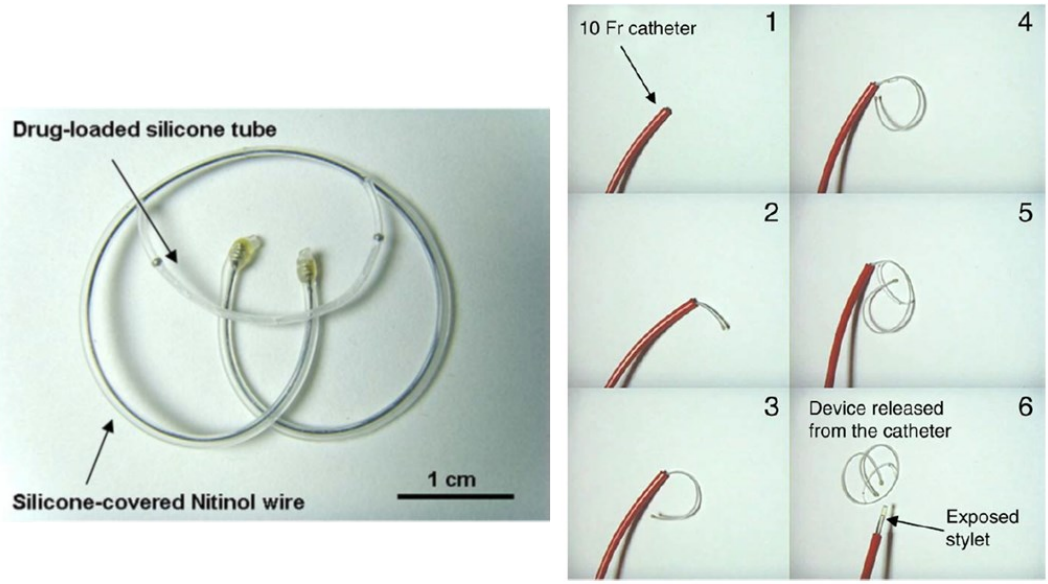

Figure 3.2. The LiRIS: lidocaine-releasing intravesical system (TARIS Biomedical) device. In a) device in its bladder-retentive shape; in b) sequence of the shape changes following insertion in a cystoscope[14].

The drug reservoir unit contains lidocaine, *i.e.* an active ingredient commonly used to treat patients with interstitial cystitis/painful bladder syndrome (IC/BPS), and consists of a water permeable silicone with an orifice acting as an osmotic pump to release the drug. Bladder retention is achieved through shape changes of the device enabled by the employment of a superelastic metallic alloy. More in details, a Nitinol wire was set in a "pretzel-like shape" with a thermal treatment and then covered with a silicone tubing of about 0.9 mm in diameter; the silicone-covered Nitinol wire was then straighten up for the delivery inside a cystoscope and once emerged through the cystoscope, it recovered its deployed shape capable to be retained inside the bladder, as shown by the pictures in Figure 3.2b following the shape changes of the device. The device was tested in clinical trials in healthy volunteers and IC/BPS patients. It was shown to be retained into the bladder while releasing the therapeutic drug into urine over a period of 2 weeks, before being retrieved with a cystoscope and resulting in overall improvements in patient conditions with reduction of pain, urgency and voiding frequency[15]. More recently, TARIS Biomedical proposed a similar device, named GemRIS™, which continuously delivers gemcitabine into the bladder over a period of 7 days for the treatment of bladder cancer[16], as outlined in Figure 3.3.

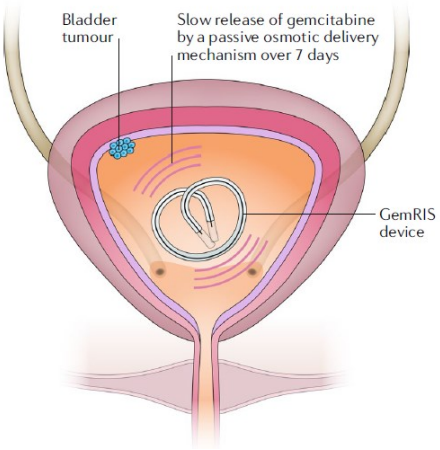

Figure 3.3. GemRIS intravesical delivery system for the treatment of bladder cancer[17].

The device consists of a similar pretzel-like silicone tubing, 5 cm long, which can be delivered using an 18 Fr (*i.e.* 6 mm of outer diameter) ureteric catheter tool and it can be removed by grasping forceps and flexible cystoscopy[17]. The retention of the drug delivery system into the bladder leads to a prolonged exposure time, ensuring higher efficacy of the drug, resulting in a reduction of the tumor size in a significant amount of patients as evaluated in a phase 1b clinical study.

In conclusion, these retentive intravesical drug delivery systems were proved to hold a great potential for the treatment of several diseases, yet they need further improvements with respect for example to the insertion and retrieval procedures, which can be quite invasive since using a cystoscope instead of a catheter, and can cause patient discomfort.

The focus of this chapter is on exploring the possibility of achieving shape changes functional to bladder retention by employing shape memory polymers, inherently capable of large shape-shifting motions. The use of SMPs manufactured by 3D printing may be beneficial to the aim of obtaining complex shape changes potentially useful to enable retention and they might add also other functionalities to the device, such as biodegradability or bioerosion, eliminating the need for removal of the device.

The work presented in this chapter was carried out in collaboration with Dr. Alice Melocchi, Marco Uboldi, Prof. Lucia Zema, Prof. Alessandra Maroni and Prof. Andrea Gazzaniga from the Biopharmaceutics and Pharmaceutical Technology Laboratory of the University of Milano and with Prof. Francesco Briatico-Vangosa (Politecnico di Milano).

3.2 Design Concept

The approach selected for the design and development of a novel retentive intravesical drug delivery platform in this work was based on the shape-shifting capability displayed by shape memory polymers. In particular, one of the main design and experimental effort to be faced regarded the achievement of a "biocompatible" shape memory effect. In fact, given the application targeting a device to be inserted into the human body, several requirements concerning the safety of the platform have to be fulfilled, starting from the choice of the material, that has to be biocompatible and approved by the regulatory agencies, to the design of a proper actuation stimulus to trigger the shape changes. With specific interest to this latter point, it is known that several actuation stimuli are available to promote the recovery of the permanent shape, among whom there are the exposure to direct or indirect heating, to electric/magnetic fields, to light, to variation in pH and or to solvents, depending on the specific chemistry or structure of the material of choice[18-20]. A major consideration for the selection of the external stimulus regarded the need to be compliant to physiological conditions in an easy fashion for the final *in vitro* or *in vivo* implementation. In fact, the device should be administered through a catheter in its compact temporary shape and, once in the bladder, it should recover its permanent shape, *i.e.* the one that has to be bladder-retentive, only thanks to the exposure to physiological conditions, as outlined in the scheme shown in Figure 3.4.

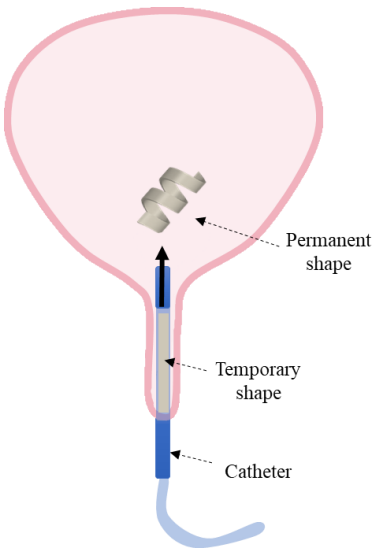

Figure 3.4. Drawing for the conceptual mechanism proposed for the retentive intravesical device developed in Chapter 3: the device in its temporary shape is administered through a catheter and once in the bladder it recovers its permanent and bladder-retentive shape.

The goal set for the working mechanism led to the exclusion of light and electromagnetic fields as actuation stimuli because of the added difficulty of either including a component in the system as the source of the desired wavelength or requiring external additional equipment for the application of the electromagnetic field. The physiological conditions that can be exploited as a triggering stimulus consist of an environment at about 37 °C, considered as the standard body temperature T_{body}, and surrounded by the presence of urine fluids, of whom the major component is water. Therefore, the exposure to heat, at approximately T_{body}, or to water and or the synergistic combination of the two effects, are considered of interest for this specific application. Especially, among shape memory polymers, those ones exhibiting water-induced shape memory response, good hot-processability and swellable/erodible response (*i.e.* able to interact with aqueous fluids ultimately dissolving/eroding), appeared advantageous as main components for the delivery system. Indeed, such materials undergo a glass-rubber transition when in contact with biological fluids with formation of a gel, the dissolution/erosion behavior of which depends on the relevant viscosity and, therefore, on the polymer molecular weight.

The water-induced shape memory response is a peculiar case of the solvent-activated or chemo-responsive shape memory effect. The working mechanism is very similar to the one characteristic of thermo-responsive shape memory polymers. In fact, the recovery is activated in both cases by the increase of macromolecular mobility occurring over transition regions in polymers; however, instead of achieving the increased mobility by heating above the transition temperature, in the case of the solvent-activated shape memory effect the recovery is triggered by lowering the transition temperature and increasing the flexibility of the chains by means of softening, swelling and or dissolving, derived from the interaction of the polymer with the solvent molecules[21]. Specifically, as it is known from the theory of polymer solutions, the solvent molecules penetrate into the polymer, they mix with it, and act as a plasticizer through chemical or physical interactions leading to a decrease of the internal energy of the material and consequently of its glass transition temperature[22-23]. There can be chemical/polar interactions and physical swelling effects, both contributing to shape changes, however the former kind of interaction can be reversible by removing the bonded solvent for example through evaporation, whereas the latter ones cannot be recovered because they involve a volume change. One of the first demonstration of shape recoveries driven by chemical interactions with solvent that reduced the glass transition temperature of a system was presented for the case of a polyurethane shape memory polymer[24,25]. It

was found that the recovery could be activated by immersion in water, causing the decrease of the glass transition temperature as a consequence of the bound water which weakened the hydrogen bonding between N-H and C=O groups of the polyurethane. Furthermore, the interactions resulted reversible because, upon heating above specific temperatures, the bound water could be removed and the glass transition temperature returned to its original value under dry conditions. Similar plasticizing effects caused by the immersion in water were found also for other materials, in particular for polyvinyl alcohol (PVA)[26-30], having hydroxyl groups on its backbone which represent sites for water to bond.

On the basis of these findings reported in the literature, in this chapter, a thorough characterization of the water-induced shape memory effect for pharmaceutical grades of PVA manufactured by 3D printing and by extrusion, as a control, was carried out and reported. The novelty proposed regards the exploitation of their smart response to design a bladder-retentive device, in the framework of 4D printing, here for the first time applied in the pharmaceutical field.

3.3 Materials

The model material chosen to investigate the water-induced shape memory effect and its application to the development of intravesical drug delivery platform was poly(vinyl alcohol) (PVA) of pharmaceutical grade, purchased from Nippon Gohsei. The grades used in this work were Gohsenol™ EG 05P and Gohsenol™ EG 18P (Nippon Gohsei, J), characterized by viscosity values of 5.3 and 18.0 mPas (measured at 20 °C in a 4% solution) respectively, thereafter called PVA05 and PVA18. Other materials used were glycerol, from Pharmagel, as a plasticizer and caffeine, from A.c.e.f., as a model tracer molecule.

Different PVA-based formulations were kindly manufactured by the group of Biopharmaceutics and Pharmaceutical Technology at the University of Milano with hot-melt extrusion and 3D printing techniques. In the following lines, the preparation of the formulations and the manufacturing of the samples are briefly reported.

The PVA powders were dried in an oven at 40 °C for 24 h and then either used on its own to prepare unplasticized samples or employed to prepare plasticized PVA formulations by adding glycerol as the liquid plasticizer dropwise while continuously mixing inside a mortar. 15% by weight of glycerol, calculated on the dry polymer, was used and the resulting mixtures, indicated as PVA05GLY and PVA18GLY depending on the grade of PVA used, *i.e.* PVA05 or PVA18 respectively, were further dried in a oven at 40 °C for 8 h. Afterwards, grinding of the mixtures was performed with a blade mill in order to recover only the < 250 μm powder fraction. For the formulation containing caffeine as a tracer molecule, labelled as PVA05GLY-CFF, the caffeine powder, previously dried in an oven at 40 °C for 24h, was mixed with PVA05GLY in a 1:9 ratio immediately before manufacturing of the samples.

Samples of the various formulations were prepared by hot-melt extrusion (HME) and fused deposition modeling (FDM) 3D printing according to the three geometries shown in Figure 3.5, *i.e.* a straight bar (I-shaped bar), a U-shaped bar and a helix with rectangular cross-section.

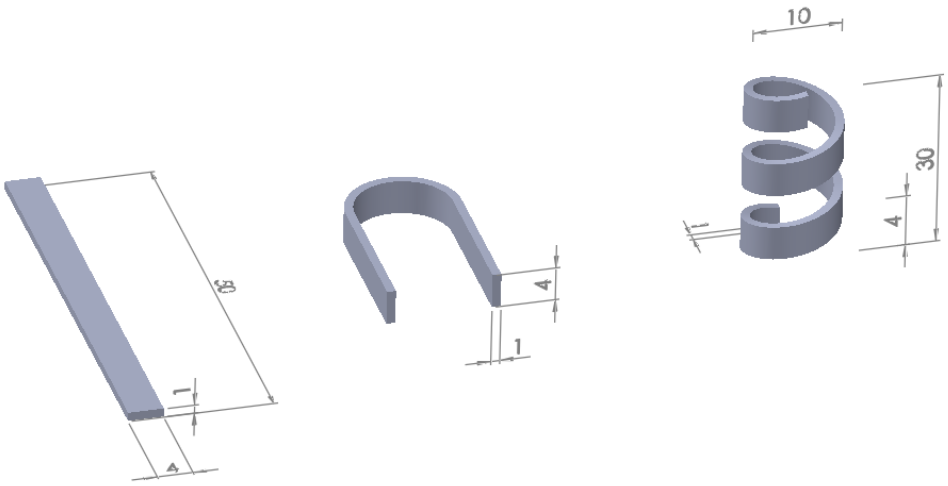

Figure 3.5. CAD drawings with quotes of the I-shaped bar, the U-shaped bar and the helix.

A twin-screw extruder (Haake™ MiniLab II, Thermo Scientific, US-WI) with counter-rotating screws and equipped with a rectangular cross-section die (4x1 mm^2) was used for hot-melt extrusion and the optimized processing conditions are reported in Table 3.1.

Material	HME			FDM
	T [°C]	Screw speed [rpm]	Torque [Ncm]	T [°C]
PVA05	200	100	190	200
PVA05GLY	170	100	100	180
PVA18GLY	200	100	220	n.d.
PVA05GLY-CFF	175	100	120	185

Table 3.1. Processing parameters used during HME and FDM for the various formulations. n.d.= not determined because of unfeasible manufacturing.

I-shaped bars were cut by extrudates with a length of 50 mm, whereas U-shaped bars and helixes required post-processing of the extrudates. More in details, U-shaped bars were obtained by bending the freshly extrudates still hot around a cylindrical stainless steel tool of 15 mm in diameter and waiting them to cool down in order to set the U shape as the permanent one; likewise, the helix geometry was achieved by wrapping the hot extrudate around a purposely developed stainless steel tool with a diameter of 6 mm and a grove with turns for the helix on it with a pitch of 5 mm.

For FDM, in-house made filaments based on the selected formulations needed to be prepared and this was accomplished by using the twin-screw extruder equipped with a custom-made aluminum circular die of 1.80 mm in diameter, as detailed by Melocchi *et al.*[31]. The extruded filaments were manually pulled and forced to pass through a caliper set at 1.80 mm, verifying every 5 cm in length their diameter and discarding those ones with a diameter greater than 1.80 mm. Portions of 25 cm long of the filaments were fed to a Kloner3D 240® Twin (Kloner3D®) 3D printer with a 0.4 mm nozzle, setting the infill to 100%, the layer height to 0.10 mm, the printing speed to 23 mm/s and the separation gap for raft and supports to 0.5 mm. The three geometries were designed using Autodesk® Autocad® 2016 software (Autodesk Inc.), exported in .stl format and used in the 3D printer software (Simplify 3D), using Netfab as an additional software to increase the resolution of the virtual geometries if needed.

All the samples, immediately after production, were packed in heat seal alufoil moisture barrier bags.

3.4 Methods

Extruded and 3D printed specimens were both characterized for their thermal and thermo-mechanical properties, their water-induced shape memory response, their fluid uptake and their release performances.

Thermal and thermo-mechanical characterization

Differential Scanning Calorimetry analysis (DSC) and Dynamic-Mechanical Thermal Analysis (DMTA) were performed on samples cut from I-shaped bars.

DSC analyses were carried out by means of a DSC Q100 (TA Instruments) using nitrogen as a purge gas. The thermal program consisted in i) a first heating scan from – 50 °C to 240 °C; ii) a cooling scan down to -50 °C and iii) a second heating scan from – 50 °C to 240 °C. All the scans were run at 10 °C/min. The glass transition temperature T_g was evaluated choosing the second scan since it provided values similar to those of the first one but easier to read. Samples of about 10 mg were employed both in their dry state and in a condition labeled as "wet", *i.e.* after immersion in distilled water at room temperature for 30 min, followed by equilibration under ambient conditions overnight, in a plastic bag.

DMTA analyses were carried out by means of the Q800 (TA Instruments) dynamic mechanical analyzer on bars (gauge length: 15 mm) under tensile conditions in displacement-controlled mode by the application of a displacement amplitude equal to 10 μm while scanning a temperature region from -50 °C to 120 °C at a heating rate of 3 °C/min.

Water-induced shape memory characterization

The shape memory testing specific for the investigation on the use of water as a triggering stimulus for the recovery consisted of a quite standard programming step for fixing a temporary shape and an *ad hoc* designed step for the recovery of the permanent one.

The programming consisted of the following protocol:

i) heating up to the deformation temperature T_{def}, chosen equal to T_g + 35 °C, the glass transition temperature being measured by DSC;

ii) application of a given deformation at T_{def} by the employment of specifically designed fixtures;

iii) cooling under the applied deformation well below T_g and storage of the samples in a freezer at -20 °C prior to the recovery.

The deformation at T_{def} was applied by bending and wrapping the I-shaped, U-shaped bars and the helixes along purposely developed fixtures so as to obtain U-shaped and I-shaped items, respectively starting from the I shape or both the U and the helix shape, as outlined in Figure 3.6.

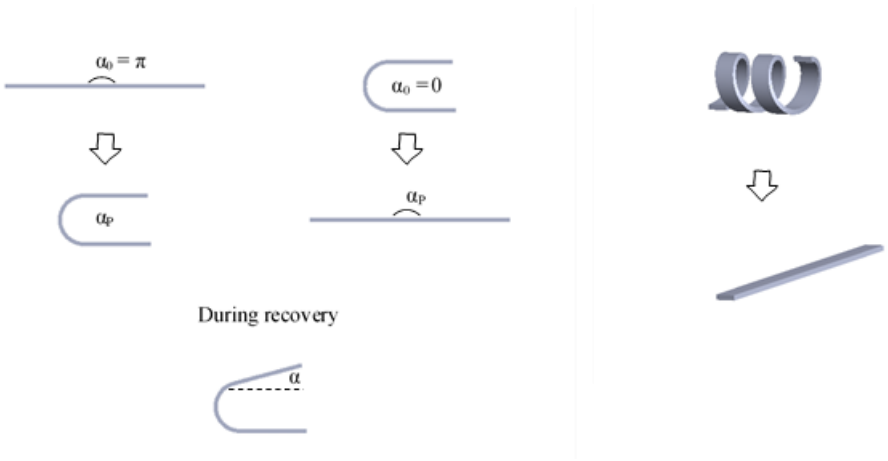

Figure 3.6. Outline of the permanent shapes (top row) and temporary shapes after the programming (under the arrows). Schematic representation of the angles used to define equations for recovery index.

The recovery of the permanent shape was carried out under isothermal conditions both at room temperature and at 37 ± 0.5 °C, by using a thermoregulated bath filled of 100 mL of unstirred distilled water. Pictures of the shape evolutions were taken throughout the recovery using digital cameras (Nikon D700 and GoPro Hero Session) and processes by using a specific software (ImageJ) to measure the variation of selected geometrical parameters, depending on the geometry of the permanent shape, so as to define recovery indexes.

More specifically, recovery index (RI) was defined for specimens with permanent I shape with Equation 1 and for specimens with permanent U shape with Equation 2.

$$RI_I = \frac{\alpha - \alpha_P}{\pi - \alpha_P} \quad (1)$$

$$RI_U = 1 - \frac{\alpha}{\alpha_P} \quad (2)$$

where α is the actual angle during the recovery and α_P is the angle obtained at the end of the programming, being all the angles measured in rad and outlined in Figure 3.6.

The maximum RI value, labeled as RI_{final}, as well as the time to reach RI_{final}, labeled as $t_{RIfinal}$ were also obtained based on the time point after which no more shape changes were observed.

For specimens with permanent helix shape, only RI_{final} and $t_{RIfinal}$ were calculated, by using Equation 3 to evaluate $RI_{final,helix}$

$$RI_{final,helix} = \frac{N_{fin}}{N_0} \quad (3)$$

where N_{fin} is the number of windings at the end of the recovery and N_0 is the number of windings of the permanent shape.

Evaluation of fluid uptake and residual dry mass

The characterization of fluid uptake and residual dry mass was performed on I-shaped bars (on triplicates) immersed in 400 mL of unstirred simulated urine fluid at 37 ± 0.5 °C prepared as indicated by Sherif *et al.*[32]. The specimen was immersed in the fluid upon a stainless steel net, withdrawn at specific time points and gently bottled and weighed. Dry masses W_d were obtained by weighing the sample after drying in a lab oven at 40 °C for 24 h.

The percentage fluid uptake and the percentage residual dry mass were calculated according to Equation 4 and 5

$$Fluid\ uptake\ (\%) = \left[\frac{(W_m - W_d)}{W_m}\right] \times 100 \quad (4)$$

$$Residual\ dry\ mass\ (\%) = 1 - \left[\frac{(W_i - W_d)}{W_i}\right] \times 100 \quad (5)$$

where W_m is the mass of the wet sample on withdrawal, W_d is the mass of the withdrawn sample after drying and W_i is the initial mass of the sample.

Evaluation of release performance

The release profile of tracer-containing samples was assessed by using a USP38 dissolution apparatus (Distek) working at 10 rpm, at 37 ± 0.5 °C, filled with 400 mL of simulated urine fluid as dissolution medium. Fluid samples were withdrawn at specific time points and assayed spectrophotometrically (λ = 206 nm) and the release profile curve was built. The test was done in triplicates. Pictures were taken every 5 s with a camera (GoPro Hero Session) during the whole length of the test.

3.5 Results and discussion

PVA was chosen as a model material on the basis of the considerations reported in the Design Concept section. A library of materials was developed by formulating different molecular weights of PVA together with a plasticizer and/or a tracer molecule and it was screened to characterize thermal, thermo-mechanical, shape memory and release properties and investigate the effect of the formulation on them. The plasticizer chosen was glycerol, as widely reported and tested in other works[33-35]. As a tracer molecule caffeine was used to demonstrate the feasibility of the release approach in the selected retentive drug delivery platform, given its good hot processability (its melting point is equal to 238 °C, that is higher than the highest temperature used during processing, as listed in Table 1) suitable for both HME and FDM. After demonstrating the proof-of-concept mechanism, other model drugs might be selected satisfying both the requirement of hot processability and compliance to the pharmaceutical application.

In light of the motivation of this proof-of-concept study, variability regarding the manufacturing process was introduced so as to compare performances also between 3D printed devices and hot-melt extruded ones, in addition to the variability regarding different formulations. Specifically, so far, FDM has not been applied yet to intravesical devices, thus the hot-melt extrusion technique is useful as a control other than being necessary to produce the polymeric filaments needed for the FDM process.

The specimens were conceived with three geometries (*i.e.* I-shaped bars, U-shaped bars, rectangular cross-section helixes) to explore the design space potentially useful for retentive devices. In particular, the U-shaped bar and the helix might be easily deformed into a bar-like shape suitable for administration and enable bladder retention upon recovery of their permanent, as manufactures, shape; conversely, the I-shapes bar was chosen as a prototypical screening tool on account of the expected ease of fabrication.

By way of example, in Figure 3.7 pictures of the extruded and printed samples based on plasticized PVA05, *i.e.* PVA05GLY, are reported.

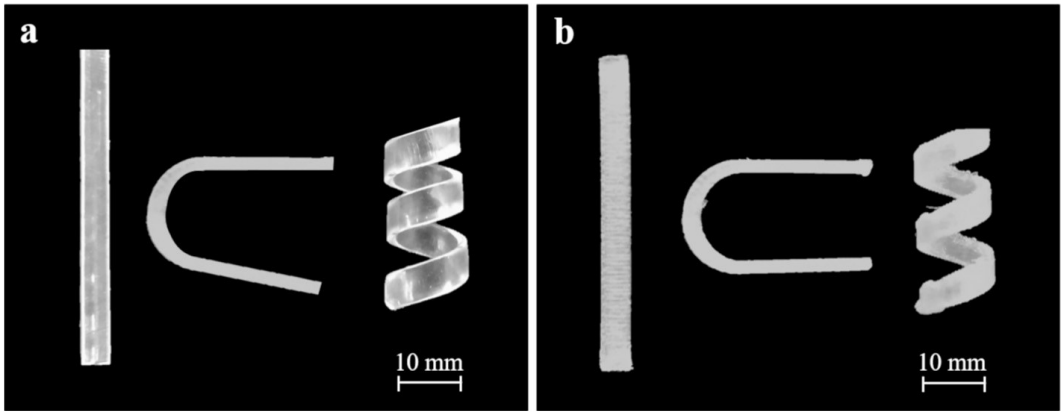

Figure 3.7. Pictures of the three different permanent shapes for the PVA05GLY formulation, as obtained by a) HME and b) FDM.

The obtained specimens were compliant to the target shapes set as the goal, as shown in Figure 3.7. Clearly, FDM offers the advantage of achieving items featuring relatively complex geometries, such as those characterizing U-shaped bars and helixes, directly, whereas HME requires additional processing, *i.e.* bending and coiling along purposely developed tools, before cooling to obtain the same geometries.

The processability by HME and FDM was tested on all the selected formulations observing a generally easier manufacturing through HME. In fact, in the specific case of PVA18-based formulations, the manufacturing through FDM was not feasible due to the high melt viscosity of the polymer, which actually is the grade with the highest molecular weights among those selected. As a consequence, the extrusion pressure required to let the polymer flow through the available nozzle was too high even for plasticized formulations; furthermore, by trying to decrease the viscosity with an increase in the printing temperature, browning of the material was observed suggesting the onset of its thermal degradation. On the other hand, HME was successfully applied to all the formulations with the exception of the unplasticized PVA18 due to required torque values exceeding the maximum allowed with the available equipment. Finally, a generally easier manufacturing was observed for plasticized formulations, with reduced number of printing failures.

Thermal and thermo-mechanical characterization

The thermal and thermo-mechanical screening was performed for all the formulations obtained by HME and FDM on samples cut from I-shaped specimens. More in details, DSC analyses were carried out and focused

on the thermal region featuring the glass transition, since the shape memory effect strictly depends on it. In fact, during the shape memory testing, the value of the glass transition temperature T_g is significant for several aims, since it provides the temperature at which i) the programming of the temporary shape can be performed, here chosen to be the deformation temperature $T_{def} \approx T_g + 35$ °C, ii) fixing and storing the temporary shape without activation of the recovery, generally well below T_g and iii) triggering the recovery of the permanent shape, at $T > T_g$. The aim of this preliminary screening was thus to evaluate how the polymer grade (mainly determined by its molecular weight), the presence of a plasticizer and the interaction with water would affect the glass transition region. Figure 3.8a shows DSC thermograms for all the formulations, comparing samples obtained by HME (solid lines) and FDM (dashed lines) and T_g values, evaluated in correspondence to the inflection point, are listed in Table 3.2.

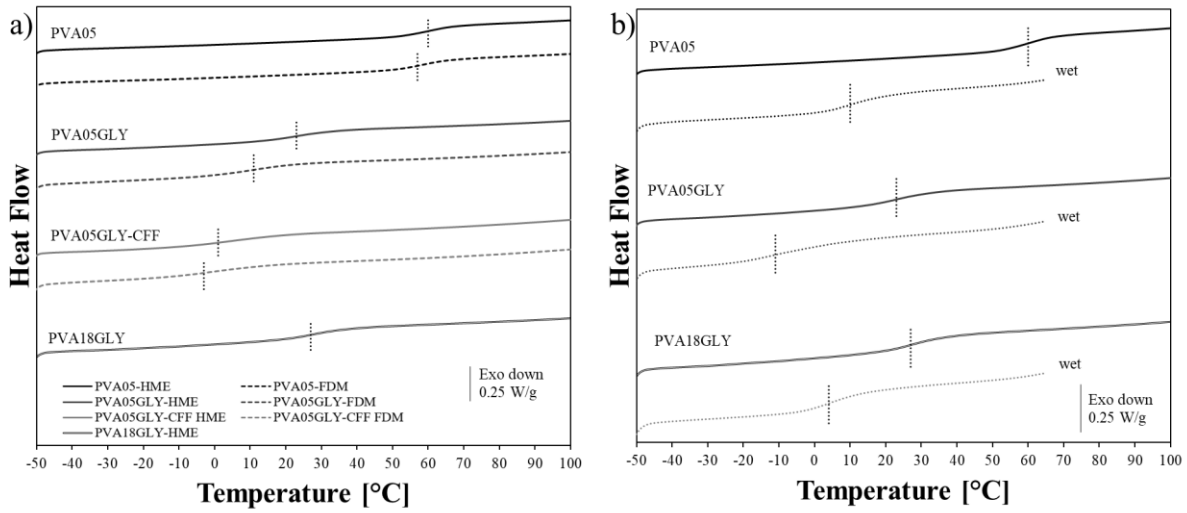

Figure 3.8. DSC thermograms (in the T_g region). Dotted vertical bars indicate T_g. In a) Comparison between specimens obtained by HME (solid lines) and those ones obtained by FDM (dashed lines); in b) comparison between dry (solid lines) and wet (dotted lines) samples obtained by HME.

Material	T_g [°C]	
	HME	FDM
PVA05	60 (10)	57
PVA05GLY	23 (-11)	11
PVA05GLY-CFF	1	-3
PVA18GLY	27 (4)	n.d.

Table 3.2. T_g from DSC analyses for specimens obtained by HME and FDM. Data in brackets refer to wet samples. n.d. = not determined because of unfeasible manufacturing.

Minor differences were found depending on the manufacturing methods, whereas the effect of the plasticizer was significant in leading to a reduction of T_g of about 40-50 °C, from 60 °C and 57 °C to 23 °C and 11 °C, for PVA05 obtained by HME and FDM respectively. The effect of exposure to water on the T_g was also studied and the results are presented in Figure 8b for the case of samples obtained by HME. It can be noted that water uptake leads to a consistent plasticizing effect, by reducing T_g to temperatures less than T_{room}, for all the formulations, with the most marked decrease happening in the case of the PVA05 specimens. Such an increase in macromolecular mobility may be due to the weakening effect exerted by water towards intra- and inter-molecular hydrogen bonds and may result in activation of the shape memory process at room temperature, driven by the exposure to water as a triggering stimulus. DMTA analyses were also used to investigate the effect of the formulation, mainly of the presence of the plasticizer, on the thermo-mechanical properties. In particular, in Figure 3.9 the evolution of the material stiffness across the temperature region involving the glass transition is presented, as storage modulus (E') *versus* temperature traces, evaluated below T_{room} and at T_{def}, corresponding to sample stiffness before and after the shape recovery.

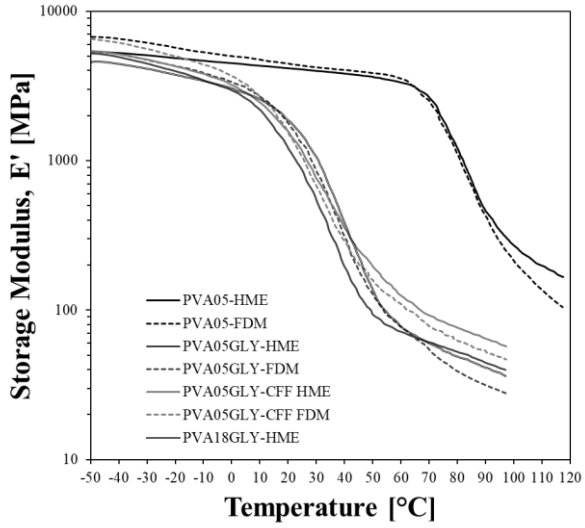

Figure 3.9. Storage modulus versus temperature curves for the various PVA-based formulations obtained by HME (solid lines) and FDM (dashed lines).

From the curves reported in Figure 3.9, data relevant to the values of the storage modulus at T_{room}, labeled as E'_{Troom}, and at T_{def}, labeled as E'_{Tdef}, were derived together with their percentage difference, $\Delta E'$, and listed in Table 3.3. $\Delta E'$ is defined in Equation 6 as:

$$\Delta E'[\%] = \frac{E'_{Troom} - E'_{Tdef}}{E'_{Troom}} \times 100 \quad (6)$$

Material	E'_{Troom} [MPa]		E'_{Tdef} [MPa]		$\Delta E'$ [%]	
	HME	FDM	HME	FDM	HME	FDM
PVA05	4060	4330	440	410	89	90
PVA05GLY	830	2750	70	120	92	96
PVA05GLY-CFF	1110	1010	340	280	70	73
PVA18GLY	1420	n.d.	80	n.d.	94	n.d.

Table 3.3. Storage modulus values at various temperature E'_{Troom}, E'_{Tdef} and their relevant percentage difference $\Delta E'$ evaluated from DMTA analyses on specimens obtained from HME and FDM. n.d. = not determined because of unfeasible manufacturing.

The choice of the storage modulus values to analyze was guided by the need of having representative data points of the whole shape memory cycle. In fact, E'_{Troom} may be representative of the stiffness of the samples in their permanent shape, with the condition that $T_g > T_{room}$, E'_{Tdef} may be an estimation of their stiffness during the shape memory transition and $\Delta E'$ may represent the overall stiffness reduction during the transition. These values offer a first approximation for dry samples, however, when exposed and immersed in water during the shape memory cycle, E'_{Tdef} and $\Delta E'$ may overestimate and underestimate, respectively, stiffness and overall change in stiffness, due to the reduction effect caused by water absorption and eventually by the polymer dissolution. The unplasticized materials displayed a stiff behavior at T_{room}, being in their glassy plateau, with E'_{Troom} equal to about 4 GPa, followed by a one order of magnitude decrease of the storage modulus across the transition with an overall stiffness reduction of about 90%. For all the plasticized formulations, the T_g, as evaluated by DSC, is very close to T_{room}, so that the materials are approaching the glass transition and this impacts the values of E'_{Troom}, which are in the order of 1 GPa. Higher values of E'_{Troom} can be found for specimens obtained by FDM and this is the main difference which might be ascribed to the processing.

Interestingly, the plasticized formulation containing caffeine (PVA05GLY-CFF) displayed higher values of stiffness compared to its corresponding formulation without caffeine (PVA05GLY), suggesting a stiffening effect promoted by the presence of caffeine. At the same time, caffeine is also responsible for a further decrease of T_g close to 0 °C, compared to the values close to T_{room} found for all the other plasticized formulation (Table 2). Such an effect is similar to what has been already observed for caffeine mixed with another thermoplastic polymer for which an antiplasticization effect was recognized[36]. Burgess *et al*.[36] ascribed the increase of stiffness to caffeine increasing the chain rigidity at room temperature by filling a portion of the free volume in the glassy state; the excess free volume of the polymer decreases and disappears at the glass transition temperature liberating the caffeine to plasticize the polymer and resulting in the reduction of T_g. Similar values of T_g, E'_{Troom}, E'_{Tdef} and $\Delta E'$ were found for the formulations containing caffeine, as reported in Table 3.2 and Table 3.3, regardless of the manufacturing method.

Shape memory characterization, evaluation of fluid uptake and release performances

The shape memory response was studied by programming the various permanent shapes at 60 °C, fixing them by cooling down to -20 °C under the deformed shape and activating the shape recovery by immersing the temporary shapes in unstirred distilled water at T_{room}. By way of example, pictures of the recovery for the three permanent geometries and the corresponding different shape motions are represented in Figure 3.10, for different formulations and different manufacturing methods.

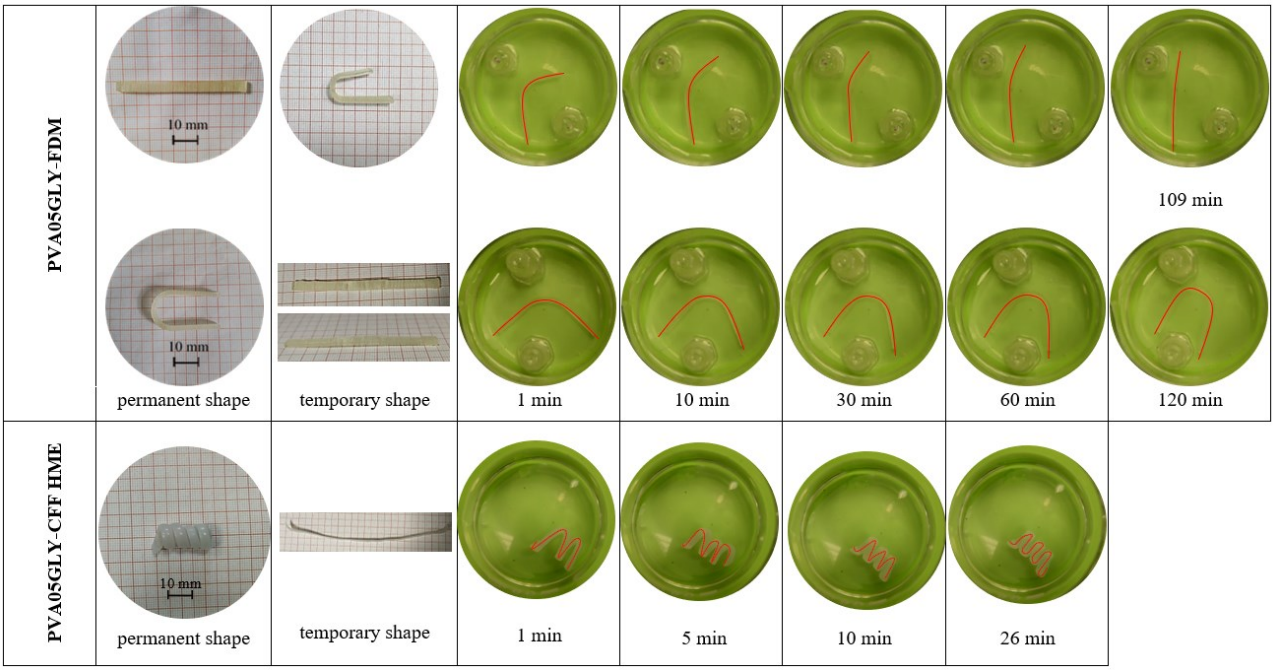

Figure 3.10. Example of pictures taken during shape recoveries carried out at T_{room}. A red solid line is superimposed to highlight the shape changes during the recovery.

For all the shapes tested, the immersion in water was successful in promoting the full recovery of the permanent shape, irrespective of the complexity of the geometry. The recovery kinetics was obviously dependent on the formulation and its consequent profile of properties. Therefore, a thorough study was performed involving all the formulations, the two different manufacturing methods and the various geometries. Recovery curves were built by employing the Equation 1 and the Equation 2, and a selection of them from extruded and printed samples are shown in Figure 3.11a and 3.11b respectively.

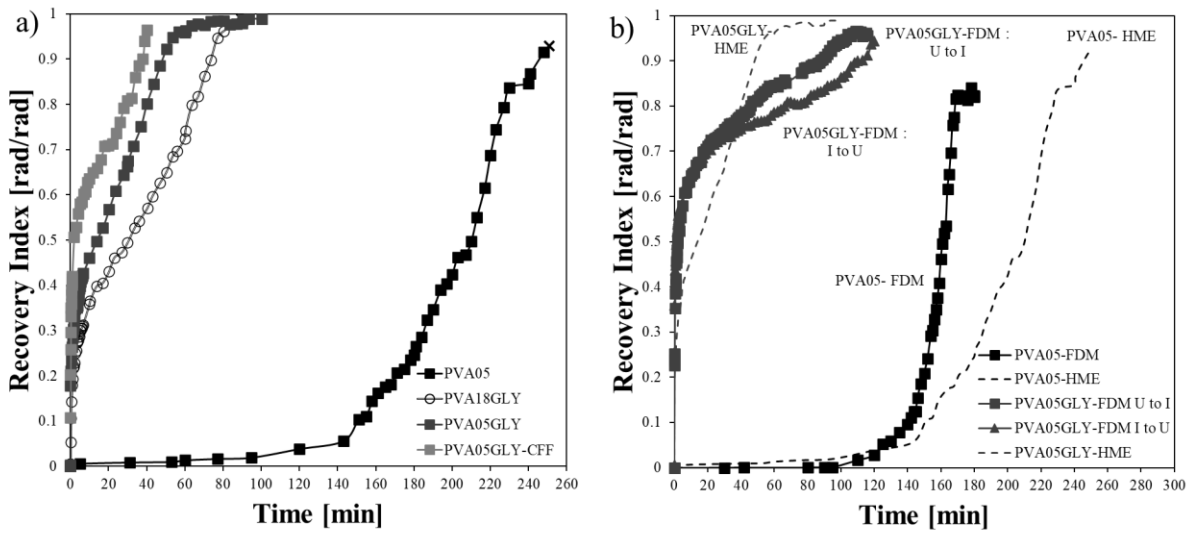

Figure 3.11. Recovery Index *versus* time curves. In a) results for all the formulations prepared by HME involving recovery of the I shape; in b) results for the PVA05 and PVA05GLY formulations processed by FDM (solid lines), compared to the relevant samples obtained by HME (dashed lines) involving the recovery of the I (squares) or U (triangles) shapes.

Two parameters were also calculated to help the comparison of the performances for the different formulations: RI_{final} and $t_{RIfinal}$ to evaluate the maximum recovery index achieved and the time necessary to reach that one, respectively. RI_{final} and $t_{RIfinal}$ values are reported in Table 3.4.

Material		T_{room}		T_{body}	
		RI_{final}	$t_{RIfinal}$ [min]	RI_{final}	$t_{RIfinal}$ [min]
HME	PVA05	0.93	251	0.97	146
	PVA05GLY	0.99	100	0.86	28
	PVA18GLY	0.99	90	0.92	55
FDM	PVA05	0.82	180	n.d.	n.d.
	PVA05GLY	0.97	109	0.88	26

Table 3.4. RI_{final} values and relevant $t_{RIfinal}$ for specimens having a permanent I shape, evaluated by water-triggered recovery tests at T_{room} and T_{body} (*i.e.* 37 °C). n.d. = not determined due to pronounced distortion of the specimen.

The recovery kinetics was found to be strictly dependent on the presence of the plasticizer. In fact, for unplasticized PVA05 obtained both by HME and FDM, the curves show an initial induction phase, about 120 min long, in which recovery doesn't occur, followed by the onset of the recovery. Conversely, for plasticized formulations the recovery starts immediately with a high rate, then slowing down before reaching RI_{final} with comparable times between extruded samples and printed ones, much shorter than the $t_{RIfinal}$ found for the unplasticized formulations. The differences both in the shapes of the curve with the presence of different phases and in the $t_{RIfinal}$ values between unplasticized and plasticized formulations is attributed to the occurrence of different contribution of the temperature-driven and water-driven effects to the whole recovery process. Indeed, for PVA05 without plasticizer the recovery temperature is much lower (approximately of 30 °C) than its T_g, thus the recovery is driven only by the effect of the immersion in water and it is governed by the kinetics of

water absorption. On the other hand, the plasticized formulations have a T_g very close to the recovery temperature and this results in a recovery process activated by the synergistic action of water and temperature, which reasonably occurs immediately without any induction phase. Furthermore, the water diffusion phenomenon may be faster for the plasticized formulations due to the greater free volume associated with lower T_g.

Concerning the employment of the two different manufacturing methods, the biggest difference was found for the rate of the recovery for PVA05. Actually, the rate of the recovery was much higher for the specimen obtained by FDM with respect to the one manufacture by HME leading to $t_{RIfinal}$ values of 180 min and 251 min, respectively. Such a difference may be due to the different surface porosity and roughness characterizing samples obtained by HME and FDM, leading to an effective surface/volume ratio higher for printed samples than extruded ones. Printed specimens have a layered porous structure compared to extruded items, which may be considered as a continuous matrix and this influenced the water absorption kinetics.

Finally, both I-shaped bars and U-shaped bars obtained by the same formulation and the same manufacturing method displayed a similar recovery kinetics, as shown in the curves of Figure 3.11b.

Recovery studies were also performed at body temperature (37 °C), to demonstrate the efficacy of the shape-shifting motions also in conditions closer to the final application, *i.e. in vivo* in the bladder at the body temperature. I-shaped specimens obtained by both HME and FDM were used and the results are reported in Table 3.4. At T_{body} the unplasticized formulations are still below their T_g, whereas the plasticized ones are exactly in the middle of their glass transition. As a consequence, PVA05GLY specimens displayed a quick recovery process, about 75 % faster for tests carried out at T_{body} than at T_{room}. Furthermore, the molecular weight was found to affect the time needed for recovery in a more pronounced manner, as it can be noted by the $t_{RIfinal}$ value of the extruded PVA18GLY which was found to be only about 40 % faster at T_{body} than at T_{room}. A reduction of $t_{RIfinal}$ was observed also for the extruded PVA05 tested at 37 °C as compared with room temperature, and in general for all the formulations, with an extent consistent with that of T_g values, as could be expected based on the increased mobility of the amorphous PVA domains. In the case of the printed PVA05 specimen, it was not possible to determine RI_{final} because of dissolution-driven distortions of the specimen that

was ascribed to the high extent of hydration reached, close to the dissolution threshold, resulting in reduced gel viscosity and sample stiffness.

Based on these findings, it was considered important to evaluate also the fluid uptake and the mass loss properties of the samples during water-induced shape memory experiments, carried out at 37 ± 0.5 °C in simulated urine fluid, to mimic *in vivo* conditions. These properties would in fact affect not only the shape recovery but also the release of the conveyed drug, which is known to be related to the mode of hydration and erosion/dissolution of the polymer.

Figure 3.12 shows the fluid uptake and residual dry mass curves over time, as evaluated by Equation 4 and Equation 5, for extruded specimens and printed ones in Figure 12a and 12b, respectively.

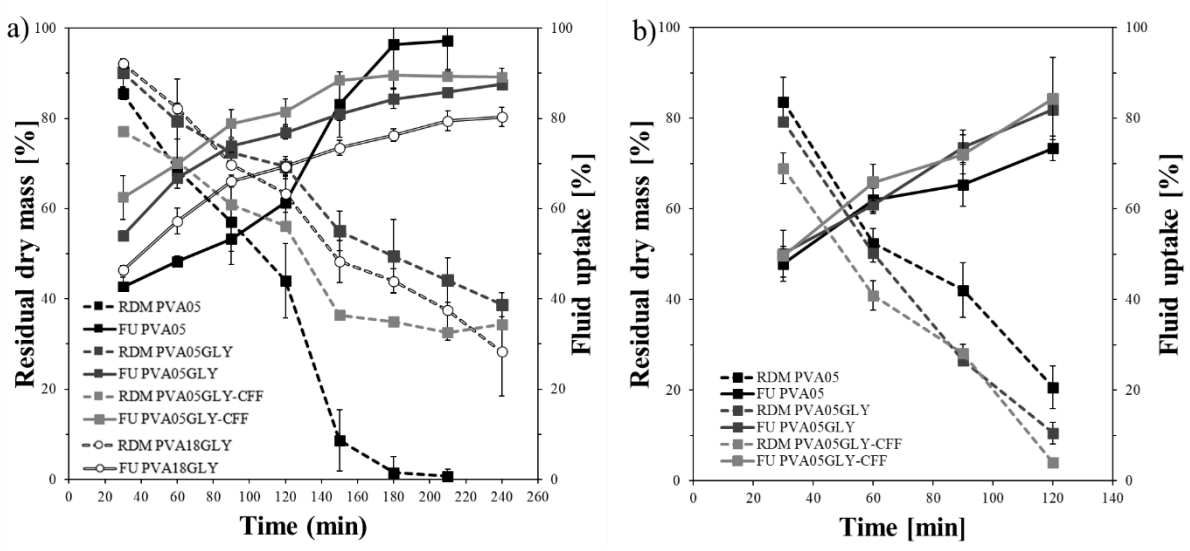

Figure 3.12. Average fluid uptake (FU, solid lines) and residual dry mass (RDM, dashed lines) curves for specimens with permanent I shape during recovery, manufacture by a) HME and b) FDM.

It is possible to observe that a significant percentage of fluid uptake is reached within the first 15 min of testing, in the order of 40% regardless of the manufacturing technique employed, whereas in the same timeframe the value of the residual dry mass remains at high percentages close to 80%. For extruded specimens, it is possible to observe variability in the fluid uptake curves depending on the formulation; specifically, plasticized specimens displayed higher values of fluid uptakes with respect to the unplasticized formulation and this is ascribed to the presence of glycerol, which is supposed to promote fluid absorption due to its hydrophilic nature. Furthermore, also a dependency on the grade of the polymer was found, with the higher molecular

weight polymer (PVA18GLY) showing a lower fluid uptake curve, when compared to PVA05GLY, as expected. Interestingly, the fluid uptake behavior of the specimens was consistent with the shape recovery previously discussed. Indeed, the activation of shape-shifting phenomena in the plasticized formulations was especially rapid not only because of the decreased T_g but also because of the higher amount of fluid taken up in the first minutes of testing.

On the basis of all the thermal, thermo-mechanical and shape memory characterizations, the most promising material systems for the intended retentive intravesical application can be considered the plasticized formulations, since they displayed fast recovery kinetics compatible with physiological conditions. Therefore, in order to evaluate also the capability of a proof-of-concept device to slowly release an active ingredient while undergoing shape recovery, a plasticized formulation was chosen and modified by the addition of caffeine (CFF) as an analytical tracer. Moreover, the selection of the formulation to be used was also guided by the manufacturing constraints for which PVA18GLY revealed to not be processable by FDM with the available equipment. Thus, the additional shape memory characterization was performed for the PVA05GLY-CFF formulation, on specimens with I shape and helix shape, obtained by HME and FDM and tested at T_{room} and at T_{body} in simulated urine fluid. The recovery kinetics was found to be similar irrespective of the testing temperature, as it can be observed when comparing the $t_{RIfinal}$ values listed in Table 3.5 related to testing at T_{room} to the pictures of the recovery performed at T_{body} shown in Figure 3.13 and in general, the recovery was found to be faster than the one found for the other plasticized formulations at T_{room} (Table 4).

	Permanent shape	**RI_{final}**	**$t_{RIfinal}$ [min]**
HME	**I shape**	0.94	40
	Helix shape	0.75	26
FDM	**I shape**	0.76	12
	Helix shape	0.71	12

Table 3.5. RI_{final} values and relevant $t_{RIfinal}$ for PVA05GLY-CFF-based specimens having a permanent I and helix shapes, evaluated by water-triggered recovery tests at $T_{room.}$

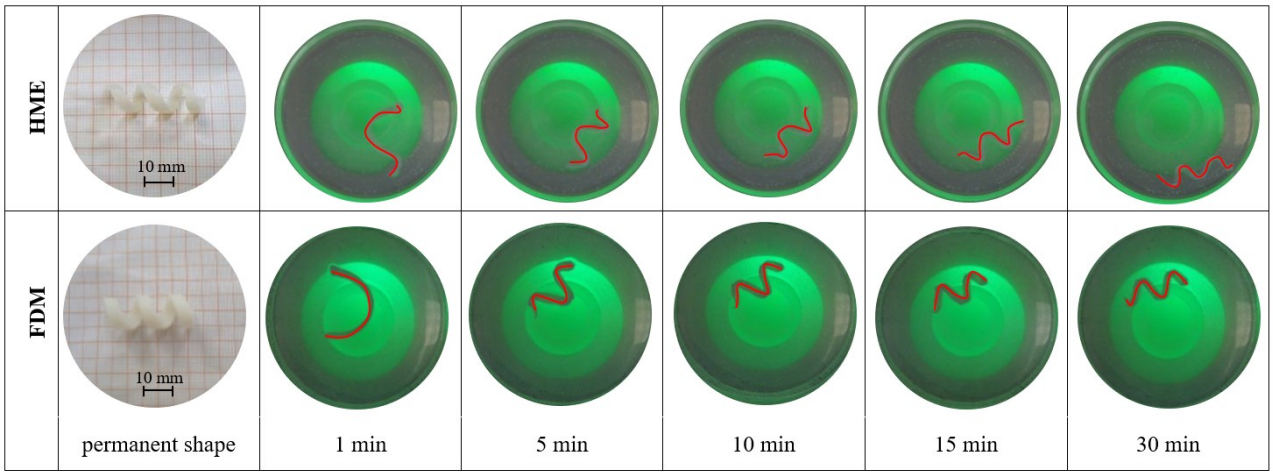

Figure 3.13. Pictures taken during shape recovery experiments carried out at T_{body} (37 °C) for PVA05GLY-CFF specimens with permanent helix shape, obtained by HME (top row) and FDM (bottom row), programmed to take on a temporary I shape. A red solid line is superimposed to highlight the shape changes during the recovery.

This response is consistent with the T_g value for PVA0515GLY-CFF, approximately close to 0 °C as shown in Table 3.2, which is the lower value found for all the formulations and more importantly, it is always lower than the testing temperature, both T_{room} and T_{body}, This consideration reveals that the shape recovery for this case is always driven by the action of temperature as the leading external stimulus in the first stage, helped in the following part thanks to the synergistic action exerted by the water absorption. Furthermore, it's worthy to be noticed that $t_{RIfinal}$ was found to be about two times higher for the extruded specimens as compared to the printed ones, in spite of a comparable extent of recovery RI_{final}. This finding may be explained on account of the porosity and of the layered structure of specimens obtained by the FDM additive manufacturing technique, with a similar argument to the one reported when comparing PVA05 specimens obtained by HME and FDM, as shown in Table 3.4.

Finally, as a first proof-of-concept of the simultaneous , a specific test was set up inside a dissolution apparatus. Extruded and printed samples with a permanent I shape were programmed and deformed into the U shape; afterwards, they were immersed in the dissolution apparatus, filled with simulated urine fluid at 37 °C while taking pictures of the recovery process and evaluating the release of the tracer molecule at given time points. The release profile for caffeine over time is shown in Figure 3.14a, while pictures of a printed specimen inside this testing configuration are shown in Figure 3.14b by way of example.

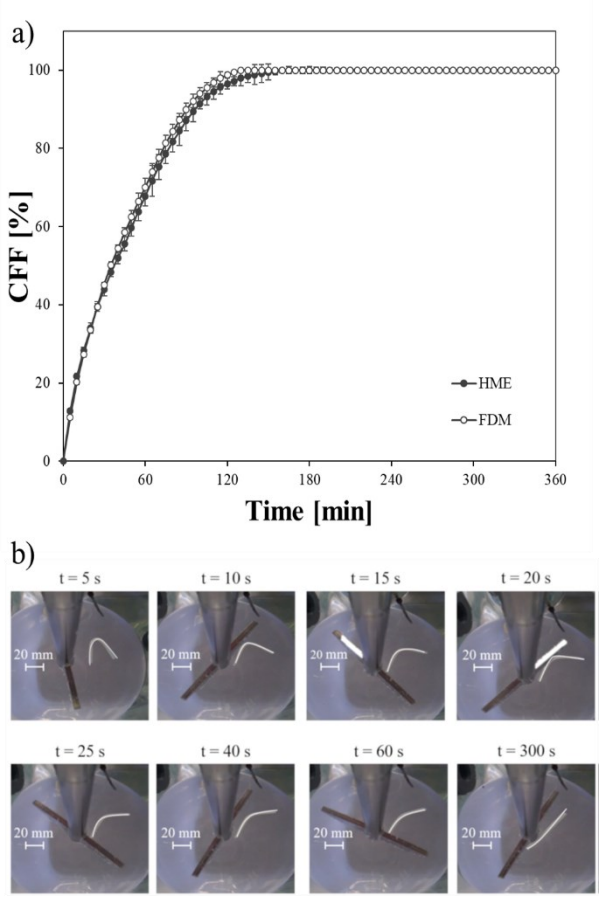

Figure 3.14. Evaluation of caffeine-containing specimens (PVA05GLY-CFF). In a) release profiles of specimens with permanent I shape obtained by HME (full grey markers) and FDM (full white markers) measured during shape recovery; in b) pictures of the FDM specimen in the dissolution apparatus taken at subsequent time points until full recovery.

Interestingly, release curves of specimens obtained by HME and FDM were almost superimposed, resulting in independence of the mode of release from the manufacturing technique, as opposed to the differences found for recovery performances and fluid uptake profiles, there ascribed to the porosity and layered structure obtained through FDM. The release started without any lag phase and was completed within 2 h. Notably, with both extruded and printed specimens, the original straight shape was almost fully recovered in the first minutes of testing. This overall behavior is desired in light of the final application. In fact, the device in its temporary shape loaded with the drug of interest is envisioned to be administered through a catheter and would need to recover its permanent, bladder-retentive shape as quick as possible, in order to safely be retained inside the bladder while slowly starting to release the active ingredient. Clearly, the proof-of-concept system here presented respected these requirement. Future further improvements will regard the choice of drug molecules

of interest and the optimization of the release profile, specifically in order to prolong the release over a wider timeframe to reduce the need of frequent drug administration. These further aims will be pursued by working with different polymeric grades having higher molecular weights or employing specific technological strategies involving sustained-release coatings, commonly used in the pharmaceutical technology research and industry.

3.6 References

1. M.J. Cima, H. Lee, K. Daniel, L.M. Tanenbauma, A. Mantzavinou, K.C. Spencer, Q. Ong, J.C. Sy, J. Santini Jr., C.M. Schoelhammer, D. Blankschtein, R.S. Langer, *J. Control. Release* 2014, 190, 157-171.
2. S.H. Lee, Y.B. Choy, *Int. Neurourol. J.* 2016, 20, 101-106.
3. M.M. Zacchè, S. Srilkrishna, L. Cardozo, *Res. Rep. Urol.* 2015, 7, 169-178.
4. P. Tyagi, M. Kashyap, H. Hensley, N. Yoshimura, *Expert Opin. Drug Deliv.* 2016, 13, 71-84.
5. S. GuhaSarkar, R. Banerjee, *J. Control. Release* 2010, 148, 147-159.
6. J. Nirmal, Y.-C. Chuang, P. Tyagi, M.B. Chancellor, *Urol. Sci.* 2010, 23, 70-77.
7. M.O. Fraser, J.P. Lavelle, M.S. Sacks, M.B. Chancellor, *Rev. Urol.* 2002, 4, 1-11.
8. S. Yamada, Y. Ito, S. Nishijima, K. Kadekawa, K. Sugaya, *Pharmacol. Ther.* 2018, 189, 130-148.
9. H.Y. Yoon, H.M. Yang, C.H. Kim, Y.T. Goo, M.J. Kang, S. Lee, Y.W. Choi, *Expert Opin. Drug Deliv.* 2020, 17, 1555-1572.
10. O.M. Kolawole, W.M. Lau, H. Mostafid, V.V. Khutoryanskiy, *Int. J. Pharm.* 2017, 532, 105-117.
11. J. Barthelmes, G. Perera, J. Hombach, S. Dünnhaupt, A. Bernkop-Schnürch, *Int. J. Pharm.* 2011, 416, 339-345.
12. T. Lin, J. Wu, X. Zhao, H. Lian, A. Yuan, X. Tang, S. Zhao, H. Guo, Y. Hu, *J. Pharm. Sci.* 2014, 103, 927-936.
13. D.G. Matsuura, W.D. Gillespie, J.P. Greelis, C.L. Parsons, M. Sirivong, P.F. Zupkas, US6171298B1
14. H. Lee, M.J. Cima, *J. Control. Release* 2011, 149, 133-139.
15. J.C. Nickel, P. Jain, N. Shore, J. Anderson, D. Giesing, H. Lee, G. Kim, K. Daniel, S. White, C. Larrivee-Elkins, J. Lekstrom-Himes, M. Cima, *Sci. Transl. Med.* 2012, 4, 1-11.
16. S. Daneshmand, K.S. Pohar, G.D. Steinberg, M. Aron, C. Cutie, *J. Clin. Oncol.* 2017, 35, [abstract] e16000.
17. W.S. Tan, J.D. Kelly, *Nat. Rev. Urol.* 2018, 15, 667-685.
18. M. Behl, A. Lendlein, *Mater. Today* 2007, 10, 20-28
19. T. Liu, T. Zhou, Y. Yao, F. Zhang, L. Liu, Y. Liu, J. Leng, *Compos. Part A-Appl. S.* 2017, 100, 20-30.
20. H. Meng, G. Li, *Polymer* 2013, 54, 2199-2221.
21. H. Lu, W.M. Huang, *Smart Mater. Struct.* 2013, 22, 115019.
22. H. Lu, *J. Appl. Polym. Sci.* 2013, 127, 2896-2904.

23. H. Lu, Y. Liu, J. Leng, S. Du, *Eur. Polym. J.* 2010, 46, 1908-1914.
24. B. Yang, W.M. Huang, C. Li, C.M. Lee, L. Li, *Smart Mater. Struct.* 2004, 13, 191-195.
25. B. Yang, W.M. Huang, C. Li, L. Li, *Polymer* 2006, 47, 1348-1356.
26. H. Du, J. Zhang, *Soft Matter* 2010, 6, 3370-3376.
27. X. Qi, X. Yao, S. Deng, T. Zhou, Q. Fu, *J. Mater. Chem. A* 2014, 2, 2240-2249.
28. H. Chen, Y. Li, G. Tao, L. Wang, S. Zhou, *Polym. Chem.* 2016, 7, 6637-6644.
29. Z. Fang, Y. Kuang, P. Zhou, S. Ming, P. Zhu, Y. Liu, H. Ning, G. Chen, *ACS Appl. Mater. Interfaces* 2017, 9, 5495-5502.
30. S. Paonessa, N. Barbani, E. Cibrario Rocchietti, C. Giachino, C. Cristallini, *Mat. Sci. Eng. C-Mater* 2017, 75, 1427-1434.
31. A. Melocchi, F. Parietti, A. Maroni, A. Foppoli, A. Gazzaniga, L. Zema, *Int. J. Pharm.* 2016, 509, 255-263.
32. A.Y. Sherif, G.M. Mahrou, F.K. Alanazi, *Saudi Pharm. J.* 2018, 26, 845-851.
33. J. Jang, D.K. Lee, *Polymer* 2003, 44, 8139-8146.
34. C.-A. Lin, T.-H. Ku, *J. Mater. Process Technol.* 2008, 200, 331-338.
35. M. Mohsin, A. Hossin, Y. Haik, *J. Appl. Polym. Sci.* 2011, 122, 3102-3109.
36. S.K. Burgess, J.S. Lee, C.R. Mubarak, R.M. Kriegel, W.J. Koros, *Polymer* 2015, 65, 34-44.

Chapter 4

Design and development of a gastroretentive drug delivery device based on shape memory polymers

The work here reported has been already partially published in:

A.Melocchi, M. Uboldi, **N. Inverardi**, F. Briatico-Vangosa, F. Baldi, S. Pandini, G. Scalet, F. Auricchio, M. Cerea, A. Foppoli, A. Maroni, L. Zema, A. Gazzaniga, Expandable drug delivery system for gastric retention based on shape memory polymers: Development *via* 4D printing and extrusion, *Int. J. Pharm.* 2019, 571, 118700.

And submitted for publication in:

N. Inverardi, G. Scalet, A. Melocchi, M. Uboldi, A. Maroni, L. Zema, A. Gazzaniga, F. Auricchio, F. Briatico-Vangosa, F. Baldi, S. Pandini, Experimental and computational analysis of a pharmaceutical-grade shape memory polymer applied to the development of gastroretentive drug delivery systems.

4.1 Introduction

The development of controlled release dosage forms for the gastrointestinal (GI) tract has long been investigated in the pharmaceutical field on the basis of the expected benefits from a pharmacokinetics and pharmacodynamic point of view[1]. In fact, several advantages might be associated to the employment of gastroretentive systems, such as an improved oral bioavailability for various types of drugs which suffer from a narrow absorption window at the upper part of the GI tract, for instance in the duodenum and jejunum (*e.g.* metformin, used for the treatment of type II diabetes, and levodopa, used for the treatment of Parkinson[2]. Both the drugs have a narrow absorption window in the upper part of the GI tract together with a short half-life, *i.e.* the time after which the concentration of the drug in the body is half of the starting dose). The passage through these regions is rapid, hence the extent of absorption at these sites can be limited. Clearly, having a system which is retained in the stomach while releasing the drug in a controlled and prolonged fashion may be useful to the aim of continuously supply the active ingredient to its absorption site[1,3]. Furthermore, it could be advantageous also for those drugs which have lower solubility in the intestinal environment than in the stomach or that are more stable in the acidic environment of the stomach (*e.g.* ofloxacin[3], used for the treatment of bacterial genitourinary and respiratory infections and captopril[4], used for the treatment of hypertension and congestive heart failure, is stable at pH 1.2). Another advantage may regard the possibility for local treatment as in the case of gastric or duodenal ulcers, esophagitis and of the eradication of *Helicobacter pylori*[2,5-8] . In fact, it is known that this bacterium lives within the gastric mucus layer and a prolonged local application of the drug can help to reach the bacterium.

From a pharmacodynamic perspective, a continuous release of the drug leads to a more stable drug concentration in the blood, compared to the immediate release dosage forms, with less fluctuations so that peak concentration with their relevant adverse effects can be avoided[3].

Additionally, another aspect has to be taken into account and it regards the difficulties associated to therapies requiring multiple drugs administration with high dosing frequency, often resulting in low patient compliance. In fact, as evaluated by the WHO[9], the adherence to long-term therapies is low, about 50%, especially in some patient populations (*e.g.* children, elderly people and patients with cognitive/mental disorders), and it is even much lower in developing countries, where the access to medications and health resources can often be limited. Therefore, a gastroretentive drug delivery system capable of prolonging drug release over days/weeks/months

can be highly beneficial to reduce dose frequency and, as a consequence, improving patient compliance, hence the outcome of the treatment[5].

The achievement of gastric retention has held great promise but the challenges to overcome were several and slowed down the development of gastroretentive systems, because of the anatomical, mechanical, hydrodynamic and chemical issues involved, such as peristaltic contractions and housekeeper waves, variable fluid volume, propulsive and retropulsive jets of gastric fluid, enzymatic processes, acidic pH.

Various approaches have been proposed over the years, relying on different working mechanisms, such as density modification (devices featuring high-density sedimentation or low-density floatation in the stomach), adhesion to the gastric mucosa, magnetic retention and localization and size increase to physically prevent the passage of the device through the pylorus[1,2,5,8,10-13]. One of the most promising strategies is represented by size-increasing gastroretentive devices, also known as expandable gastroretentive systems, which were initially developed for veterinary applications throughout the 1980s.

Figure 4.1 represents two expandable gastroretentive devices for ruminants which enabled oral administration thanks to a folded shape which is released in the rumen to avoid its evacuation and ensure its retention.

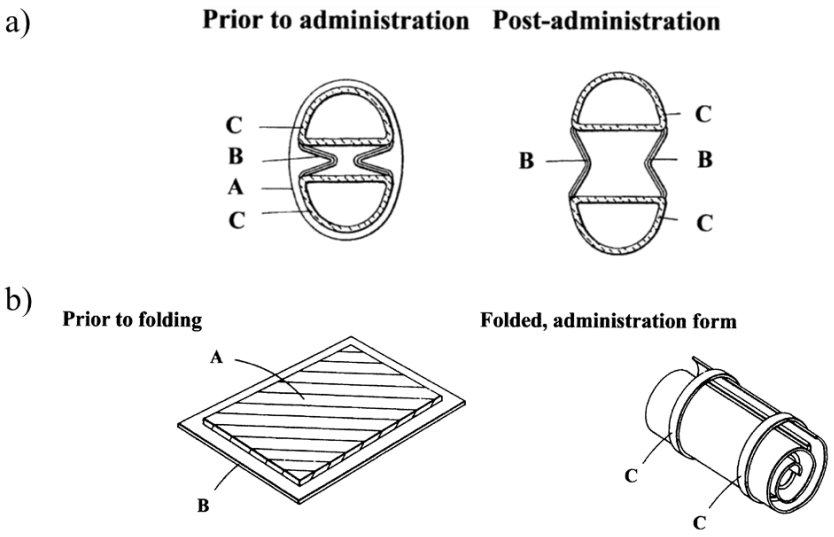

Figure 4.1. Expandable gastroretentive devices for veterinary application. a) Unfolding dosage form with a gelatin capsule (A), hydrophobic/hydrophilic strips (B) which upon water uptake after the capsule dissolution cause the expansion of the device, and a permeable material containing the drug (C)[14]. b) Unfolding dosage form composed of an erodible sheet (A) as a drug reservoir attached to a non-erodible

resilient sheet (B) to prolong retention and gelatin strips (C) to secure the folded configuration for the administration[15].

In order to move from veterinary applications to employment in humans, several devices started to be designed on the base of the various requirements to fulfill including i) a convenient and well-accepted administration mode (such as *via* the oral route), ii) prompt achievement of the bulky configuration enabling retention upon entry in the stomach, iii) retention for a programmed period of time while releasing the drug without interfering with gastric motility, iv) mechanical resistance to counteract muscle contraction, v) elimination following reduction in size. These systems have to be conceived to be deformed into a collapsed configuration which enables easy swallowing, typically within a carrier dosage form (*e.g.* a capsule), for instance by folding. Once in the stomach, they can regain their initial configuration with larger spatial encumbrance, preventing passage through the wide open pylorus that has diameter of about 11 - 13 mm. The first studies were focused on the identification of geometries suitable to accomplish these goals based on unfolding mechanisms. However, in spite of the good *in vivo* results obtained in a dog model with a period of residence of 24 h, the later translation to humans were less satisfactory. Over the years, some systems have received FDA approval or are in phase III clinical trials, such as the Depomed's Acuform® technology which is an expanding pill working upon swelling and achieving retention for 8-10 h, and the Accordion Pill™ (IntecPharma) which consists of a folded film conveyed into a capsule capable to be retained for about 12 h[1,5].

The key challenge remained the achievement of a significant retention time, beyond 24 h. Pioneering research with this respect was recently performed at the Massachusetts Institute of Technology (MIT), with the development of several devices working by unfolding or swelling and led to the foundation of a company (Lyndra® Therapeutics) with several researches under pre-clinical and Phase I clinical study and one under Phase II concerning weekly administration of a drug for the treatment of schizophrenia[16]. In more details, a first gastroretentive drug delivery device was designed in a stellate shape, as shown in Figure 4.2a, composed of multiple materials: an elastomeric core and rigid polymeric arms containing the drug formulation. The device can be folded to fit a standard size gelatin capsule (00el) and upon dissolution of the capsule it deploys reaching sizes compatible with gastric retention up to a period of 14 days in a large animal model (swine)[17,18].

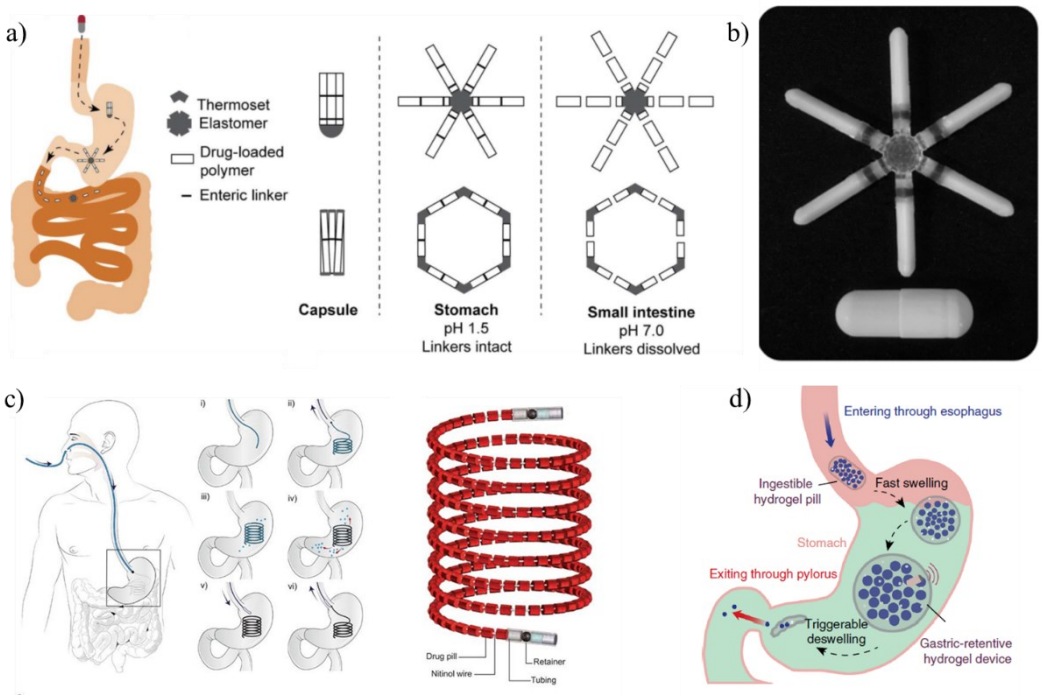

Figure 4.2. Gastroretentive devices designed at the Massachusetts Institute of Technology. a) Star-shaped device working upon unfolding in the stomach[17]. b) Extended release oral capsule (Lyndra® Therapeutics): device to be fitted inside a 00el capsule[21]. c) Gastric resident system for multigram dosing administered and retrieved by the nasogastric route[19]. d) Ingestible hydrogel pill undergoing high speed swelling upon reaching the stomach[20].

These devices have drug loading capabilities <500 mg and this might be an issue when dealing with treatments requiring gram-level dosing of drug, such as in the case of tuberculosis treatment. Therefore, another approach, shown in Figure 4.2c, was developed consisting of a superelastic Nitinol wire equipped with several drug pills to reach and tune the amount of drug loading. The wire is straighten up for the administration through the nasogastric route, but thanks to its superelastic response, upon release of the wire in the stomach it recovers its coil shape for gastric retention releasing the drug over the course of 4 weeks. This macrodevice solves the issue of high drug loading capacity but at the cost of a more invasive way of administration and retrieval. Conversely, in order to pursue an approach that takes into account also the interface of the device with the stomach, soft materials and in particular hydrogels were considered to enhance the mechanical compatibility of the device and its retention site. To this aim, a novel ingestible hydrogel was developed consisting of a poly(vinyl alcohol) hydrogel-skin containing superabsorbent hydrogel particles. These latter ones, as outlined

in Figure 4.2d, quickly imbibe water upon entering into the stomach leading to a fast shape change and swelling up to sizes compatible with gastric retention. This device was shown to reside in vivo in large animal model (swine) up to 1 months while continuously monitoring physiological signals, such as temperature. For all the devices developed, great attention was given to the mechanism of voidance from the stomach. This was ensured by different mechanisms based on the decrease in the size of the device, either brought about by exposure to specific substances administered orally when appropriate, or associated with weakening/breaking of purposely designed portions due to diminished resistance to gastric contractions.

Therefore, given the aforementioned devices and their relevant working mechanism, an approach based on the use of shape memory polymers to provide the required shape expansion was also considered worthy to be investigated in this chapter. In fact, shape memory polymers may offer advantages since they are capable of large shape changes and they feature a stiffness variation across the shape changes which can be helpful for interfacing with soft tissues. Furthermore, they can be designed to be bioerodable/biodegradable in the stomach so as to eliminate the need for a retrieval of the device, which was required when using their metallic counterparts (shape memory alloys) as in the case of the Nitinol-based device previously described.

The work presented in this chapter was carried out in collaboration with Dr. Alice Melocchi, Marco Uboldi, Prof. Lucia Zema, Prof. Alessandra Maroni and Prof. Andrea Gazzaniga from the Biopharmaceutics and Pharmaceutical Technology Laboratory of the University of Milano, with Prof. Francesco Briatico-Vangosa (Politecnico di Milano) and with Dr. Giulia Scalet and Prof. Ferdinando Auricchio of the Computational Mechanics and Advanced Materials group of the University of Pavia.

4.2 Design Concept

The aim of developing a self-expandable gastroretentive drug delivery device was approached in this chapter under a novel perspective by taking into account the inherent shape-shifting capability of shape memory polymers. In fact, the shape memory response might be useful to such an aim, by leveraging the possibility of programming a temporary shape, which can be fitted inside a commercially available capsule and exploiting the recovery of the permanent shape upon contact with the acidic environment of the stomach to achieve a bulky configuration capable to be retained in the organ.

Therefore, the key challenge addressed was related to the design of both the permanent gastroretentive shape and the temporary one which has to be compliant to the available sizes of gelatin capsules. Concerning the permanent shape, gastric retention was assumed to be reached if the spatial encumbrance of the device is large enough to prevent its passage through the pylorus to the intestine. In particular, considering the diameter of the wide open pylorus, ranging between 5.6 and 22.1 mm and more commonly reported as 11-13 mm, the design criterium for the permanent shape resulted in having at least two dimensions bigger than 13 mm. Additionally, the permanent shape should be characterized by large void volumes in order not to prevent passage of gastric fluids through the pyloric sphincter, should the device be positioned in its close proximity during residence in the stomach. Conversely the geometry of the temporary shape was based on the dimensions of standard hard-gelatin capsules, especially considering those ones recommended for preserved patients acceptance and compliance, such as AA size and 00el size[21,22], whose main dimensions are reported in Table 4.1.

Capsule size	Diameter [mm]	Overall closed length [mm]
00el (Coni-Snap®)	8.18 ± 0.06 *	25.3 ± 0.03
AA (DB caps®)	9.39 ± 0.06 #	17.5 ± 0.03

Table 4.1. Dimensions of the chosen capsules relevant to the design of the temporary shapes. *body external diameter, #internal diameter.

Various permanent shapes meeting the required dimensions were conceived to be manufactured by either fused deposition modeling (FDM) or hot-melt extrusion (HME). The permanent shapes, their relevant temporary shapes and the resulting encapsulated devices proposed are reported in Figure 4.3, 4.4, 4.5 and 4.6.

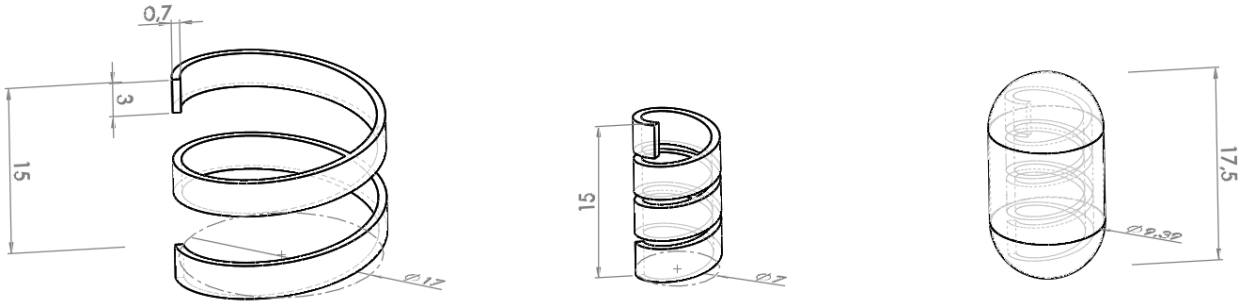

Figure 4.3. From left to right Permanent shape: cylindrical helix with rectangular cross-section; temporary shape: supercoiled helix; encapsulated device in a DB caps® AA sized capsule.

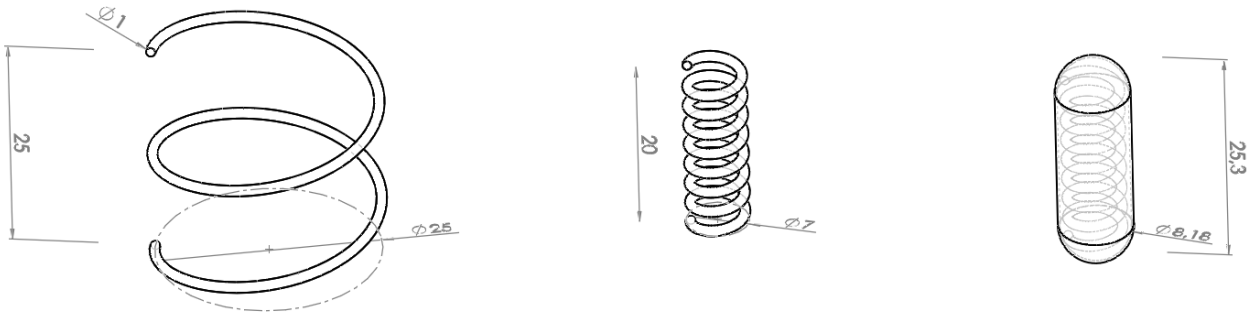

Figure 4.4. From left to right Permanent shape: cylindrical helix with circular cross-section; temporary shape: supercoiled helix; encapsulated device in a Coni-Snap® 00el capsule.

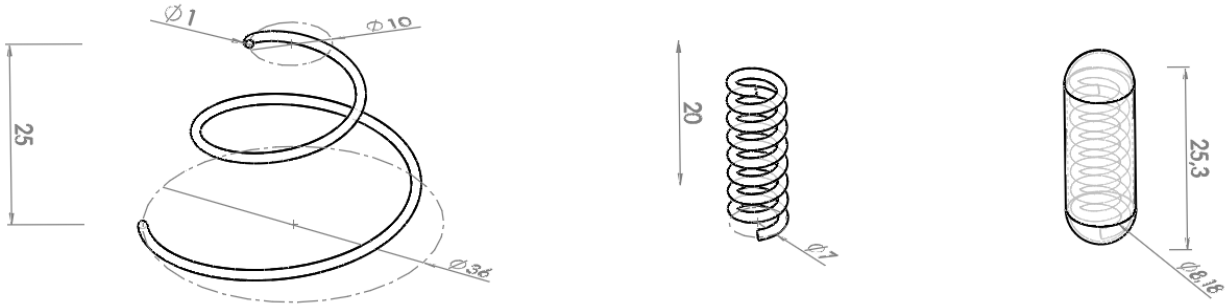

Figure 4.5. From left to right Permanent shape: conical helix with circular cross-section; temporary shape: supercoiled helix; encapsulated device in a Coni-Snap® 00el capsule.

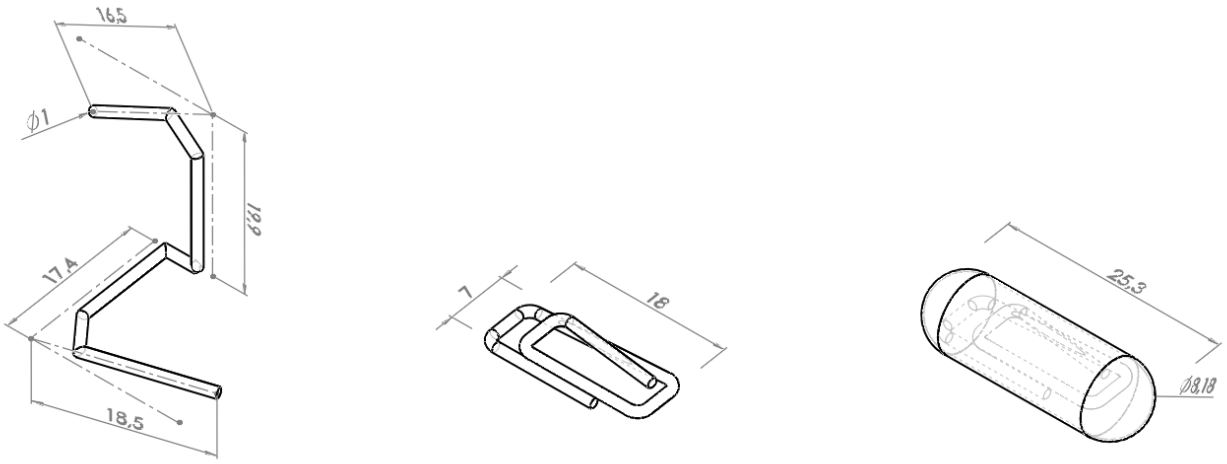

Figure 4.6. From left to right Permanent shape: S-shaped clip with circular cross-section; temporary shape: paper-clip; encapsulated device in a Coni-Snap® 00el capsule.

The investigations performed in this chapter have the final aim of demonstrating the achievement of the designed shape changes, as sketched in Figure 4.7 for the case of the permanent conical shape, by way of example, which might be useful for the development of gastroretentive drug delivery devices.

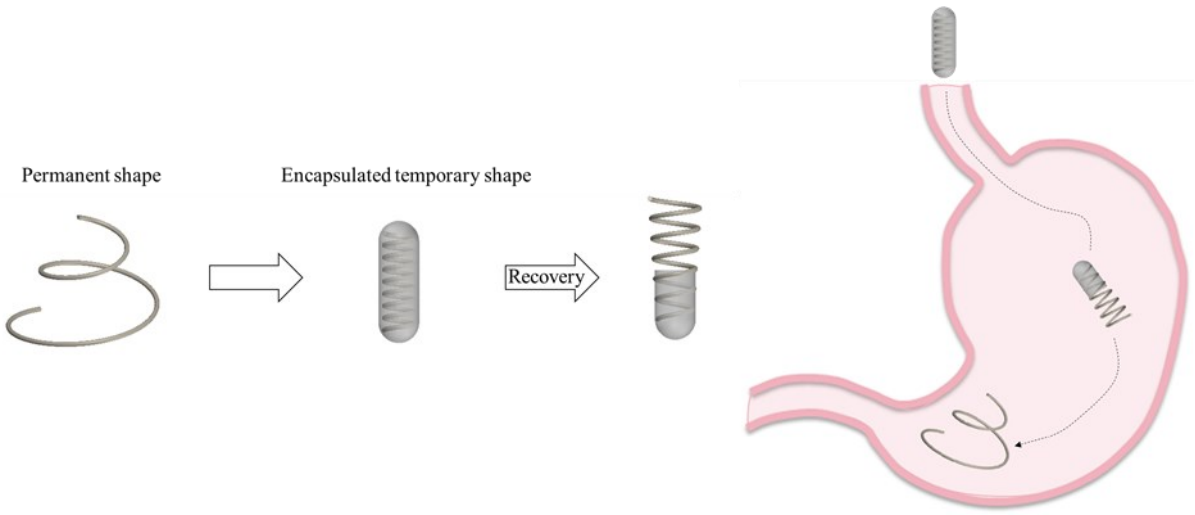

Figure 4.7. Targeted shape-shifting sequence for a gastroretentive prototype based on a conical helix as permanent shape. From left to right: permanent shape (conical helix of Figure 5); encapsulated temporary shape in a 00el capsule; supposed shape at a given point during the recovery and capsule dissolution; desired shape changes upon swallowing of the capsule.

4.3 Materials

The materials used comprised two pharmaceutical grades of poly(vinyl alcohol) already introduced in the Chapter 2, *i.e.* Gohsenol™ EG 05P and Gohsenol™ EG 18P (Nippon Gohsei), thereafter called PVA05 and PVA18, respectively. Glycerol (Pharmagel), labeled as GLY, was used as plasticizer and Allopurinol (FarmaQuimica sur S.L.; boiling point 250.36 °C, melting point > 300 °C[23]), labeled as ALP, was employed as a model drug molecule. Metacrylic acid copolymer Eudragit® RS100 (Evonik) and triethyl citrate (Sigma Aldrich) were used for a coating treatment. Carbonium Nylon filaments with a diameter of 1.75 mm were purchased from TreeDFilaments and used as received for 3D printing of templates. Hard-gelatin Coni-snap® capsule size 00el (capacity 1.02 mL, body external diameter 8.18 ± 0.06 mm, overall closed length 25.3 ± 0.03 mm) and DB caps® size AA (capacity 0.80 mL, internal diameter 9.39 ± 0.06 mm, overall closed length 17.5 ± 0.03 mm) (Capsugel, I) were used to encapsulate the gastroretentive device.

Plasticized PVA-based formulations were kindly manufactured by the group of Biopharmaceutics and Pharmaceutical Technology at the University of Milano with hot-melt extrusion (HME) and fused deposition modeling (FDM) 3D printing techniques, as briefly reported in the following.

PVA05GLY and PVA18GLY were prepared starting by PVA05 and PVA18 powders, previously dried in an oven at 40 °C for 24 h, and adding 15% by weight of GLY calculated on the dry polymer. The mixtures were further dried at 40 °C for 8 h, ground by a blade mill and the < 250 μm powder fraction was used. Drug-containing formulations, labeled PVA05GLY-ALP and PVA18GLY-ALP, were prepared by adding ALP powder, previously dried at 40 °C for 24 h, to PVA05GLY and PVA18GLY respectively in a 1:9 weight ratio.

PVA05GLY and PVA05GLY-ALP formulations were processed by FDM using a Kloner3D 240® Twin (Kloner3D) printer equipped with 0.5 mm nozzle. Suitable filaments to use in the 3D printer were obtained by extrusion through a custom-made aluminum circular die with a diameter equal to 1.80 mm, as reported elsewhere[24]. The design of the cylindrical helix with rectangular cross section, shown in the Design Concept section in Figure 4.3, to be printed as the permanent shape was drawn in Autodesk® Autocad® 2016 (Autodesk Inc), saved in .stl format and imported to the printer software (Simplify 3D). 25cm-long portions of the in-house prepared filaments were fed to the printer and the printing was performed with the printing temperature

equal to 190 °C, the infill equal to 100%, the layer height equal to 0.10 mm, the printing speed equal to 23 mm/s and the separation gap for raft and supports equal to 0.5 mm.

PVA18GLY and PVA18GLY-ALP formulations were processed by HME with a twin-screw extruder (Haake™ MiniLab II, Thermo Scientific) equipped with counter-rotating screws and with a custom-made aluminum die (circular cross section with a diameter equal to 1.00 mm), according to the process conditions reported in Table 4.2.

System	T [°C]	Screw speed [rpm]	Torque [Ncm]
PVA18GLY	200	20	190
PVA18GLY-ALP	200	20	210

Table 4.2. Process conditions and maximum torque values recorded during HME.

The rods coming out from the extruder, while still hot, were wrapped around 3D printed templates and cooled down under pressurized air for 2 min to obtain the cylindrical helix, the conical helix and the S-shapes clip presented in the Design Concept section in Figure 4.4, 4.5 and 4.6 as permanent shapes. 3D printed templates were manufactured using commercial carbonium Nylon filaments on a Kloner3D 240® Twin (Kloner3D) printer, by setting the printing temperature to 230 °C, the infill to 100 %, the layer height to 0.10 mm and the printing speed to 50 mm/s. CAD models of the templates, shown in Figure 4.8 along with their corresponding permanent shape obtained, were drawn in Autodesk® Autocad® 2016 (Autodesk Inc). Additional templates, similarly designed and processed, were obtained by 3D printing and used to set the temporary shapes of the prototypes, as later described in the Result section.

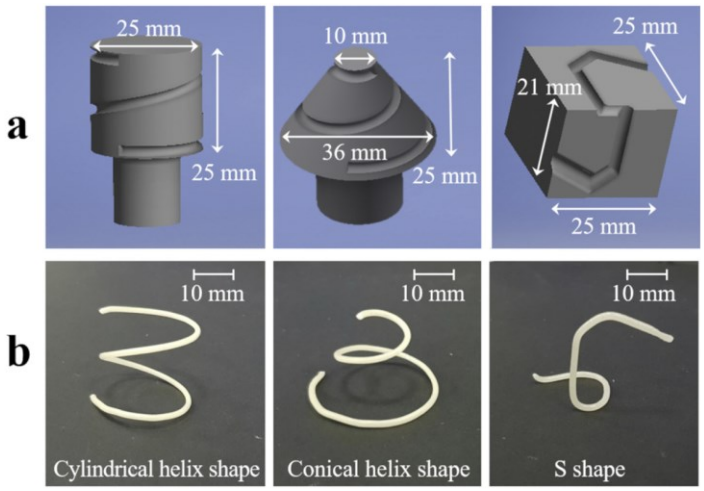

Figure 4.8. a) CAD 3D drawings of the templates used to obtained the permanent shapes by HME; b) pictures of the permanent shapes obtained by HME.

A group of samples with cylindrical helix shape was subjected to a coating treatment performed at ambient conditions with a spraying system (nozzle diameter = 0.8 mm, pump speed = 10 rpm, atomizer = 0.75 atm, pattern = 1 atm) and a rotating gear (2.3 rpm). A 14% w/w ethanolic solution of Eudragit® RS/Eudragit® RL (1/1 w/w) plasticized with 15% w/w of triethyl citrate on the dry polymer was used up to a 60% of weight gain of the samples. Samples after coating were cured at 40 °C for 2 h in a ventilated oven.

All the samples were stored in heat-sealed alufoil moisture barrier bags.

4.4 Methods

The employed methodologies included a first demonstration of the design feasibility for the proposed approach regarding proof-of-concept gastroretentive devices and a more in-depth investigation of the materials properties ensuring the shape memory effect.

The first part of the experimental methodologies concerned the investigation of the shape changes of the prototypes and consisted of differential scanning calorimetry (DSC) analyses to assess the glass transition temperature T_g, shape recovery tests to evaluate the shape memory performances and release tests to obtain the release profile of drug-containing prototypes.

Differential scanning calorimetry

DSC analyses were carried out by means of a DSC Q100 (TA Instruments) employing nitrogen as a purge gas and setting the thermal program to perform three scans at 10 °C/min on samples of about 10 mg: a first heating from -50 °C to 240 °C, a cooling down to -50 °C and a second heating up to 240 °C.

Shape memory characterization on the prototypes

Prototypes obtained by HME and FDM underwent a shape memory characterization comprising the programming of the temporary shape and the recovery of the permanent one. The programming consisted of heating the prototypes up to a deformation temperature $T_{def} = T_g + 35$ °C (evaluating T_g from the DSC analyses); the prototypes were then deformed either manually or by using purposely developed templates (shown in the Results section in Figure 4.13b) and the temporary shapes achieved were set by cooling under the imposed deformation well below T_g, down to -20 °C, keeping these conditions for at least 1 h before the recovery tests.

Recovery tests consisted of immersion of the temporary shapes into a crystallization vessel filled with 250 mL of simulated gastric fluid, prepared with HCl 0.1N. A testing environment with unstirred fluid kept at 37 ± 0.5 °C was reached by keeping the vessel inside a thermoregulated bath. Pictures were taken throughout the all recovery by using two digital cameras (GoPro Hero Session) placed above and in front of the specimens (distances of 13 cm and of 10 cm, respectively). Tests were done on three

replicates. The pictures were processed with a software (ImageJ) to evaluate the evolution of specific geometric parameters during the recovery in order to build recovery index (RI) curves over time. Recovery indexes were defined with respect to the permanent shape of the samples according to the following Equations.

For samples having a permanent cylindrical helix shape, RI values were measured on the coil diameter θ, shown in Figure 4.9a, as defined with $RI_{\emptyset,CylindricalHelix}$ in Equation 1

$$RI_{\emptyset,CylindricalHelix}(\%) = \frac{\emptyset_t - \emptyset_p}{\emptyset_0 - \emptyset_p} \times 100 \quad (1)$$

where $RI_{\emptyset,CylindricalHelix}$ is the coil diameter recovery index, with $\emptyset_t$ the diameter measured during shape recovery, $\emptyset_p$ the one measured in the temporary shape, $\emptyset_0$ the one measured in the permanent shape.

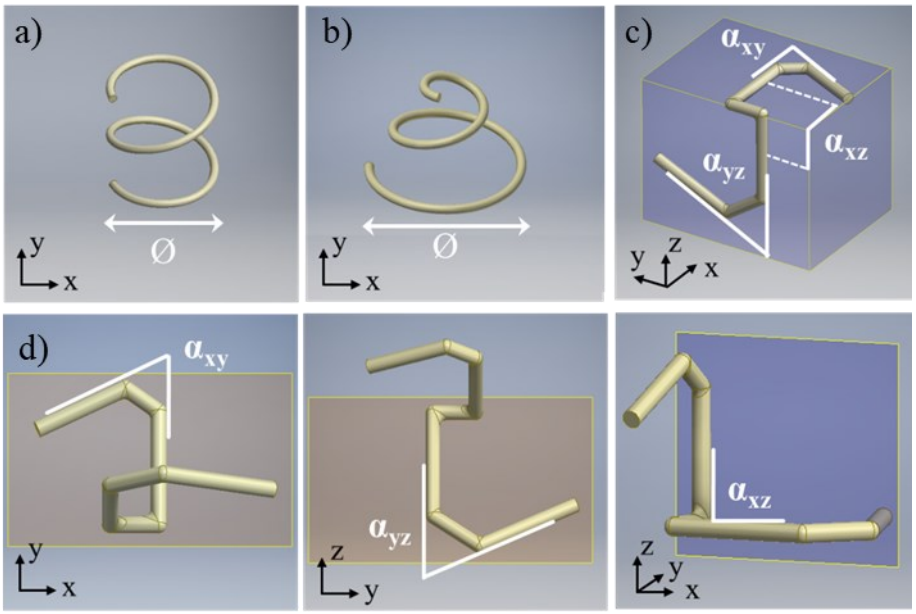

Figure 4.9. Definition of the geometrical parameters used to define the recovery index RI on the CAD drawings relevant to a permanent shape of a) cylindrical helix, b) conical helix, c) S-shaped clip. In d) representation of the S-shaped clip in the xy, yz and xz plane, from left to right.

For samples having a permanent conical helix shape, RI values were measured on the coil diameter at the largest section θ shown in Figure 4.9b, as defined with $RI_{\emptyset,ConicalHelix}$ in Equation 2

$$RI_{\emptyset,ConicalHelix}(\%) = \frac{\emptyset_t - \emptyset_p}{\emptyset_0 - \emptyset_p} \times 100 \quad (2)$$

where $RI_{\emptyset,ConicalHelix}$ is the coil diameter recovery index -measured at the largest section -, with $\emptyset_t$ the diameter measured during shape recovery, $\emptyset_p$ the one measured in the temporary shape, $\emptyset_0$ the one measured in the permanent shape.

For samples having a permanent S-shaped clip, RI values were measured on the three angles α_{xy}, α_{yz} and α_{xz} represented in Figure 4.9c by defining Equation 3, 4 and 5

$$RI_{\alpha_{xy}}(\%) = \frac{\alpha_{xy,t} - \alpha_{xy,p}}{\alpha_{xy,0} - \alpha_{xy,p}} \times 100 \quad (3)$$

$$RI_{\alpha_{yz}}(\%) = \frac{\alpha_{yz,t} - \alpha_{yz,p}}{\alpha_{yz,0} - \alpha_{yz,p}} \times 100 \quad (4)$$

$$RI_{\alpha_{xz}}(\%) = \frac{\alpha_{xz,t} - \alpha_{xz,p}}{\alpha_{xz,0} - \alpha_{xz,p}} \times 100 \quad (5)$$

where $RI_{\alpha_{xy}}$ is the recovery index for the angle α_{xy}, with $\alpha_{xy,t}$ the angle measured during shape recovery, $\alpha_{xy,p}$ the one measured in the temporary shape and $\alpha_{xy,0}$ the one measured in the permanent shape; $RI_{\alpha_{yz}}$ is the recovery index for the angle α_{yz}, with $\alpha_{yz,t}$ the angle measured during shape recovery, $\alpha_{yz,p}$ the one measured in the temporary shape and $\alpha_{yz,0}$ the one measured in the permanent shape; $RI_{\alpha_{xz}}$ is the recovery index for the angle α_{xz}, with $\alpha_{xz,t}$ the angle measured during shape recovery, $\alpha_{xz,p}$ the one measured in the temporary shape and $\alpha_{xz,0}$ the one measured in the permanent shape. During the recovery of the S-shaped clip, only two angles can be measured in a single recovery test because the sample can lie on two different planes in the crystallization vessel, given its geometry. Therefore, one recovery test for this geometry consisted of two replicates on two different samples to acquire all the three angles defined.

Additional recovery tests were performed to visually follow the shape changes of the prototypes after encapsulating the temporary shapes in commercially available gelatin capsules and promoting the recovery by immersion of the encapsulated prototypes into simulated gastric fluid at 37 ± 0.5 °C. The

capsules were glued to a microscope slide placed in the crystallization vessel to avoid floating and to ease the recording of pictures throughout all the recovery process.

Evaluation of release performance

The release profile of ALP-containing samples was assessed by using a USP38 dissolution apparatus 2 (Distek) working at 50 rpm, at 37 ± 0.5 °C, filled with 900 mL of HCl 0.1N. Both samples in their permanent shape as obtained after fabrication and placed in capsules in their temporary shapes were used. Fluid samples were withdrawn at specific time points and assayed spectrophotometrically (λ = 251 nm) and the release profile curve was built. The test was done on six samples for each material system. Pictures were taken every 5 s with a camera (GoPro Hero Session) during the whole length of the test.

The second set of tests was carried out in order to thoroughly investigate the shape memory response of the material with thermal, mechanical and shape memory characterization under different testing conditions and on different samples geometries. Furthermore specific testing was conducted also in order to generate the necessary data for the calibration and validation of a constitutive model, implemented with computational investigation, to finally simulate the shape changes of one of the prototype. All the testing was carried out for the extruded PVA18GLY, as a model material, but the methodologies employed can be easily applied to the other material systems previously presented. According to the specific test, extrudates with a rectangular cross section (5 x 2 mm^2) or a circular cross section (diameter equal to 1 mm) were used as obtained by the twin-screw extruder equipped with relevant dies, under the same process conditions, as reported in Table 4.2.

Thermal, thermo-mechanical and mechanical analyses

DSC analyses were performed on a DSC Q100 (TA Instruments) on samples of about 10 mg, using nitrogen as purge gas. The thermal scans, all run at 10 °C/min, consisted of a first heating from -50 °C to 240 °C, a cooling down to 50 °C and a second heating from -50 °C to 240 °C.

Dynamic mechanical thermal analyses (DMTA) were performed by means of a DMA Q800 (TA Instruments) equipped with a tensile clamp on bars cut from the extrudates (gauge length: 10-15 mm) under single frequency or multi-frequency approaches. The former test consisted in applying 10 μm in amplitude of an oscillating displacement at 1 Hz, while heating from -50 °C to 200 °C at 3 °C/min. The latter test consisted in applying a displacement amplitude of 15 μm, while scanning a region from -50 °C to 160 °C at a heating rate of 0.5 °C/min with a sweep at a set of frequencies (100 Hz, 60 Hz, 40 Hz, 30 Hz, 20 Hz, 10 Hz, 6 Hz, 4 Hz, 3 Hz, 2 Hz, 1 Hz, 0.6 Hz, 0.4 Hz). In both cases a pre-load force (0.01 N) was applied.

Mechanical tests were performed under quasi-static conditions in tensile and compressive conditions at 60 °C, *i.e.* T_g + 35 °C. Tensile tests were carried out by means of the dynamic mechanical analyzer (DMA Q800) on samples cut from the extruded bars (gauge length: 10 mm) with a ramp force of 1 N/min up to the maximum load allowed (18 N). Compression tests were carried out by means of an electromechanical dynamometer (Instron Mod. 3366) on samples cut from the extruded bars and tested through their thickness (cross-section: 5 x 5 mm^2), at a crosshead speed equal to 0.5 mm/min.

Shape memory tests on the material

The shape memory characterization on the material consisted of the programming of a temporary shape and of a subsequent recovery step, triggered by temperature and in which the shape changes were studied both as a function of increasing temperature, in the so-called thermally stimulated recovery (TSR), and as a function of time, *i.e.* under isothermal conditions. Different thermo-mechanical protocols were employed, as later described in the section relevant to programming, including a recovery characterization performed after a stress relaxation step.

Tests including TSR as the recovery protocol were carried out on samples with a rectangular cross-section, which is the most efficient geometry to easily grip inside the DMA tensile clamp. Conversely, tests including isothermal recovery were performed on samples with a circular cross-section, because

it's the same cross-section characterizing the protype, whose recovery was studied under isothermal conditions. For a schematic outline of all the tests performed, Table 4.3 is presented in the following.

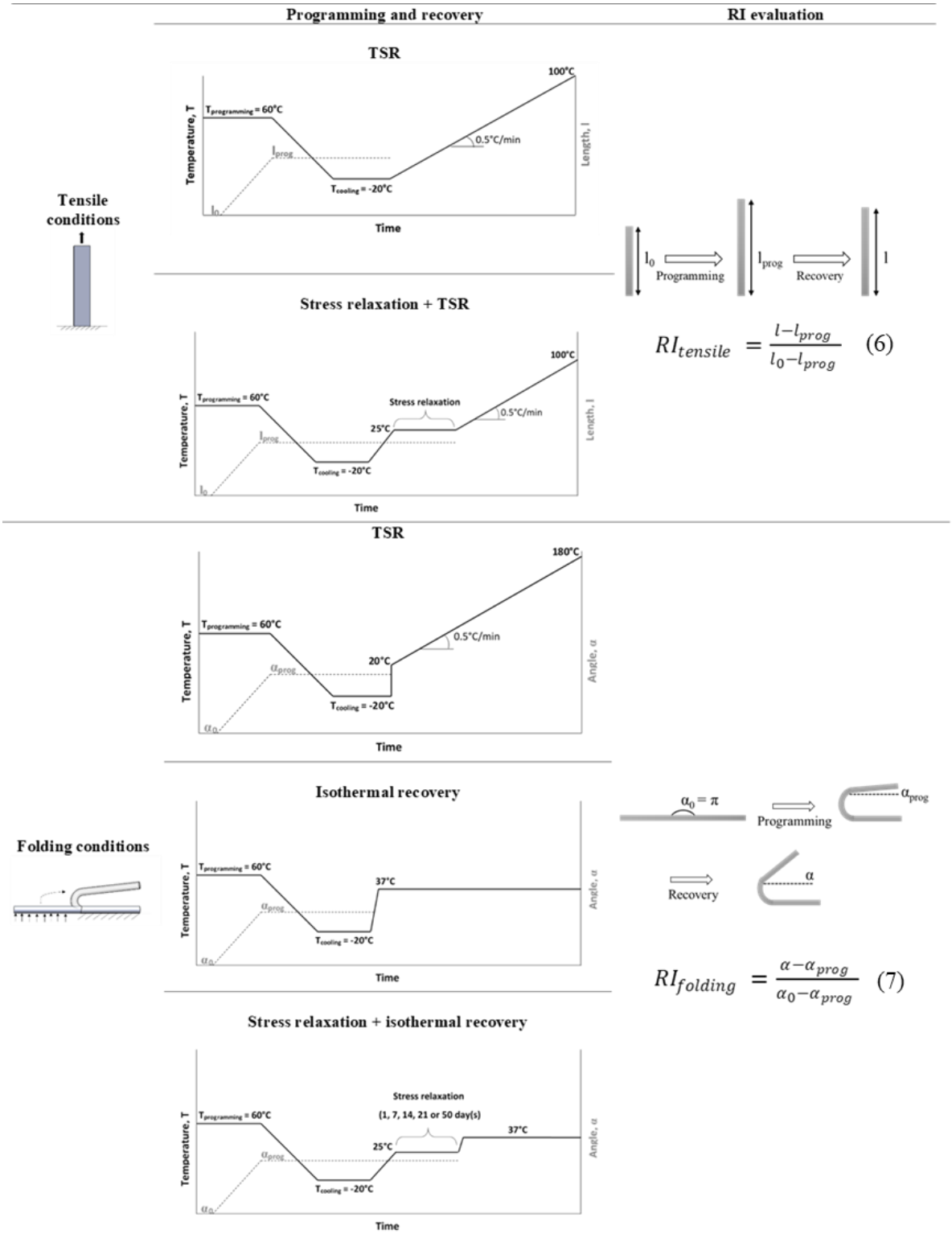

Table 4.3. Schematic outline of the various testing conditions for the shape memory characterization on the material.

Programming

The programming was carried out following the standard heating/cooling history, comprising heating above the transition temperature (60 °C) and thermal equilibration of the sample for 10 min, followed by the application of the deformation and finally cooling well below the transition temperature (-20 °C) under the imposed deformation. Two deformation conditions were employed: a tensile deformation and a bending one. The former consisted in the application of a ramp force at 1 N/min up to the maximum load allowed (18 N) by means of the dynamic mechanical analyzer (DMA Q800). The latter consisted in folding a straight specimen (labeled as I shape) to a U-shaped one by using an *ad hoc* built fixture.

Thermally stimulated recovery test (TSR)

TSR tests consisted in the application of a controlled heating ramp, in different conditions depending on the deformation previously applied in the programming.

TSR tests after tensile deformation were carried out in the DMA Q800 under tensile conditions applying a heating ramp from -20 °C to 100 °C at 0.5 °C/min under the application of a small load (0.005 N). The shape recovery performances were evaluated in terms of the extent of the deformation recovered as temperature increases with the recovery index $RI_{tensile}$ defined by Equation 6

$$RI_{tensile} = \frac{l - l_{prog}}{l_0 - l_{prog}} \quad (6)$$

where l is the length of the specimen during recovery, l_{prog} is the length after the programming step, and l_0 is the original length of the specimen.

TSR tests after folding the I shape into the U shape were carried out in a lab oven, fixing a half of the U-shaped sample to the oven plate, while leaving the other one free to move and to recover the deformation. The heating ramp was set from 20 °C to 180 °C at a heating rate of about 0.5 °C/min and the actual temperature was measured with a thermocouple places near the sample. Pictures of the recovery process were taken acquiring 1 frame / 20 s with a camera

(Nikon D700). The recovered deformation during the test was evaluated with the recovery index $RI_{folding}$ defined by Equation 7

$$RI_{folding} = \frac{\alpha - \alpha_{prog}}{\alpha_0 - \alpha_{prog}} \quad (7)$$

where all the angles, all measured in rad, are defined as shown in Table 4.3, with α being the angle between the arms during the recovery, α_{prog} the angle measured in the temporary shape ($\alpha_{prog} \approx 0$) and α_0 the initial angle ($\alpha_0 = \pi$).

Isothermal recovery test

U-shaped rods were subjected to isothermal recovery tests performed by placing the samples into a large enough crystallization vessel immersed into a thermoregulated bath so as to keep the temperature at 37 ± 1 °C. Temperature values were measured with a thermocouple placed near the sample. Pictures were taken throughout all the test and the recovery index was calculated using Equation 7.

Recovery tests on specimens after stress relaxation

TSR and isothermal recovery tests were carried out also on specimens which underwent a modified programming including at the end a period of stress relaxation under the imposed deformation at room temperature. In more details, for TSR tests specimens were deformed inside the DMA Q800 up to 10% of strain at 60 °C and cooled down to -20 °C under fixed strain. A thermal equilibration at 25 °C was applied to the specimen under fixed strain and held for a given relaxation time t_{rel} (t_{rel} = 0 min (no relaxation), 9, 90 and 900 min). Finally the strain was removed and the TSR protocol was applied with a heating ramp from 25 °C to 100 °C at 1 °C/min. For isothermal tests, the temporary U shape, kept in the fixture to block all potential motions, was equilibrated at room temperature (about 25 °C) and kept under static vacuum for a given t_{rel} (t_{rel} = 1, 7, 14, 21 and 50 days). Finally isothermal recovery was carried out by placing the U shape, free to recover the deformation, at 37 ± 1 °C.

Modeling and simulation

A three-dimensional generalized Maxwell model was used to describe the viscoelastic behavior of the material, as widely proposed in the literature[25,26]. Finite element simulation was used to implement the model and the Abaqus Standard finite element code (Simulia, Providence) was chosen since it already includes the model, its finite strain extension, as given by Simo[27], to describe large strain and either the Williams-Landel-Ferry equation or the Arrhenius one to express the time-temperature dependence[28]. The finite-strain viscoelasticity theory is available implemented in Abaqus in the time domain and, because of the large strain considered, has to be coupled to a hyperelastic material model to describe the rate-indipendent elastic response of the material. Moreover, the rate-independent elasticity can be defined in terms of either instantaneous elastic moduli or long-term elastic moduli, without effect on the solution. Additionally, in the numerical implementation of the model, the material is considered to be defined by a Prony series expansion of the relaxation modulus, whose series terms can be calibrated using frequency-dependent data, as the results obtained by multi-frequency DMA tests. In Abaqus, linear isotropic viscoelasticity is formulated in terms of the bulk modulus K and the shear modulus G; therefore, according to the Abaqus nomenclature, Equation 8 and 9 are used to relate the Prony series relaxation functions to the storage modulus $G'(\omega)$ and loss modulus $G''(\omega)$, under shear conditions:

$$G'(\omega) = G_0\left[1 - \sum_{i=1}^{N} \bar{g}_i^P\right] + G_0 \sum_{i=1}^{N} \frac{\bar{g}_i^P \tau_i^2 \omega^2}{1+\tau_i^2 \omega^2} \tag{8}$$

$$G''(\omega) = G_0 \sum_{i=1}^{N} \frac{\bar{g}_i^P \tau_i \omega}{1+\tau_i^2 \omega^2} \tag{9}$$

where $\bar{g}_i^P$ and τ_i are the Prony-parameters and G_0 represents the unrelaxed modulus (*i.e.* the instantaneous modulus - the modulus at time t = 0). The Prony-parameters are here calibrated on the storage and loss modulus master curves obtained in tensile conditions and the validation was performed on the loss angle (tan δ) master curve.

Furthermore, here the thermo-rheologically simple temperature effects are considered by using the Arrhenius form to define the shift function, as defined in Equation 10

$$\ln a_{T_0}^{T} = \frac{E_0}{R}\left(\frac{1}{T} - \frac{1}{T_0}\right) \quad (10)$$

where E_0, typically representing the activation energy of the relaxation process, has to be determined experimentally on the shift factor values employed for the master curve construction[24], R is the universal gas constant, T is the actual temperature, and T_0 is the reference temperature, both expressed as absolute temperatures.

Finally, the choice of the hyperelastic model to use was based on the experimental results of the mechanical tests carried out in the rubber-like plateau for which the Yeoh model represented a good fit, thus it was adopted under the hypothesis of incompressible material behavior. The strain energy potential function U(ε) for the Yeoh model is defined in Equation 11 as follows[29]

$$U = C_{10}(\bar{I}_1 - 3) + C_{20}(\bar{I}_1 - 3)^2 + C_{30}(\bar{I}_1 - 3)^3$$
$$+ \frac{1}{D_1}\left(J^{el} - 1\right)^2 + \frac{1}{D_2}\left(J^{el} - 1\right)^4 + \frac{1}{D_3}\left(J^{el} - 1\right)^6 \quad (11)$$

where U is the strain energy per unit of reference volume (*i.e.* volume in the initial configuration); C_{i0} and D_i are temperature-dependent material parameters; $\bar{I}_1$ is the first deviatoric strain invariant defined in Equation 12 as

$$\bar{I}_1 = \bar{\lambda}_1^2 + \bar{\lambda}_2^2 + \bar{\lambda}_3^2 \quad (12)$$

where the deviatoric stretches $\bar{\lambda}_i = J^{-\frac{1}{3}}\lambda_i$; J is the total volume ratio comprising the elastic volume ratio J^{el} and the thermal volume ratio J^{el} and λ_i are the principal stretches (*i.e.* the ratios of current length to length in the original configuration in the principal directions of a material fiber). Equation 11 is written as the sum of a deviatoric component $U(\bar{I}_1, \bar{I}_2)$ and a volumetric component $U(J^{el})$; therefore assuming incompressibility and the absence of thermal expansion, it can be written as in Equation 13

$$U = C_{10}(\bar{I}_1 - 3) + C_{20}(\bar{I}_1 - 3)^2 + C_{30}(\bar{I}_1 - 3)^3 \quad (13)$$

Under the same conditions, the first deviatoric strain invariant can be written in Equation 14 as

$$\bar{I}_1 = \lambda_1^2 + \lambda_2^2 + \lambda_3^2 \tag{14}$$

because $J = \det(\boldsymbol{F}) = 1$ and hence $\lambda_1\lambda_2\lambda_3 = 1$, being **F** the deformation gradient in the principal direction of stretch, defined as in Equation 15

$$\boldsymbol{F} = \begin{bmatrix} \lambda_1 & 0 & 0 \\ 0 & \lambda_2 & 0 \\ 0 & 0 & \lambda_3 \end{bmatrix} \tag{15}$$

The principal stretches λ_i are related to the principal nominal strains ε_i by Equation 16.

$$\lambda_i = 1 + \varepsilon_i \tag{16}$$

Details of the various simulations are reported in the Results and discussion section with respect to the experiment to simulate.

4.5 Results and discussion

The first part of this section demonstrates the feasibility of the Design Concept previously introduced. In fact, it mainly focuses on the illustration of the shape-shifting sequences achieved for both extruded and printed prototypes, which ensure easy administration and gastroretentive capability. The second part regards a thorough investigation on the material shape memory properties and their modeling in a finite element framework with the final potentiality of optimizing the prototype performances.

A key material property to obtain for the design of the desired shape-shifting sequences is the glass transition temperature T_g. Actually, the prototype has to be programmed into its temporary shape suitable for administration inside a capsule at a temperature above T_g and cooled down well below T_g to fix the deformed shape achieved. In addition, recovery takes place when the temperature of the prototype is higher than T_g. Therefore values of T_g were verified for all the formulations and they were found to be consistent with the results obtained for the intravesical drug delivery platform[30] described in Chapter 3. T_g is at about 25 °C, lower than body temperature T_{body}, irrespective of the formulation, as shown in Table 4.4.

System	T_g [°C]
PVA05GLY	24
PVA05GLY-ALP	23
PVA18GLY	25
PVA18GLY-ALP	24

Table 4.4. Glass transition temperature for different formulations obtained by FDM (for the PVA05-based systems) and HME (for the PVA18-based formulations). The T_g for PVA05 was evaluated as 57 °C, the T_g for PVA18 was measures at 64 °C.

Importantly, the presence of Allopurinol ALP did not affect the T_g, hence drug-containing formulations were found to have similar thermal properties of their counterparts not containing the active ingredient. The choice of ALP, which is a xanthine oxidase inhibitor used as the first-line therapy for gout an hyperuricemia, was the results of several considerations. In fact, it displays a great absorption window in the stomach because it is in its non-ionized form under acidic environment (pK_a 9.4), other than in the duodenum and in the upper

jejunum[31-33]; it was already proposed for administration in gastroretentive devices working upon floating and mucoadhesion[33]; furthermore, it is suitable for processing under high temperature characterizing both HME and FDM due to its high melting point (> 300 °C).

As a proof-of-concept of the 4D printing feasibility of gastroretentive devices, the 3D printing process was optimized for the PVA05GLY and PVA05GLY-ALP formulations, based on the experience previously gained with the same PVA grade[30], described also in Chapter 3. Successful prints of the cylindrical helix introduced in Figure 4.3 in the Design Concept section were achieved by setting the printing temperature to 190 °C and working under a low printing speed (23 mm/s) to avoid dragging of the layers. The programming of the temporary shape was accomplished by manually coiling the prototype into the helix with smaller diameter designed in Figure 4.3, compliant to the dimensions of the DB caps® size AA capsule. Pictures of the actual 4D printed prototype in its permanent shape and the temporary one are shown in Figure 4.10.

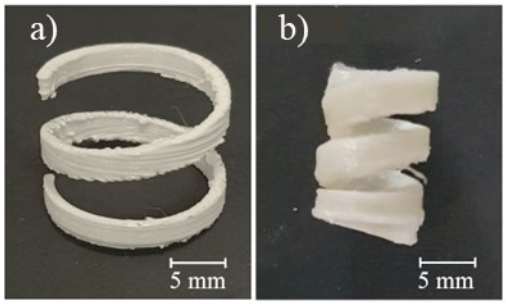

Figure 4.10. Pictures of the prototype obtained by FDM printing of PVA05GLY-ALP in its a) permanent shape (cylindrical helix), b) temporary shape (supercoiled).

The FDM cylindrical helix prototype resulted to have an average weight of 571.70 mg (coefficient of variation, cv = 7.31) and drug load of 9.82% (cv = 4.06).

The device in its temporary shape was fitted inside the chosen capsule, not available in the transparent version, and both the recovery of the permanent shape and the release of the drug were studied by immersing the prototype in simulated gastric fluid (HCl 0.1N) kept at 37 ± 0.5 °C.

Shape changes were qualitatively followed by taking pictures throughout all the recovery, lasted for 10 min and resulting in the achievement of a recovered shape that can be considered very close the initial permanent one, as shown in Figure 4.11.

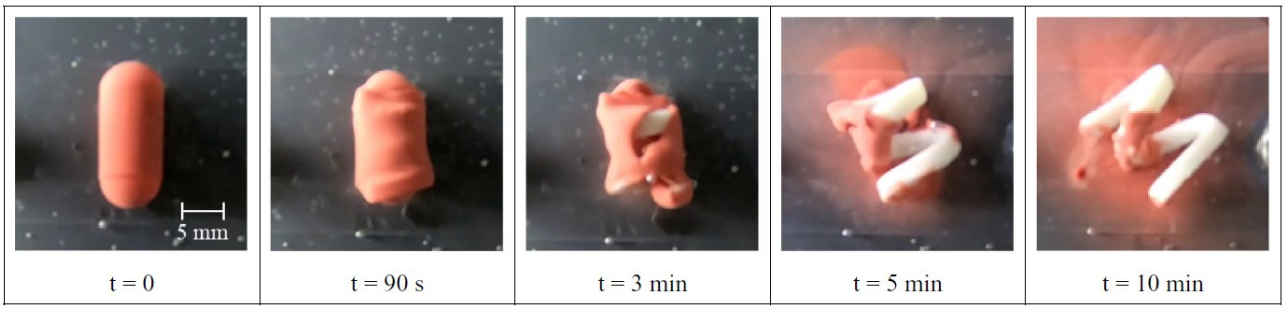

Figure 4.11. Pictures taken during shape recovery of a cylindrical helix printed from the PVA05GLY-ALP formulation at given time points.

Moreover the breakup of the capsule was observed to be completed in 3 min, significantly in contrast to the breakup time of unfilled capsules under the same conditions. In fact, the same capsules filled with a blue powder tracer started to open up after 10 min, as it is possible to evaluate thanks to solvent staining. The shorter breakup time for device-containing capsules was explained as the consequence of the pressure exerted by the device itself, when in the process of recovering its permanent shape under the constraint of the capsule. After the capsule breakup, the prototype is directly exposed to the acidic medium and, thanks to the combined effect of temperature and water on the shape memory response of PVA already demonstrated in Chapter 3 and in [30], the recovery occurred at a faster rate.

The release profile of the prototype while undergoing the shape changes responsible for gastric retention is presented in Figure 4.12.

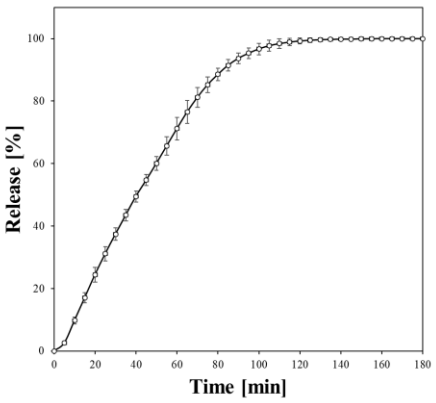

Figure 4.12. Average release profile with error bas from a cylindrical helix printed from PVA05GLY-ALP, inserted into a AA sized capsule after programming of the temporary supercoiled shape.

The drug release was proved to be sustained over a period of 2 h after immersion in the acidic medium.

In order to test another grade of PVA to use in the attempt of better control the drug release profile, PVA18 was selected for manufacturing of plasticized formulations containing the active ingredient. However, given the higher viscosity, FDM was not feasible with the current equipment available and the demonstration of the proof-of-concept was carried out on prototypes obtained by HME. The permanent shapes obtained together with their corresponding temporary ones, on the base of the drawings reported in the Design Concept section in Figure 4.4, 4.5 and 4.6 and the templates used to impart the deformed shapes are shown in Figure 4.13.

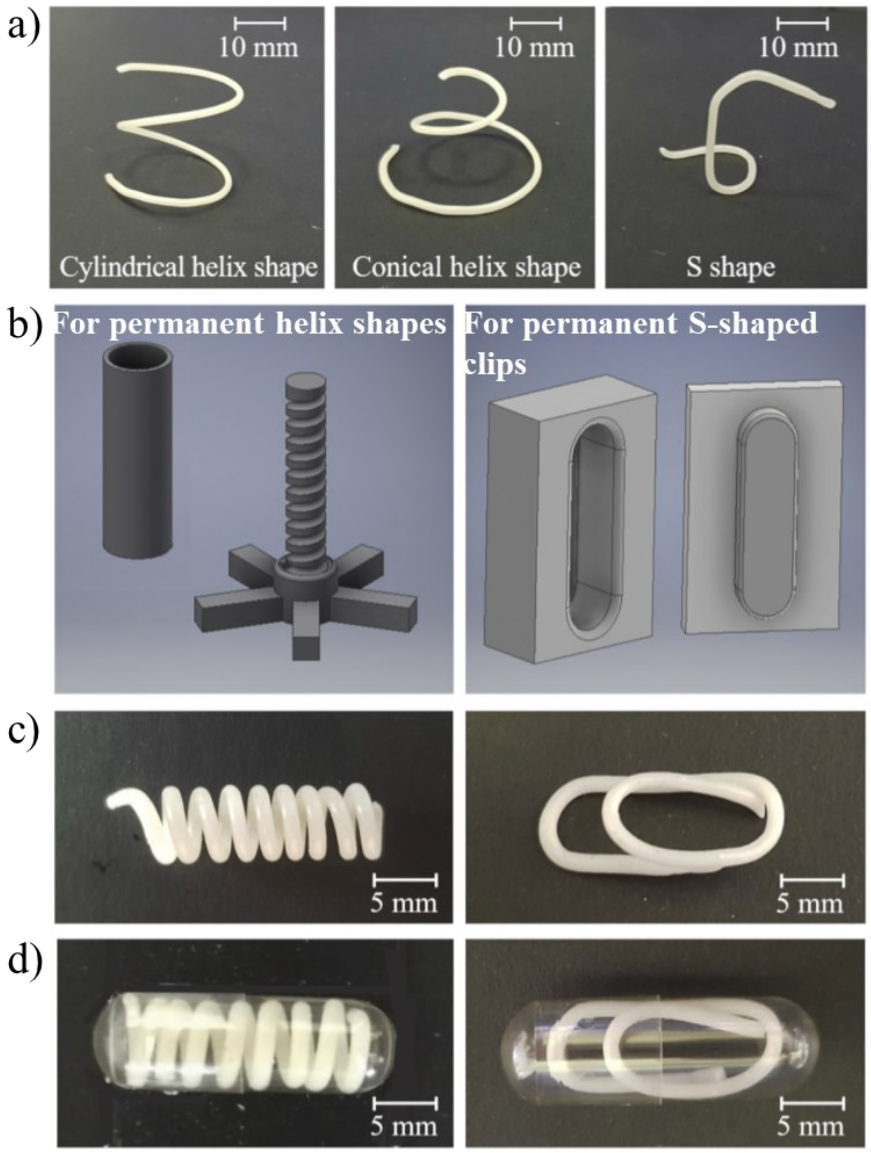

Figure 4.13. a) Pictures of the prototypes obtained by HME of PVA18GLY-ALP; b) CAD 3D drawings of the templates used to impose the temporary shape; in c) and d) pictures of the prototypes in their temporary shapes (supercoiled helix and paper-clip shape) before and after encapsulation, respectively.

The use of the templates was useful to enhance the reproducibility of the deformation process into the temporary shapes, making it less dependent on the operator. More in details, the two permanent helix shapes were wrapped around a rod with a smaller pitch with a circular cross section, represented in Figure 4.13b (left), so as to obtain supercoiled helixes, *i.e.* items with shorter length and diameter, as shown in Figure 4.13c (left). The three-dimensional S-shaped clip was forced to take on a planar temporary shape, similar to a paper clip, as depicted in Figure 4.13c (right). In Figure 4.13d, pictures of the encapsulated prototypes are presented, demonstrating that both the temporary shapes were effectively fitted inside the 00el capsule, as designed in the Design Concept section and shown in Figure 4.4, 4.5 and 4.6.

The choice of investigating the performances of prototypes with three different permanent shapes was justified by the interest in following the resulting shape-shifting motions and by the possibility of pursuing a personalized dose modification. In fact, the extruded rods used for the three different shapes had different length, resulting in different weights, as reported in Table 4.5 and, consequently, in loading differing amounts of the drug.

Prototype	Weight [mg] (cv)
Cylindrical helix	300.07 (3.17)
Conical helix	298.62 (4.09)
S shape	140.87 (5.21)

Table 4.5. Weigh of the prototypes obtained by HME of PVA18GLY-ALP having different permanent shapes.

Furthermore, the amount of ALP effectively loaded in the prototypes was found to be consistent with the nominal one, about 99% of the nominal value, meaning that during HME significant loss of drug didn't occur.

Release profiles were obtained for all the prototypes and for the cylindrical helix coated with Eudragit® RS/ Eudragit® RL 1/1 and the results are reported in Figure 4.14.

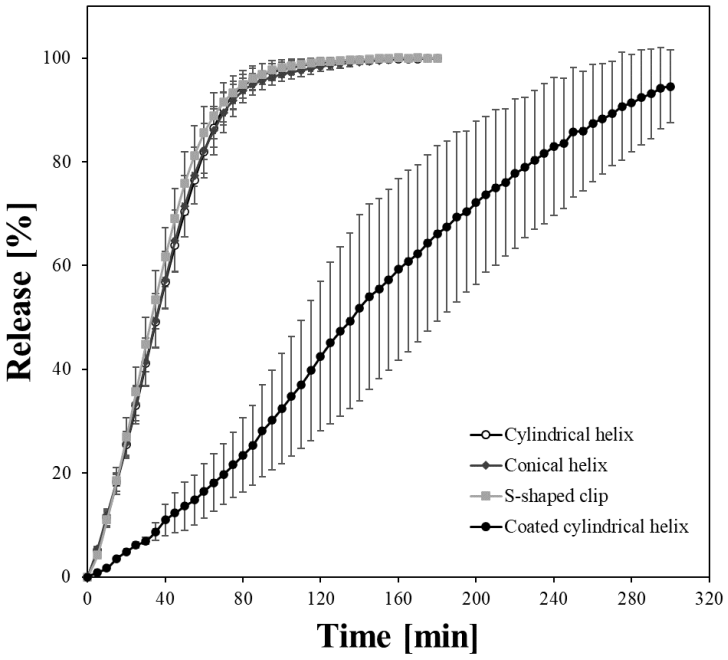

Figure 4.14. Average release profiles with their error bars from uncoated and coated prototypes obtained by HME of PVA18GLY-ALP.

Superimposable profiles were obtained for all the uncoated prototypes, irrespective of the length and the mass of the extruded shape, lasting for approximately 2 h. In spite of the use of a higher molecular weight PVA with respect to the one manufacture by FDM, whose release profile was shown in Figure 4.12, the release performance was not improved, *i.e.* it was not extended. A possible explanation may lie in the higher surface/volume ratio measured for extruded systems (about 4 mm^{-1}) as compared to the printed one (3.5 mm^{-1}), which is known to impact on the release rate and which could have helped in speed up the release for the extruded PVA despite its higher molecular weight. Therefore, another strategy relying on the application of an insoluble/permeable coating was pursued and successfully resulted in the extension of the release profile over about 5 h, as shown in the curve for the coated cylindrical helix shown in Figure 4.14.

All the prototypes deformed in their temporary shape and encapsulated in the 00el transparent carrier were tested for their recovery performance and, by way of example, pictures representing the recovery for the conical helix shape immersed in the acidic medium at T_{body} were reported in Figure 4.15.

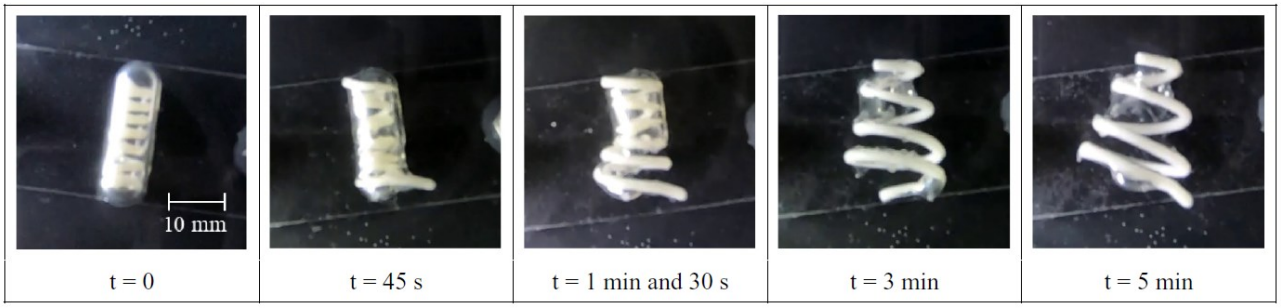

Figure 4.15. Pictures taken at different time points during the shape recovery for the conical helix obtained by HME of PVA18GLY-ALP, inserted into the 00el Coni-Snap capsule in its temporary shape and immersed in HCl 0.1N at 37 °C.

For this coupling between the 00el capsule and the extruded prototype, the breakup of the capsule was observed after 45 s, occurring even faster than the one characteristic of the system AA size capsule and printed prototype shown in Figure 4.11. A quantitative evaluation of the shape recovery for all the prototypes was carried out by building the recovery index RI curves based on Equation 1 and 2 for the cylindrical and conical helix respectively and on Equation 3, 4 and 5 for the S-shaped clip. A spatial encumbrance theoretically ensuring gastric retention is considered to be reached when at least two geometrical dimensions of the prototypes become greater than 13 mm during the recovery. Therefore, in Figure 4.16a, 4.17b, 4.17c, 4.17d and 4.17e the RI curves as a function of time are reported together with a dashed horizontal line indicating the threshold for gastric retention, depending on the geometry of the prototype considered.

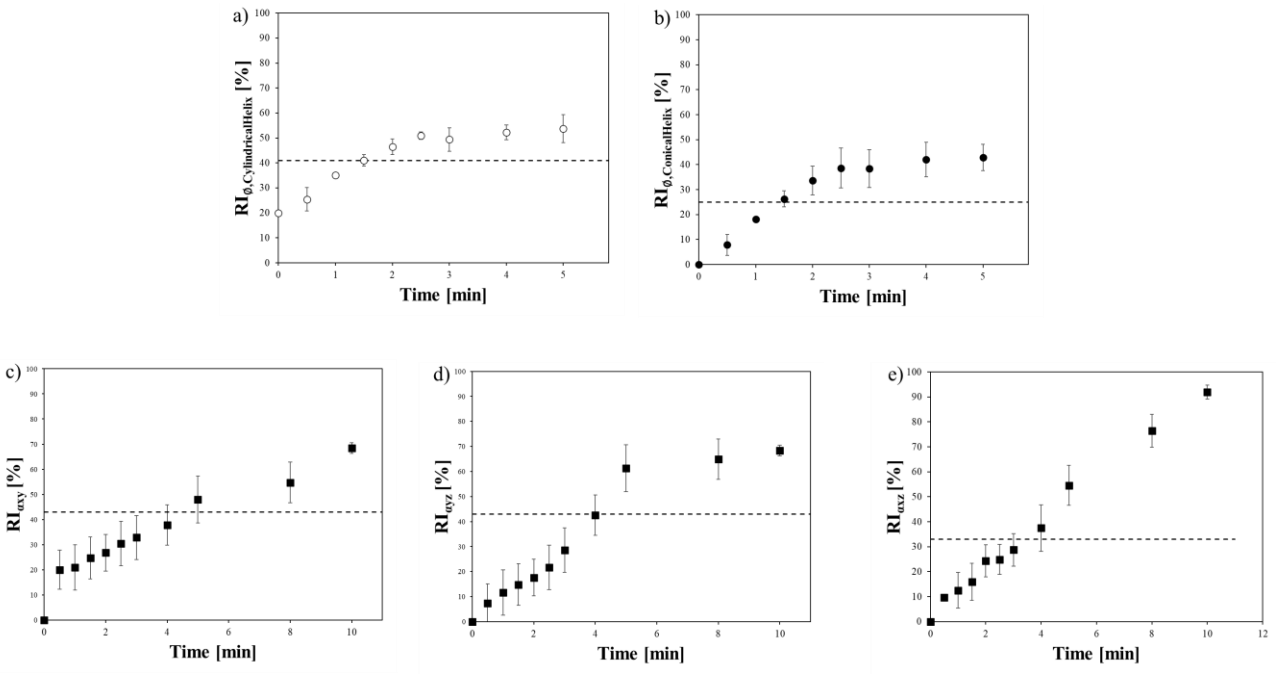

Figure 4.16. Recovery index RI *versus* time curves for the prototypes having as permanent shape a) cylindrical helix, b) conical helix, c) d) and e) S shape.

Figure 4.16a and Figure 4.16b represented the recovery curves for cylindrical and conical helixes respectively. For both these prototypes, the length of the supercoiled temporary shape was already greater than the threshold (about 20 mm); therefore, the achievement of the desired spatial encumbrance was considered to be accomplished when also the diameter of the helixes became equal or greater than 13 mm, specifically equal to a value of 14.5 mm considering a factor of safety. This latter condition corresponds to the achievement of a $RI_{\emptyset,CylindricalHelix}$ equal to 41 % and $RI_{\emptyset,ConicalHelix}$ equal to 25 %, for cylindrical and conical helixes respectively. The threshold was reached in less than 2 min in both cases and, at the end of 5 min of testing, RI values reached a plateau equal to 58 % and 42 % for cylindrical and conical helixes respectively, which corresponds to approximately the 70% and the 52% of the initial diameter (17.5 mm and 18.7 mm for cylindrical and conical helixes, respectively).

Recovery curves for the S-shaped clip are reported in Figure 4.16c, 4.16d and 4.16e, since the opening of the temporary planar paper-clip involved the evaluation of the three angles α_{xy}, α_{xz}, and α_{yz} evaluated by means of Equation 3, 4 and 5. For the geometry of this prototype, the required spatial encumbrance is reached when at least two angles widened enough reaching the values of 43°, 32° and 33° for α_{xy} α_{yz}, and α_{xz}, respectively. All the three angles reached their relevant threshold within 5 min of testing and kept increasing achieving approximately the 70% of the recovery for α_{xy} and α_{xz} and the 90% for α_{xz} at 10 min. The lower values found for α_{xy} and α_{xz} might result from friction of the prototype against the bottom surface of the crystallization vessel and consequently a hindered recovery, whereas in the xz plane the prototype was free to move and to change shape without any obstacle.

For all the prototypes the time needed to reach the threshold dimensions was relatively short, as the consequence of the combined effect of temperature and fast water uptake of the systems. This was considered advantageous, since the time needed to achieve the bulky retentive configuration has to be the shortest possible, once the device arrives into the stomach, because late expansion might result in small intestine location of the system. This wrong location might lead to clogging of the canal and also loss of the absorption window with consequent reduction of bioavailability.

Therefore, a first *in vitro* demonstration of the performances of the proposed gastroretentive devices was accomplished, identifying as one of the more promising systems the S-shaped clip which is folded into a planar paper-clip suitable for capsule administration. This prototype, hence, was the subject of the simulation activity through finite element modeling, which was founded on the results of the second set of tests presented in the following. The material investigated was the PVA18GLY formulation.

DSC and DTMA analyses were performed to gain first insight on the macromolecular structure responsible for the shape memory effect. The cooling and second heating scans from DSC analysis and the evolution of the storage and loss moduli as a function of temperature from a single-frequency DMTA test are reported in Figure 4.17a and 4.17b respectively.

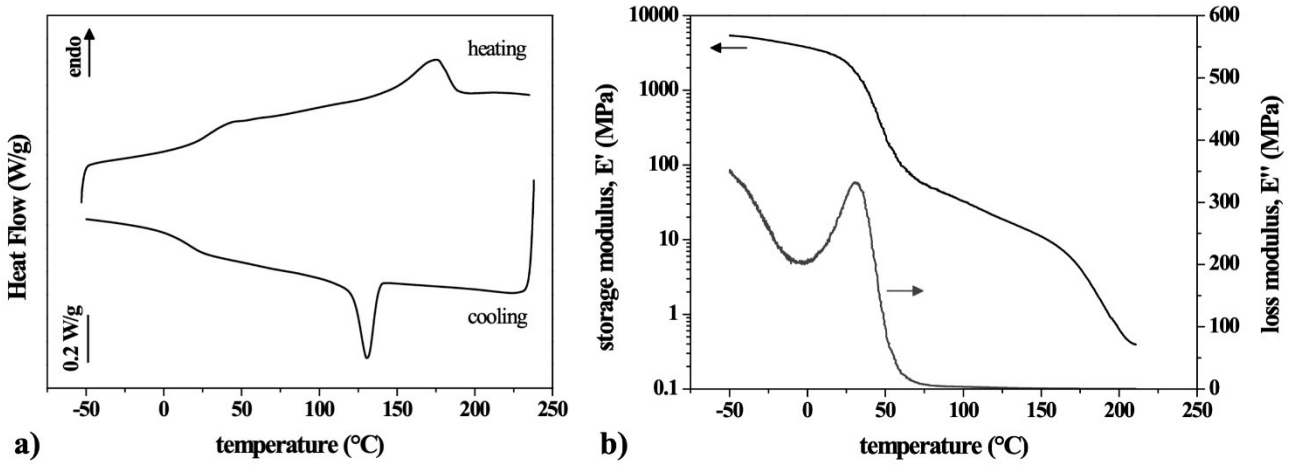

Figure 4.17. Results from thermal and thermo-mechanical analyses on PVA18GLY obtained by HME. a) DSC thermograms showing the cooling and second heating scan; b) DMTA curves of the storage modulus and loss modulus as a function of temperature at 1 Hz.

From Figure 4.17a the T_g was confirmed to be slightly above room temperature, at about 27 °C in the here presented heating scan, and more importantly also the melting T_m and the crystallization T_c temperatures were identified at 179 °C and 132 °C respectively. Additionally, the crystallinity content was calculated from the enthalpy at melting (ΔH_m = 25.9 J/g) and resulted equal to about 18.7% (under the assumption of melting enthalpy for 100% crystalline PVA equal to 138.60 J/g[34]). These considerations highlighted the possibility of observing significant viscoelastic effects including stress relaxation and strain recovery at room temperature due to the measured T_g value; whereas the crystalline domains required high temperatures, well above the

temperature used in the programming of the temporary shape T_{def} = 60 °C, to be modified and melted. Likewise, the DMTA results shown in Figure 4.17b allowed to identify the extension of the glass transition region from room temperature up to 60 °C with a T_g value of 33 °C, as evaluated from the peak of the loss modulus curve. These results, all together, may help in the interpretation of the shape memory effect for this material, as outlined in the scheme of Figure 4.18, for which the polymeric segments undergoing the glass transition can be considered the molecular switchers of the chain mobility, conversely the crystalline domains can be considered as the "hard domain" capable of preventing the viscous flow of the polymeric chains thus ensuring the recovery.

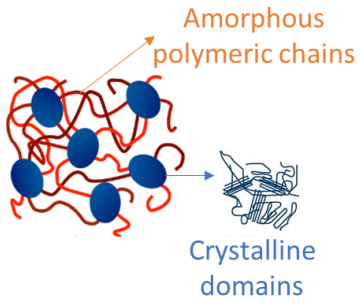

Figure 4.18. Schematic representation of the macromolecular structure of the PVA responsible for its shape memory response.

An additional thermo-mechanical analysis was conducted with the aim of investigating the potential presence of thermal strains and shrinkage effects on freshly extruded samples when subjected to a heating ramp inside the dynamic mechanical analyzer under quasi-stress-free conditions. In fact, the presence of internal stresses, deriving from the processing history of the material, may result in shape changes, including axial shrinkage and/or flexural bending, which might disturb and complicate the measurement of the shape memory response. As shown in Figure 4.19, the measured strain was plotted as a function of temperature and the shrinkage behavior was related to the deviation from an ideal baseline (dashed line in the plot) representing the thermal expansion of the specimen.

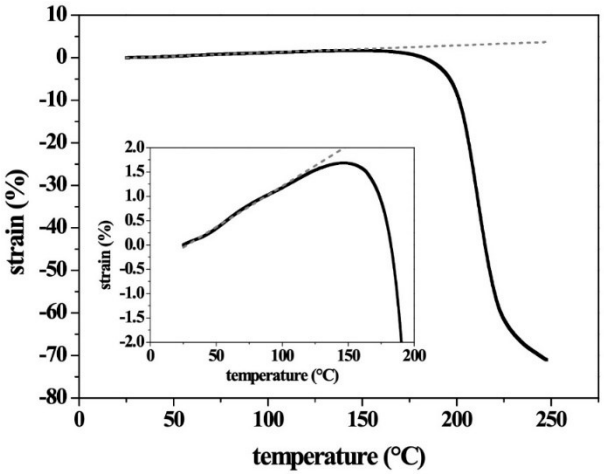

Figure 4.19. Quasi-stress-free strain change due to shrinkage of the specimen obtained by HME of PVA18GLY along a heating ramp. The dashed line is reported as baseline representing an ideally pure thermal expansion. Inset: magnification of the shrinkage curve and of the base line for temperatures up to 180 °C.

A significant shrinkage process was found to occur from about 160 °C up to 250 °C reaching a value of negative strain equal to 75%, however its importance at lower temperature can be considered negligible, with a deviation from the baseline starting at about 100 °C and summing up to only 1% at about 150 °C, as more evident in the inset of the figure. Therefore, it was possible to conclude that strains deriving from frozen stress are released for higher temperatures than the one characterizing the glass transition region, which represents the temperature zone in which the shape recovery takes place. Indeed, the shape memory response is the result of the increase in chain mobility occurring over time and promoted by the temperature and it is driven by the entropic elasticity of the material in the rubber state.

Therefore, on the basis of the viscoelastic interpretation of the shape memory effect, the thermo-viscoelastic generalized Maxwell model introduced in the Methods section was chosen and the required material parameters were derived from the master curve description of the mechanical dynamical response of the material. The results of the multi-frequency DMTA test are reported in Figure 4.20a, 4.20b and 4.20c along with the calibrated curves obtained from the model.

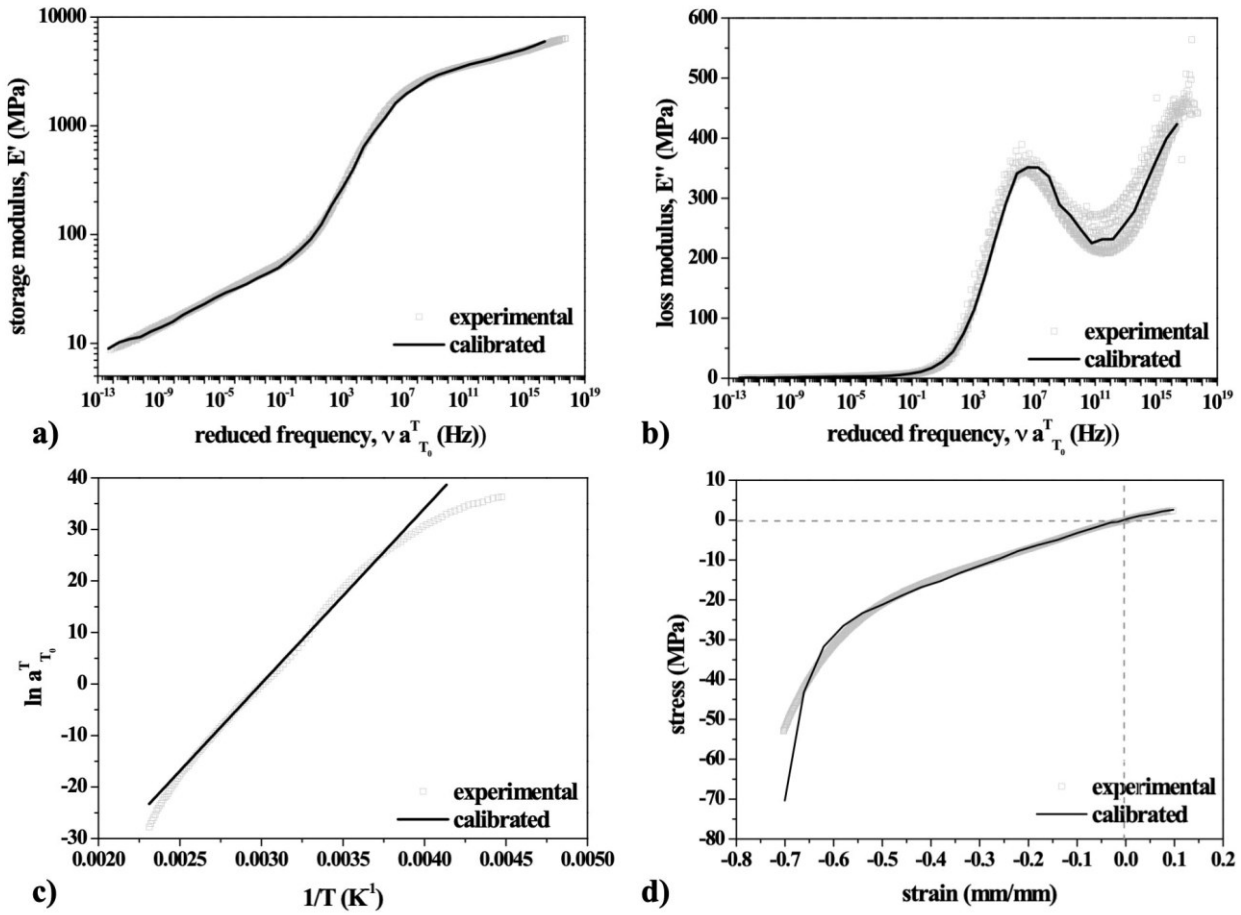

Figure 4.20. Experimental curves (grey dots) versus calibrated (black solid line) for the PVA18GLY formulation obtained by HME for: a) the storage modulus; b) the loss modulus; c) Arrhenius approximation of the calculated horizontal shift factors and d) experimental stress-strain curve (both under tension and compression) versus calibrated curve at 60 °C. As a reference, the value of $1/T_g$ is 0.00327 K^{-1}.

The storage, loss moduli master curves (Figure 4.20a and 4.20b) and tan δ master curve were obtained by applying a frequency-temperature equivalence principle for the reference temperature chosen as T_0 = 60 °C. More in details, the isothermal curves resulting from the frequency sweeps (here not shown) were rigidly shifted until best superposition. The results showed a continuous decrease of the storage modulus, from high values about 3-7 GPa for high frequencies to values between 100 and 10 MPa at frequencies below the relaxation one. In Figure 4.20c the shift factor dependence on the inverse of absolute temperature was plotted: an Arrhenius dependence could be recognized with multiple slopes in the glassy regions, whereas across the glass transition a Williams-Landel-Ferry dependence was harder to identify lying between 25 °C (1/T = 0.00335 K^{-1}) and 80 °C (1/T = 0.00283 K^{-1}).

Furthermore a good fitting was achieved for both the storage and loss modulus master curves, as shown in Figure 4.20a and 4.20b, by using the generalized Maxwell model and implementing an optimization procedure[35] in Matlab, resulting in 33 Maxwell elements. The corresponding Prony parameters $\bar{g}_i^P$ and τ_i, as employed in the definition of Equation 8 and 9, are listed in Table 4.6.

$\bar{g}_i^P$	τ_i [s]	$\bar{g}_i^P$	τ_i [s]	$\bar{g}_i^P$	τ_i [s]
0.00374141	1.00E-21	0.0607589	1.00E-10	0.00102984	10
0.00375453	1.00E-20	0.0802685	1.00E-09	0.000989874	100
0.00388872	1.00E-19	0.0742552	1.00E-08	0.00066613	1000
0.00576913	1.00E-18	0.0940951	1.00E-07	0.000693835	10000
0.126106	1.00E-17	0.061216	1.00E-06	0.000649501	100000
0.0858064	1.00E-16	0.0538247	1.00E-05	0.00053126	1.00E+06
0.0663233	1.00E-15	0.0237761	0.0001	0.000536651	1.00E+07
0.0675624	1.00E-14	0.0148667	0.001	0.000302641	1.00E+08
0.04612	1.00E-13	0.00610823	0.01	0.000310251	1.00E+09
0.056199	1.00E-12	0.0032505	0.1	6.80E-05	1.00E+10
0.0528531	1.00E-11	0.00197859	1	0.000322855	1.00E+11

Table 4.6. Prony parameters of the generalized Maxwell model: normalized moduli, $\bar{g}_i^P$ and relaxation times, τ_i, evaluated at T_0 = 60 °C.

Additionally the time-temperature dependence was fitted on the experimental curve of the shift factor *versus* the inverse of the absolute temperature. As shown in Figure 4.20c, a good approximation of the experimental trend was obtained by using the Arrhenius equation, reported in Equation 10, over a set of temperature between -20 °C (1/T = 0.0039 K^{-1}) and 115 °C (1/T = 0.0026K^{-1}) and taking T_0 equal to the reference temperature (60 °C). The interval chosen provided a fairly linear correlation and moreover, it covered the whole temperature region involved in the shape memory cycle. E_0 resulted equal to 282.38 kJ/mol for the fitting shown in Figure 4.20c.

Finally, in Figure 4.20d the experimental stress versus strain curve measured under tensile and compressive conditions are reported along with the calibrated curves obtained by the application of the Yeoh model to describe the hyperelastic material behavior for temperatures higher than T_g. The parameters employed in the

definition of Equation 13 resulted equal to the following values: C_{10} = 4977901.74 MPa, C_{20} = -1063924.80 MPa and C_{30} = 148187.61 MPa

The multi-frequency DMTA results were considered useful also in order to describe the relaxation modulus as a function of time. This was attempted in Figure 4.21 under the approximation that E ≃ E' and that the reduced time is $t/a_{T0}^{T} \simeq (\omega a_{T0}^{T})^{-1}$, for two different reference temperature T_0 = 25 °C and T_0 = -15 °C.

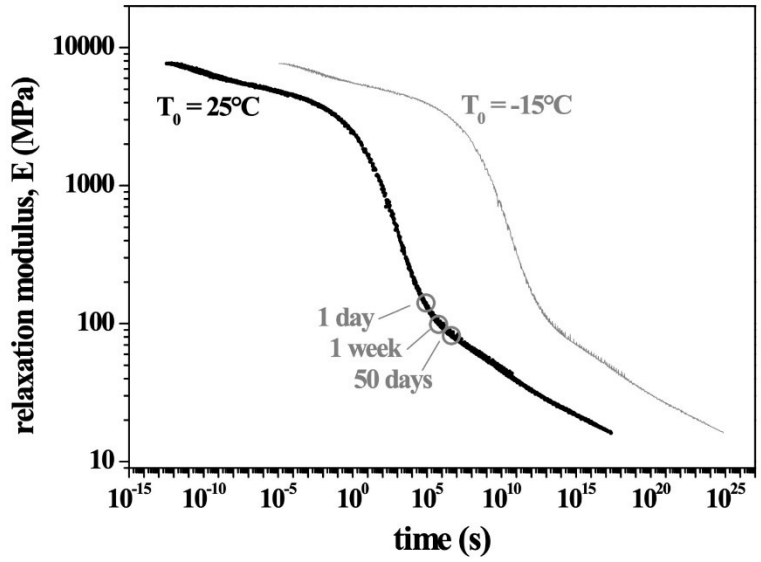

Figure 4.21. Approximate relaxation modulus master curve as a function of time for a temperature T_0 = 25 °C in black, with relevant instants for the relaxation process; in grey: master curve for a temperature T_0 = -15 °C. Both curves are referred to the PVA18GLY formulation obtained by HME.

The description of the relaxation modulus was pursued specifically with the aim of describing the stress relaxation occurring under the fixed strain represented by the encapsulation of the device in its temporary shape in the capsule. More in details, the curve represented for T_0 = 25 °C suggested that at this temperature, commonly considered in the storage of medicinal products under standard shelf life conditions, a large portion of the relaxation process took place in short time as highlighted by the circle drawn in Figure 4.21 in correspondence of 1 day and 1 week, after which the material entered in its rubbery region. After 50 days, the material is in its relaxed state and the modulus got reduced to about 1% of its unrelaxed value (*i.e.* the value measured at the shortest time). Conversely, the curve at T = -15 °C, which is a typical valued for low temperature storage, is shifted towards higher time, suggesting slower relaxation. In fact the modulus maintains its glassy value at 1 day and the material approaches its transition region at 50 days, with a modulus still high,

equal to about 2 GPa. Therefore, for storage of the encapsulated device at room temperature, a significant relaxation process may occur and its effect on the shape memory response is not known a priori. It can be hypothesized that the relaxation process could help in achieving a better fixing of the temporary folded shape, while partially erasing the permanent one. In fact, the presence of the constraint provided by the capsule could prevent the spontaneous recovery that would take place under strain-free conditions. As a consequence, the shape memory response was worthy to be studied not only in the standard conditions but also after having imposed a constraint on the temporary shape for different periods of time.

The Figure 4.22a displays the results for a standard shape memory protocol with a thermally stimulated recovery (TSR), sketched in the inset of the figure, carried out on an extruded bar under tensile conditions, in terms of the recovery index $RI_{tensile}$, defined in Equation 6, *versus* temperature.

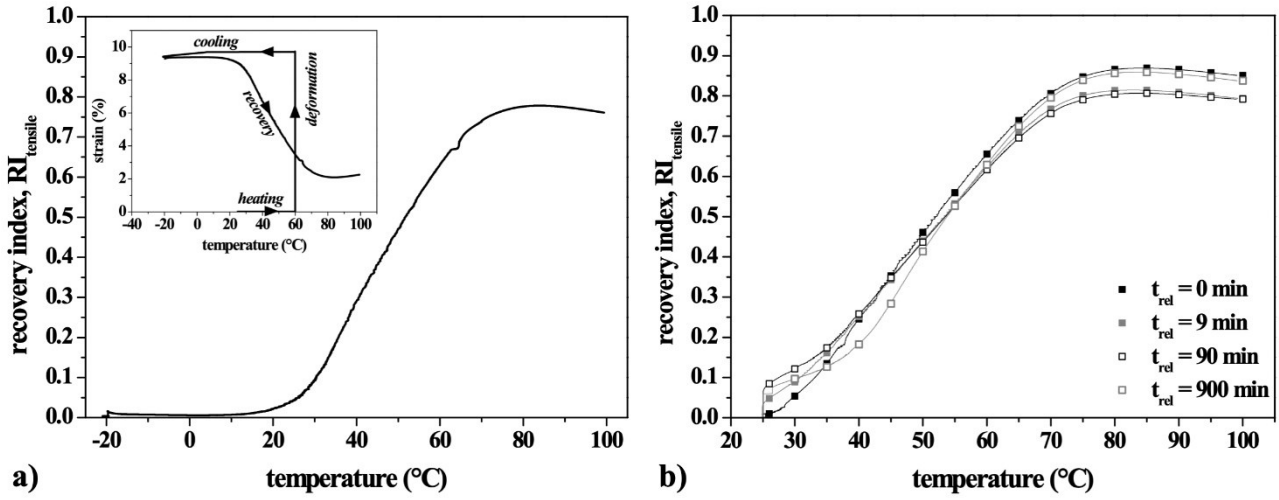

Figure 4.22. Recovery index, $RI_{tensile}$, curves as a function of temperature along a heating ramp for a specimen subjected to recovery a) right after cooling under fixed strain and b) for various relaxation times under fixed strain (0, 9, 90 and 900 min). Inset of Fig. 4.22a: Representation of the shape programming and recovery protocol in terms of strain vs temperature. The results are relevant to specimens obtained by HME of PVA18GLY.

The recovery of the applied strain started at about 10 °C and the slope of the curve became steeper above 30 °C, leading to an almost complete recovery (84%) at 80 °C. The later inversion of the recovery could be ascribed to the presence of only the thermal expansion of the sample, which is a process that goes in the opposite direction to the recovery, that in these conditions lead to a reduction of the length of the sample.

Similar TSR tests were carried out also on specimens stretched in their temporary shapes and subjected to stress relaxation at room temperature and their results are shown in Figure 4.22b. For all the relaxation times tested, the recovery curves followed a similar trend, with the recovery process starting immediately after unloading. However, the higher was the relaxation time imposed, the higher was the extent of the instantaneous recovery as measured with the first step increment of the recovery index. This contribution was ascribed to an elastic, or short-time viscoelastic, response, which became more significant as t_{rel} increased, ascribing this response to a more pronounced increase in their internal energy as a consequence of their attempt to recover their permanent shape, hindered by the presence of the fixed strain. After the instantaneous recovery step, samples which underwent higher t_{rel} showed an initial lower rate but above 50 °C and at the end of the recovery, no dependence on the relaxation history was recognized with the maximum $RI_{tensile}$ indexes varying slightly between 81% and 87%. For the time scale that was possible to explore in the dynamic mechanical analyzer, it was found that the relaxation step did not affect the final extent of the recovery which is the important parameter for the intended application, but only the initial, elastic spring-back contribution.

The shape memory performances were studied also in test on specimens under bending conditions, being this deformation mode more resembling to the one imposed on the gastroretentive prototype. Shape recovery was studied after folding the straight specimens into U-shaped ones and following their shape motions both under the TSR protocol and under isothermal conditions, and their results are presented in terms of $RI_{folding}$, defined as in Equation 7, in Figure 4.23a and 4.23b, respectively.

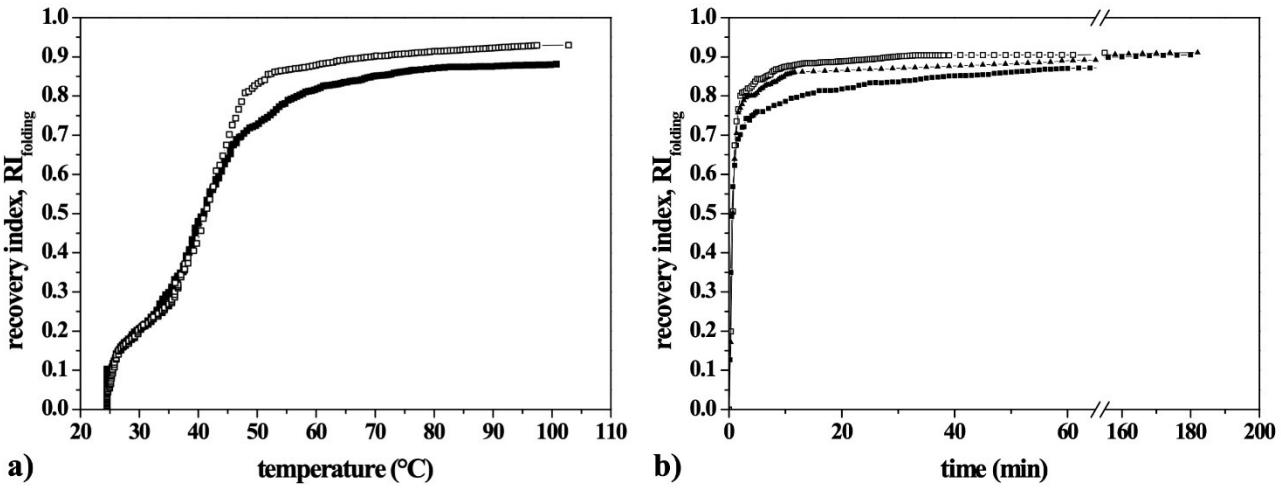

Figure 4.23. Recovery index, $RI_{folding}$, curves a) as a function of temperature in TSR tests and b) as a function of time in isothermal recovery tests at 37 °C, for I shape specimens obtained by HME of PVA18GLY folded into a U shape.

The results of the TSR tests shown in Figure 4.23a confirmed the ones obtained under tensile conditions, reported in Figure 4.22a, with a recovery process that onsetted at room temperature and achieved high rate at about 45 °C resulting in a finally recovery index $RI_{folding}$ of about 90%. In the case of the folding deformation, the recovery can be considered complete already at about 55 °C. In Figure 4.23b, the results of isothermal recovery tests carried out at T_{body} (37 °C) are reported, showing that only few minutes are required to reach significant $RI_{folding}$ values of approximately 70% and that the process can be considered complete in a time window ranging from 10 to 40 min. Furthermore, being the recovery at the constant temperature of 37 °C the final target of this study considering the intended application for the gastroretentive device, additional recovery tests comprising the effect of a relaxation period at room temperature, simulating in this way the effect provided by the capsule to the encapsulated device, were carried out also under these folding conditions of deformation. The results are reported in Figure 4.24 in terms of the evolution of the $RI_{folding}$ with time for relaxation times ranging from 1 to 50 days. Tests were done on triplicates for each t_{rel} and their relevant standard deviation was reported only in Table 4.7 in order to improve the clarity of the figure.

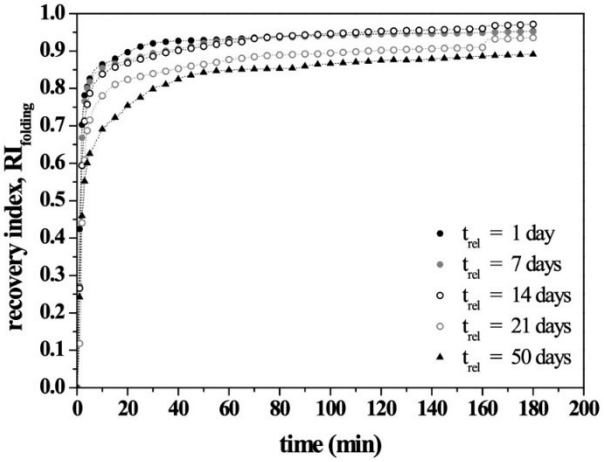

Figure 4.24. Recovery index, $RI_{folding}$, curves for isothermal experiments carried out at 37 °C on U-shaped folded specimens from extruded PVA18GLY, maintained in that shape at room temperature for various times (1, 7, 14, 21, 50 days) before the recovery experiment.

Relaxation time, t_{rel} [d]	$RI_{folding}$ at 1 min	$RI_{folding}$ at 10 min	$RI_{folding}$ at 20 min	$RI_{folding}$ at 180 min
1	0.42 ± 0.28	0.86 ± 0.05	0.90 ± 0.04	0.95 ± 0.02
7	0.27 ± 0.14	0.85 ± 0.01	0.87 ± 0.02	0.95 ± 0.03
14	0.26 ± 0.18	0.84 ± 0.08	0.87 ± 0.08	0.97 ± 0.04
21	0.12 ± 0.12	0.78 ± 0.05	0.82 ± 0.04	0.93 ± 0.01
50	0.24 ± 0.12	0.69 ± 0.10	0.75 ± 0.09	0.89 ± 0.03

Table 4.7. Recovery index $RI_{folding}$ data, measured at various recovery times, in isothermal experiments carried out at 37 °C on U-shaped folded specimens from extruded PVA18GLY, maintained in that shape at room temperature for various times (1, 7, 14, 21, 50 days) before activating recovery.

An effect of the t_{rel} on the recovery response can be recognized, as partially expected. In fact, on average, $RI_{folding}$ values for any given time point were found to be lower especially for samples subjected to long relaxation times (21 and 50 days) compared to the ones which underwent shorter relaxation. On the other hand, the rate of the recovery after the initial 10 min seemed to be independent from the relaxation times, with final high $RI_{folding}$ values, from 90 to 95% at the end of 3 h. Interestingly, for all the explored conditions, a significant recovery is reached already in the first 10 min of testing (about 70%). This is considered optimal for the application, being independent from the presence of a constraint – as the capsule can be, and for which a quick recovery up to high percentage of the applied deformation is desired.

After the experimental investigation of the shape memory response under different deformation conditions comprising the presence of a stress relaxation period, the model calibrated on the Figure 4.20a, 4.20b and 4.20c was validated on the experimental results regarding flexural deformations applied to the straight specimen. This specimen geometry was meshed by using eight-node linear isoparametric hexahedral elements, reduced integration with hourglass control, hybrid with constant pressure. Quasi-static analysis were performed for all the simulations and temperature was assumed uniform in the specimen. A first simulation regarded the TSR test, in which a pressure of 3000 MPa was applied to the half specimen at 60 °C to fold it into a U shape with an angle α_{prog}. The temporary U shape was fixed by cooling under the imposed shape down to -20 °C and, after constraints removal, a heating ramp up to 100 °C was applied to induce shape recovery. Numerical results are compared with experimental one in Figure 4.25a, whereas pictures of the shapes from the simulation during

the shape memory cycle are shown in Figure 4.25b together with the coordinate system and the applied boundary conditions.

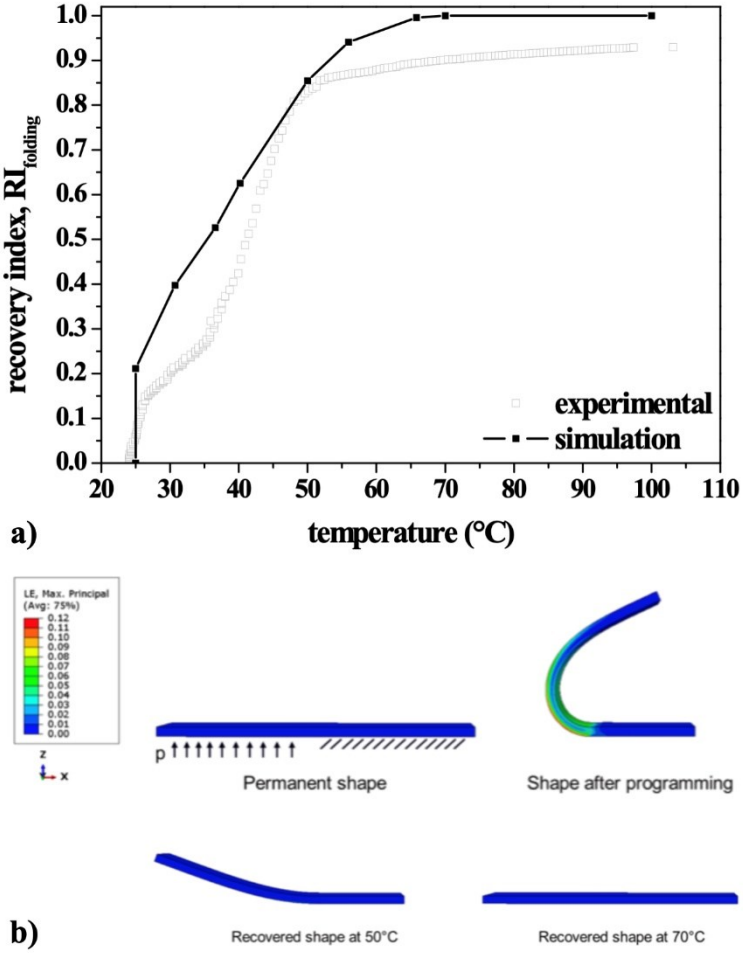

Figure 4.25. a) Comparison between experimental (grey open squares) and numerical (black full squares) recovery indexes, $RI_{folding}$, for the TSR test on bar samples obtained by HME of PVA18GLY; b) results of numerical simulations showing the contour plot of the maximum principal logarithmic strain.

A good agreement between the simulation and the experimental curves was found, even if the model slightly overpredicted the experimental recovery index for most temperatures. In fact, the model did not take into account the presence of an irreversible strain and predicted a complete recovery of the permanent shape at 70 °C, whereas the presence of a not complete recovery is a common feature for non-crosslinked semicrystalline polymers.

Furthermore, also the recovery test under isothermal conditions on a rod sample was simulated with the same coordinate system and boundary conditions shown in Figure 4.25b. The same thermo-mechanical history was applied to obtain the temporary U shape and the recovery was initiated by removing the constraints and heating at 37 °C, keeping the temperature constant for 500 min. Figure 4.26 compared the numerical results (black open squares) with the experimental ones (grey open squares).

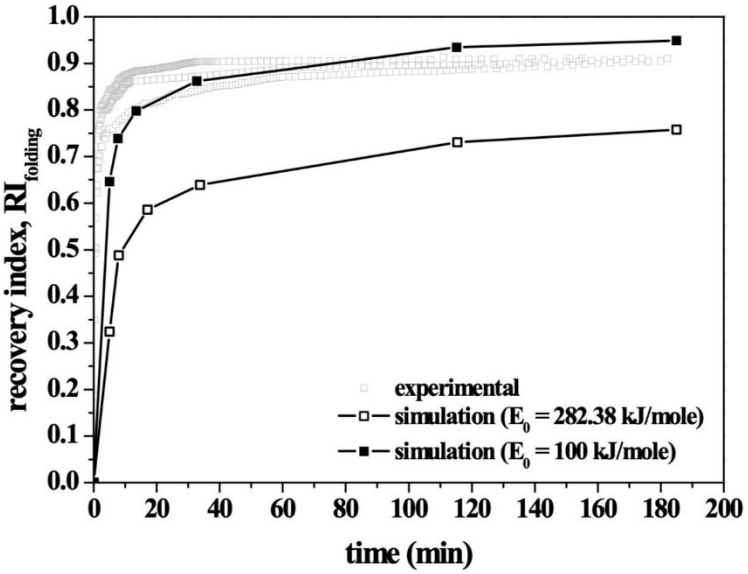

Figure 4.26. Comparison between experimental (grey open squares) and numerical (black open squares: E_0 = 282.38 kJ/mole; black full squares: E_0 = 100 kJ/mole) recovery indexes, $RI_{folding}$, for isothermal tests on rod samples obtained by HME of PVA18GLY.

In this case, even if the curves showed a similar trend with a fast increase of the recovery index in the first 20 min, the difference between numerical results and experimental ones is significant. The model underpredicted the measured recovery index resulting in a final $RI_{folding}$ of about 70% after 160 min compared to the experimentally measured 90% on average. The poor agreement found was related to the adoption of a not suitable time-temperature correlation for these recovery conditions, in which the material is inside its glass transition region. In order to improve the model accuracy and its prediction capability for the recovery of the prototype under isothermal conditions, a customized procedure was set. Because of the ease of application and implementation, the choice of the model didn't change and also the Arrhenius equation was maintained in its shape, however its calibration was done not on the shift factors data but directly on the results of the isothermal recovery test. In this way, the value of the parameter E_0 was varied until a good agreement between the

numerical and the experimental results was found, as shown in Figure 4.26, and this resulted in a E_0 equal to 100 kJ/mol (black full squares in Figure 4.26). Therefore, it was found that for this material, under these conditions of temperature in which the material response is dominated by the viscoelastic behavior, the DMA results at small strains are not enough to reliably describe the shape memory response, probably due to the complex chain motions occurring in a semicrystalline polymer, which are not considered by the model. The value of E_0 calibrated on the isothermal recovery results and used in the Arrhenius-like equation was lower than the one obtained from the shift factors used for the master curve construction. This difference can be explained considering that DMA results are related to relaxation motions of the chains taking place at small deformations in the linear viscoelastic regime, whereas the shape recovery involved larger strain, potentially belonging to a non-linear viscoelastic regime. Chain motions associated with the latter conditions may require lower activation energy on the basis of the stored internal energy and a larger free volume, in this way the lower E_0 found was tentatively explained.

On the basis of these findings, the response of the S-shaped prototype fixed in a temporary paper-clip shape was modeled. The geometry was meshed by using four-node linear tetrahedron, hybrid with linear pressure, the temperature was assumed uniform in the clip and a quasi-static analysis was performed. The desired deformation was obtained thanks to the application of a pressure and a surface-to-surface contact was employed with a 0.03 friction coefficient, enforced by linear penalty method, in order to avoid self-penetration during deformation. The temporary shape was then fixed by cooling at -20 °C; afterwards constraints were removed and the prototype was heated up to 37 °C to promote the recovery over a time window of 90 min. The comparison between numerical results and experimental ones are shown in Figure 4.27a, 4.27b and 4.27c in terms of the recovery indexes $RI_{\alpha_{xy}}$, $RI_{\alpha_{yz}}$ and $RI_{\alpha_{xz}}$ and the shapes achieved after 7 and 21 min of recovery, as predicted by the model, are represented in Figure 4.27d.

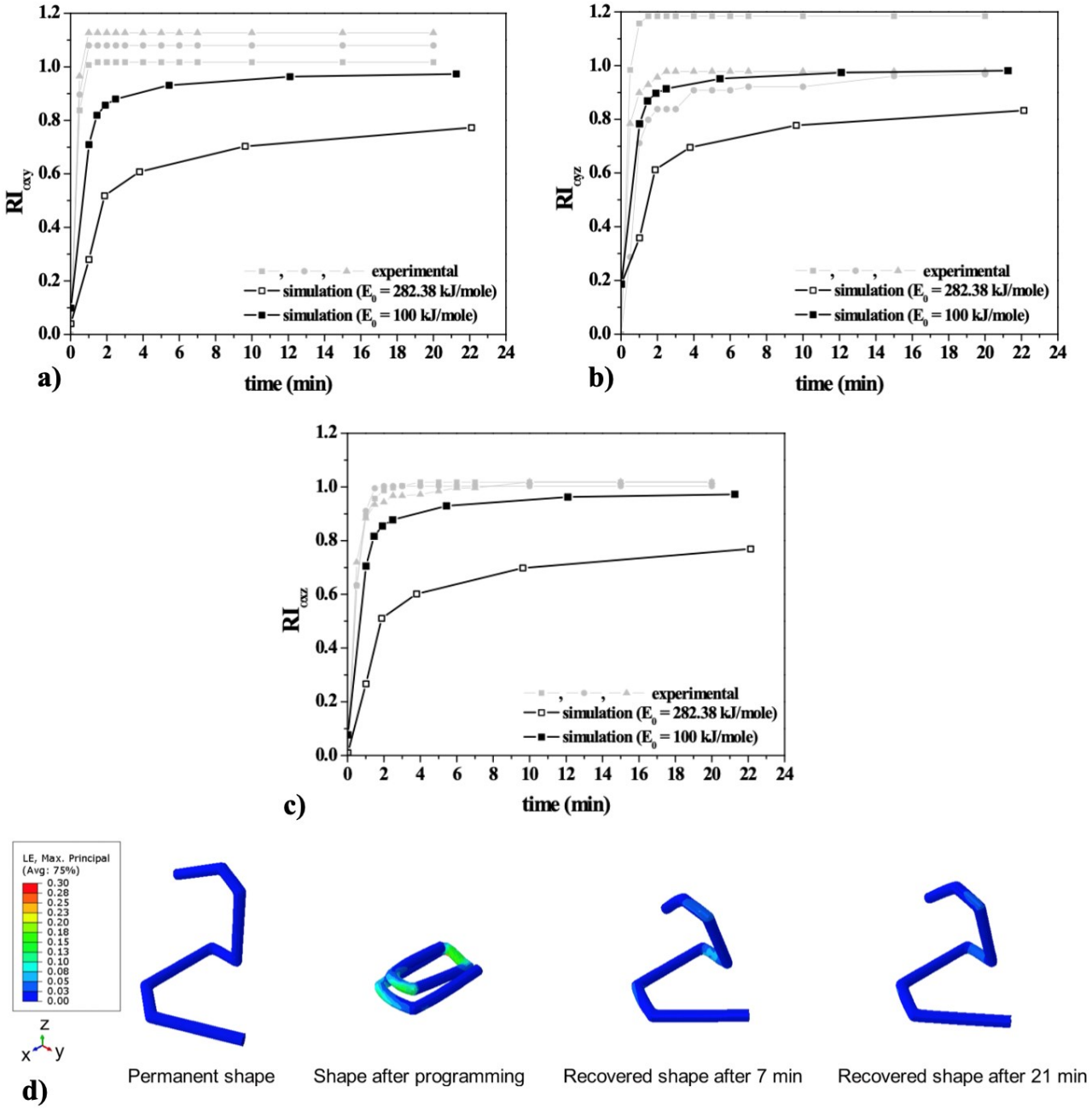

Figure 4.27. Comparison between experimental (grey full squares) and numerical (black open squares: E_0 = 282.38 kJ/mole; black full squares: E_0 = 100 kJ/mole) recovery indexes, RI, for isothermal tests on a S-shaped clip obtained by HME of PVA18GLY. Recovery Index curves: a) $RI_{\alpha,xy}$, b) $RI_{\alpha,yz}$, c) $RI_{\alpha,xz}$. d) Results of numerical simulations with E_0 = 282.38 kJ/mole, showing the contour plot of the maximum principal logarithmic strain.

The experimental results (grey full squares in Figure 4.27a, 4.27b and 4.27c) derived from the same characterization method conducted in Figure 4.16c, 4.16d and 4.16e for the drug-containing formulation, here

repeated for the formulation not containing the drug. In both cases, a very efficient shape recovery was found, in particular in the case of Figure 4.27a, 4.27b and 4.27c after 30 s the angles already reached their thresholds for gastric retention (43°, 33° and 32° for $\alpha_{xy,}$ $\alpha_{xz,}$ and α_{yz}, respectively, as already discussed for Figure 4.16c, 4.16d and 4.16e). After 3-4 min the recovery was already completed and the final recovery index values were found to be close to 100%. For some tests, the prototypes over-recovered the applied deformation with recovery indexes reaching 110-120% and this was ascribed to the presence of frozen-in-stresses and their corresponding additional deformations. By comparing the experimental results with the numerical curve obtained by using the DMTA-derived E_0 (black open square), a not suitable description of the experimental evidences was found, as expected from the case shown in Figure 4.26. In fact, the permanent shape was not recovered after 21 min, as shown in the pictures of Figure 4.27d. Therefore, the modified modeling approached was applied by using the value of 100 kJ/mol in the Arrhenius-like equation, derived from the isothermal recovery curves of the rod specimen. The numerical curve obtained (black full squares) showed a significantly improved agreement with the experimental results. To conclude, the modeling approach proposed for the simulations of gastroretentive devices with complex shapes consisted in considering E_0 as a calibration parameter, which can be optimized on the base of simple shape recovery tests on sample geometries with a significantly simplified shape and corresponding shape motions. This strategy was proved to be effective for the S-shaped device but it could be applied and extended also to other shapes and potentially to other materials, whose response cannot be described only by the employ of DMTA analyses.

4.6 References

1. E.A. Klausner, E. Lavy, M. Friedman, A.Hoffman, *J. Control. Release* 2003, 90, 143-162.
2. C.M. Lopes, C. Bettencourt, A. Rossi, F. Buttini, P. Barata, *Int. J. Pharm.* 2016, 510, 144-158.
3. A. Hoffman, D. Stepensky, E. Lavy, S. Eyal, E. Klausner, M. Friedman, *Int. J. Pharm.* 2004, 277, 141-153.
4. A.O. Nur, J.S. Zhang, Drug Dev. Ind. Pharm., 2000, 26, 965-969.
5. D.H. Altreuter, A.R. Kirtane, T. Grant, C. Kruger, G. Traverso, A.M. Bellinger, *Expert Opin. Drug Deliv.* 2018, 15, 1189-1198.
6. P.L. Bardonnet, V. Faivre, W.J. Pugh, J.C. Piffaretti, F. Falson, *J. Control. Release* 2006, 111, 1-18.
7. R. Gupta, P. Tripathi, P. Bhardwaj, A. Maho, *J. Anal. Pharm. Res.* 2018, 7, 404-410.
8. M. Kumar, D. Kaushik, *Recent Pat. Drug Deliv. Formul.* 2018, 12, 84-92.
9. E. Sabaté, Adherence to Long-Term Therapy: Evidence for Action (World Health Organization, 2003); https://www.who.int/chp/knowledge/publications/adherence_report/en/ last access in December 2020.
10. J. Chen, W.E. Blevins, H. Park, K. Park, *J. Control Release* 200, 64, 39-51.
11. E.A. Klausner, E. Lavy, M. Borta, E. Cserepes, M. Friedman, A. Hoffman, *Pharm. Res.* 2003, 20, 1466-1473.
12. H. Omidian, J.G. Rocca, K. Park, *J. Control. Release* 2005, 102, 3-12.
13. S. Verma, K. Nagpal, S.K. Singh, D.N. Mishra, *Int. J. Biol. Macromol.* 2014, 64, 347-352.
14. R.H. Laby, US3844285.
15. G.J.L. Griffin, M.D. Brewer, US4268497.
16. http://329.b67.myftpupload.com/our-therapies/, last access in December 2020.
17. A.M. Bellinger, M. Jafari, T.M. Grant, S. Zhang, H.C. Slater, E.A. Wenger, S. Mo, Y.-A.L. Lee, H, Mazdiyasni, L. Kogan, R. Barman, C. Cleveland, L. Booth, T. Bensel, D. Minahan, H.M. Hurowitz, T. Tai, J. Daily, B. Nikolic, L. Wood, P.A. Eckhoff, R. Langer, G. Traverso, *Sci. Transl Med.* 2016, 8, 1-12.
18. A.R. Kirtane, O. Abouzid, D. Minahan, T. Bensel, A.L. Hill, C. Selinger, A. Bershteyn, M. Craig, S.S. Mo, H. Mazdiyasni, C. Cleveland, J. Rogner, Y.-A.L. Lee, L. Booth, F. Javid, S. Wu, T. Grant, A.M. Bellinger, B. Nikolic B, A. Hayward, L. Wood, P.A. Eckhoff, M.A. Nowak, R. Langer, G. Traverso, *Nat. Commun.* 2018, 2294, 9: 1-12.

19. M. Verma, K. Vishwanath, F. Eweje, N. Roxhed, T. Grant, M. Castaneda, C. Steiger, H. Mazdiyasni, T. Bensel, D. Minahan, V. Soares, J.A.F. Salama, A. Lopes, K. Hess, C. Cleveland, D. J. Fulop, A. Hayward, J. Collins, S.M. Tamang, T. Hua, C. Ikeanyi, G. Zeidman, E. Mule, S. Boominathan, E. Popova, J.B. Miller, A.M. Bellinger, D. Collins, D. Leibowitz, S. Batra, S. Ahuja, M. Bajiya, S. Batra, R. Sarin, U. Agarwal1, S.D. Khaparde, N.K. Gupta, D. Gupta, A.K. Bhatnagar, K.K. Chopra, N. Sharma, A. Khanna, J. Chowdhury, R. Stoner, A.H. Slocum, M.J. Cima, J. Furin, R. Langer, G. Traverso, *Sci. Transl. Med.* 2019, 11, eaau6267.

20. X. Liu, C. Steiger, S. Lin, G.A. Parada, J. Liu, H.F. Chan, H. Yuk, N.V. Phan, J. Collins, S. Tamang, G. Traverso, X. Zhao, Ingestible hydrogel device, *Nat. Commun.* 2019, 493, 10, 1-10.

21. https://unitaid.org/assets/Lyndra-NC-September-2018.pdf, last access in December 2020.

22. https://www.fda.gov/downloads/drugs/guidances/ucm377938.pdf, last access in December 2020.

23. https://www.drugbank.ca/drugs/DB00437, last access in December 2020.

24. A. Melocchi, F. Parietti, A. Maroni, A. Foppoli, A. Gazzaniga, L. Zema, *Int. J. Pharm.* 2016, 509, 255–263.

25. J. Diani, P. Gilormini, C.Frédy, I. Rousseau, *Int. J. Solids Struct.* 2012, 49, 793–799.

26. T. Chen, O.R. Bilal, K. Shea, C. Daraio, *P. Natl. Acad. Sci. USA* 2018, 115, 5698–5702.

27. J.C. Simo, *Comput. Methods Appl. Mech. Eng.* 1987, 60, 153–173.

28. Abaqus Analysis User's Manual, ver 6.11 (2012). Dassault systemes Simulia Corp., Providence, RI.

29. O.H. Yeoh, *Rubber Chem. Technol.* 1993, 66, 745–771.

30. A. Melocchi, N. Inverarid, M. Uboldi, F. Baldi, A. Maroni, S. Pandini, F. Briatico-Vangosa, L.Zema, A. Gazzaniga, *Int. J. Pharm.* 2019, 559, 299-311.

31. H. Jaeger, D. Russmann, J. Rasper, J. Blome, Comparative study of the bioavailability and the pharmacodynamic effect of five Allopurinol preparations (author's translation, Article in German), *Arzneimittelforschung*, 1982, 32, 438-443.

32. N. Rouge, P. Buri, E. Doelker, *Int. J. Pharm.* 1996, 136, 117-139.

33. O.P. Sharma, M.V. Shah, D.C. Parikh, T.A. Mehta, *Expert Opin. Drug Deliv.* 2015, 12, 13-524.

34. N.A. Peppas, E.W. Merrill, *J. Appl. Polym. Sci.* 1976, 20, 1457-1465.

35. M.A. Kraus, M. Schuster, J. Kuntsche, G. Siebert, J. Schneider, *Glass Struct. Eng.* 2017, 2, 147–167.

Chapter 5

Design of an autonomous capsule-sized anchoring system for the gastrointestinal tract

The content of this chapter is the subject of a provisional patent application: Self-Righting Gripping-System; Inventors: Sahab Babaee, Nicoletta Inverardi, Robert Langer, Giovanni Traverso

5.1 Introduction

The gastrointestinal (GI) tract can be affected by manifold medical conditions ranging from gastrointestinal bleeding and ulcers, mucosal defects and perforations, often arising from endoscopic resection, and anastomotic leaks following gastrointestinal surgery, to name a few of them. Minimally invasive surgery (MIS) techniques can be highly advantageous to access remote areas, such as the GI tract, in order to reduce invasive procedures and their relevant adverse effects. Interesting approaches to MIS rely on the integration of novel technologies based on soft robotics to develop and optimize novel flexible endoscopic arms[1]. The development of the first bioinspired surgical octopus-like manipulators[2,3] and the design of novel deployable grasping and tissue manipulator modules based on soft fluidic microactuators and origami principles, such as the ones shown in Figure 5.1, have received huge attention[4-7].

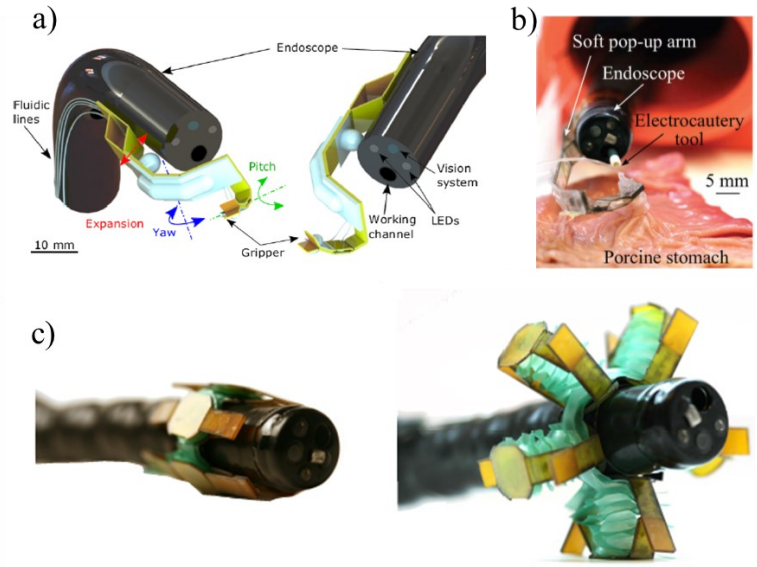

Figure 5.1. a) CAD rendering of a soft pop-up mechanism attached at the tip of the endoscope[4]; b) ex vivo test for the proof-of-concept soft pop-up arm[5]; c) origami add-ons for the tip of the endoscope before and after inflation (left and right, respectively)[6].

Clearly these systems have the potentiality of significantly improving natural orifices transluminal surgery, but simultaneously researchers are also exploring new possibilities, not requiring the use of an endoscope, inspired by the concept of "swallowing the doctor", as envisioned by Richard Feynman[8]. In fact, endoscopic capsules equipped with electronics and camera modules for diagnosis are already FDA approved and used in clinical practice to evaluate and give the physician precious information regarding region of the GI tract

otherwise difficult to access. Based on these premises, novel capsules are being developed to achieve advanced and novel functionalities, such as grasping tissue, taking biopsy and drug delivery, in the GI tract[9-13], as sketched in Figure 5.2 by Mattoli[12].

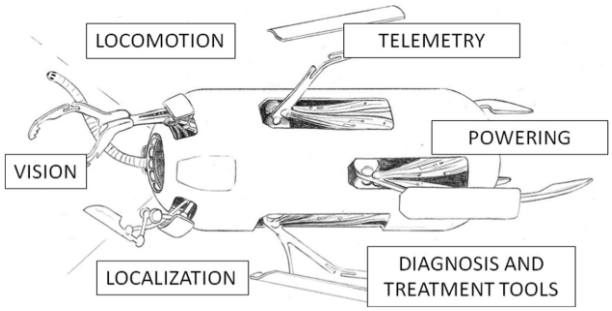

Figure 5.2. Sketch showcasing the potentialities of a robotic capsule[12].

The idea for robotic capsules is to engineer them to navigate the GI tract by exploiting an off/on adhesion mechanism to the small intestine mucosa with the final aim of taking biopsy or releasing drugs at a certain site of application. Proposed solutions concern the rational use of several different mechanisms, usually involving magnetic actuation and/or the use of shape memory alloys, triggering the deployment of legs, bioadhesive patches and blades for short-term adhesion to mucosal tissues and excision for biopsy[14-18]. Some of the suggested designs are reported in Figure 5.3.

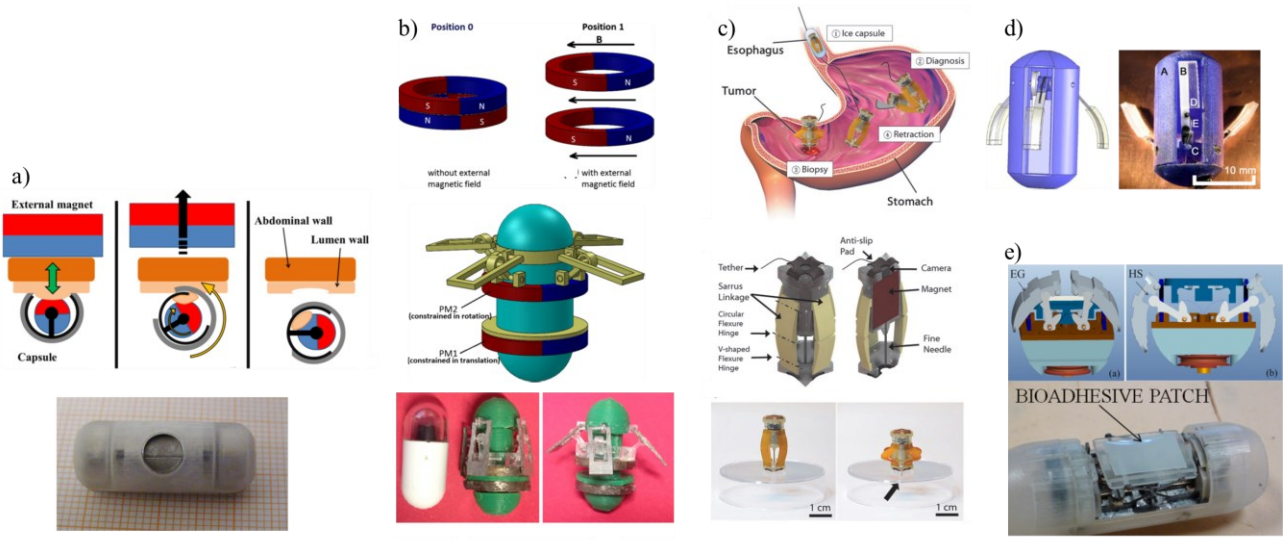

Figure 5.3. Examples of robotic capsule for navigation in the GI tract with on/off anchoring capability and/or equipped with biopsy blades and needles. a) Magnetic torsion spring mechanism proposed by Simi *et al.* for a wireless biopsy[14]. b) Magnetic springs to trigger the deployment of legs[15]. c) Robotic capsule

capable of rolling motion, collapsing motion and fine-needle biopsy actuated by a magnetic localization and actuation system[16]. d) Robotic capsule with a tri-legged anchoring mechanism having micropillar adhesives actuated by a shape memory alloy wire[17]. e) Robotic capsule for the deployment of bioadhesive patches triggered by a shape memory alloy-based release mechanism[18].

A capsule-sized system capable of gripping the stomach tissue autonomously and in a non-invasive way for long-term adhesion could be highly desirable to broaden the field of the possible applications. Actually the stomach is recognized as a very interesting target for resident biomedical devices intended for drug delivery and/or sensing applications, as widely reported[19,20]. Therefore, such an autonomous gripping system could be useful to achieve a long-term residency in the stomach, *e.g.* acting as an anchor for large drug depots or for sensors capable of recording physiological signals. Untethered gripping systems are being studied and developed focusing on a wide spectrum of expertise from materials science to mechanical design and robotics. Stimulus-responsive fingered grippers produced by photolithography on a layer of a prestressed structural metallic films or obtained from hydrogel composite systems were reported in several different designs, varying materials and actuation method[21-25]. These are tiny systems, as shown in Figure 5.4, delivered through an endoscope, mainly meant for taking biopsy.

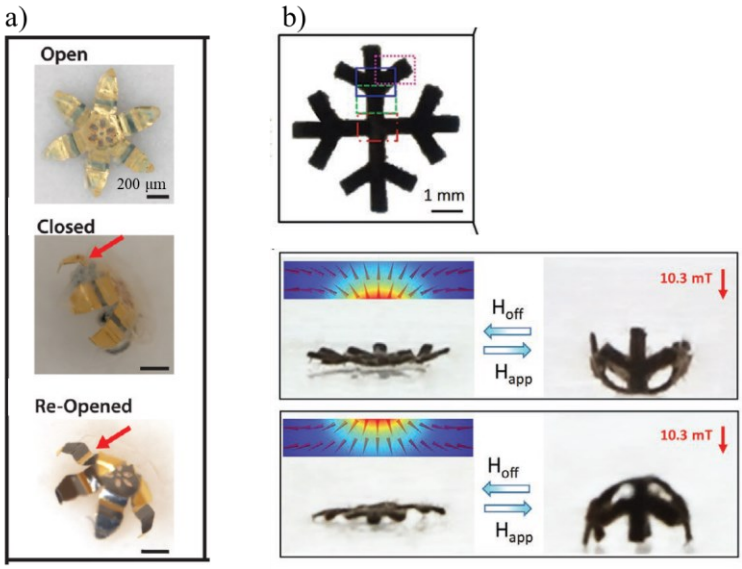

Figure 5.4. a) Outline of the shape motions features by a multilayered thin film gripper triggered on the exposure to enzymes[21]. b) Shape deformations for the hydrogel milli-gripper triggered by exposure to magnetic field (the bending direction is determined by the dipole moment direction)[25].

Very recently, these submillimeter-scale grippers, called theragrippers, were proved to be retained in the upper GI tract for up to 24 h after endoscopic administration in a porcine model and to be retained in the rectal tract up to 24 h while delivering a drug with a sustained exposure between 8 and 18 h, following intrarectal administration in a rat model. The *in vivo* efficacy of these theragrippers in large animal models was proved for temporary gripping, but not yet for prolonged residency and for simultaneously drug release[26].

Therefore, the focus of this chapter is on developing a capsule-sized device including an autonomous gripper with the aim of long-term residency in the gastric tract.

The work presented in this chapter was carried at the Massachusetts Institute of Technology as part of a research visiting period in the Langer and Traverso Laboratories (Koch Institute for Integrative Cancer Research at MIT and Department of Mechanical Engineering) in a multidisciplinary team, under a strict collaboration with Dr. Sahab Babaee, Jacob Wainer, Adam Wentworth, Declan Gwynne, Seokkee Min and Prof. Giovanni Traverso.

Results that are disclosed here in the following are the ones covered by the filed provisional application for a patent.

The support from the Bill and Melinda Gates Foundation is kindly acknowledged.

5.2 Design Concept

The challenging problem of developing an untethered capsule for anchoring and gripping the stomach tissue was in this chapter faced by a comprehensive approach based on novel design concepts for medical devices, a thorough study of the working mechanism and performances of existing ones and the exploitation of bio-inspired approaches. In fact, anchoring to the gastrointestinal (GI) tissue is already efficiently achieved by gastrointestinal parasites, such as the *Taenia solium* tapeworm, which is capable of a strong attachment to the mucosa of its host thanks to the presence of four suckers and a double crown of hooks on its head (scolex)[27], as shown in Figure 5.5. In this way, it can survive attached to the small intestine for years.

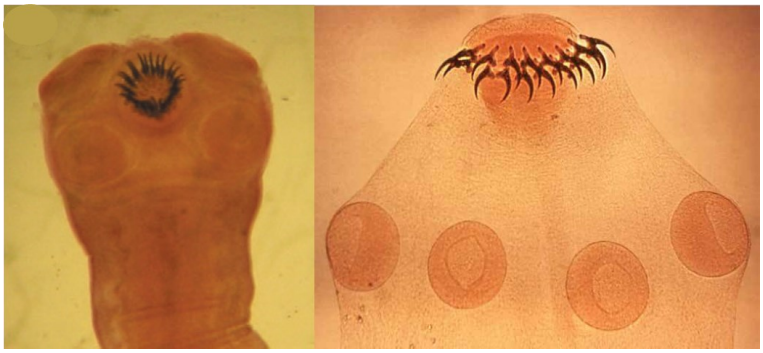

Figure 5.5. Scolex of *Taenia solium* tapeworm. As a scale bar, the diameter of the scolex is about 1-2 mm[27,28].

Attachment of a foreign body to the GI tract is also achieved during specific endoscopic procedures for which endoscopic clipping devices are deployed at the desired site of application thanks to an endoscope[29]. These clips are routinely used for the treatment of GI bleeding but also to close mucosal defects and perforation, anastomotic leaks and to mark tumor site before surgery and /or radiation therapy. Their duration of attachment at the site of application is usually about 4-5 weeks, but gastroenterologists report their retention for up to 1 year in some cases, likely due to their attachment to the submucosa and muscularis propria layers[29,30]. Especially, over-the-scope clips have been used extensively thanks to their success in the clinical practice[31,32]. These latter ones consist of a thin metallic shell that can be folded over a cap mounted at the tip of the endoscope and, in a fashion similar to the response of a bear trap, once the cap is retrieved in the proximity of the tissue to target, the device is released and it springs back to its unloaded shape while trapping, grasping and gripping the tissue[33]. Two relevant products are commercialized under the name of OVESCO OTSC® clip

(Ovesco Endoscopy AG, Tübingen, Germany) and Padlock Clip® (Steris, Mentor, OH, USA). Both the devices are produced with a Nitinol superelastic alloy and thanks to their design, shown in Figure 5.6, can be folded in a pre-loaded state, mounted over the tip of the endoscope, without causing any plastic deformation, so that they can recover their initial shape upon deployment.

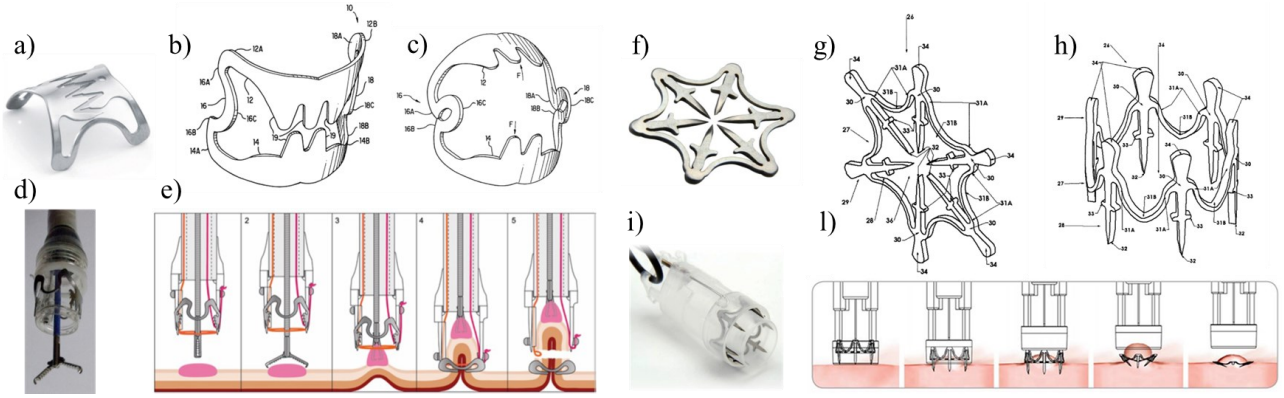

Figure 5.6. Pictures of the OTSC® clip (a) and the Padlock® clip (e), respectively in their undeformed shape (b[34] and g[35]), pre-loaded state (c[34] and h[35]), mounted over the tip of the endoscope (d[36] and i[37]). Sketch of the application of the OTSC® clip for a resection procedure[36] (e) and of the application of the Padlock® clip[37] (l).

The OTSC® clip has a curved bear claw shape with a maximum outer diameter ranging between 14.6 and 21 mm and it is characterized by the presence of several teeth, blunt or with spikes depending on the application and with different working depths (3 and 6 mm), which upon deployment compress the tissue; the Padlock® clip has a hexagonal planar shape with an outer diameter of 11 mm and it features 6 needles, 3.5 mm long, pointing towards the center and providing radial compression of the tissue.

The working mechanism for these clips together with their relevant geometrical dimensions for tissue gripping without causing any major adverse events were used as helpful guidelines to design the anchoring capsule subject of this chapter. In fact, the achievement of a strong adhesion for a device to the stomach wall may pave the way also to novel and impactful applications in the field of robotic capsule for sensing and/or extended drug delivery applications.

The following design criteria are set for the development of a novel gripping and anchoring system targeting the gastric tract:

i) easy administration without the need of the endoscope;

ii) directional gripping;

iii) autonomous activation.

Therefore, the novelty proposed in this chapter concerns the design of a capsule-sized milli-gripper device which

i) doesn't need an invasive procedure to be administered;

ii) features the presence of gripping elements;

iii) is capable of self-righting and self-orienting to provide the correct direction for the interface between the gripping elements and the tissue;

iv) is autonomously activated upon entering the stomach without the need of any tethers or external actuation systems.

5.3 Materials and Methods

The components of the capsule-sized autonomous gripper were either manufactured in-house or outsourced to vendors.

The materials used for in-house manufacturing included polycaprolactone (PCL) (M_n ~ 37,000), poly(ethylene oxide) (PEO) (M_v ~ 200,000), poly(ethylene glycol) (PEG) (M_w ~ 1,450), Kollicoat® IR, (hydroxypropyl)methyl cellulose (HPMC) (M_n ~ 86,000) and glycerol, all purchased from Sigma-Aldrich. Isomalt was purchased by VWR and Soluplus® by BASF. The silicone rubber Elite Double 8 was purchased by Zhermack SpA. Veterinary size gelatin capsules (#12EL) were purchased by Torpac. Phosphate-buffered saline, to keep the tissue moist during mechanical tests, was purchased from Gibco by Life Technologies.

Resins for 3D printing were purchased from Formlabs and Stratasys.

Nitinol superelastic and shape memory alloy sheets (transition temperatures of -15 °C and 80 °C, respectively) were purchased from Kellogg's Research Labs (Salem, NH, US) in thicknesses ranging from 0.25 mm to 0.5 mm. Nitinol solder research kit was purchased from Indium Corporation.

Muscle tissue from pig was purchased from Star Market. Stomach tissue was harvested from a Yorkshire pig right after euthanasia. Animal experiments were conducted in accordance with protocols approved by the Committee on Animal Care at the Massachusetts Institute of Technology (MIT).

The design activity was performed by using a CAD software (SolidWorks, Dassault Systèmes) and a CAE software (Abaqus, Dassault Systèmes).

Manufacturing of the customized torsion spring was commissioned to Lee Spring (Brooklyn, NY, US) using stainless steel 302 (per ASTM A313). Manufacturing of the base (housing for the spring) was commissioned to Protolabs (Maple Plain, MN, US) using stainless steel 316. Manufacturing of some needle arrays was commissioned to Potomac Photonics (Baltimore, MD, US).

3D printing of prototypes and fixtures

Prototyping of the gripper and 3D printing of plastic fixtures were performed by employing a Formlabs Form 3 printer or a Stratasys Object30 Pro printer. CAD drawings were exported in .stl and imported in the software PreForm (Formlabs) or Object Studio (Stratasys) to orient the models and, if needed, to add the support structures. The 3D printed parts were washed and post-cured, if needed, according to the manufacturer's guidelines and the support structures removed.

Microcompounding

Microcompounding of polymeric formulations was carried out by means of an Xplore twin-screw microcompounder (Xplore Instruments). A mixture of 25% Soluplus® and 75% PEO 200K and a mixture of 85% Kollicoat® IR and 15% glycerol were microcompounded at 145 °C at 50 rpm and 25 rpm, respectively. A mixture of 50% PCL 37K and 50% PEG 1450 was compounded at 65 °C at 50 rpm. The extruded filaments were then cut into pellets.

Manufacturing of the capsule

The manufacturing of the capsule was carried out by a molding-casting approach. First, the 3D models for the two halves of the capsule were modified by adding a conical sprue, *i.e.* the channel by which the material to be casted will enter inside the cavity to fill, in the CAD software (SolidWorks, Dassault Systèmes). The models were then exported as .stl files to the Preform Software (Formlabs) and 3D printed by using the Grey resin (Formlabs) with the Formlabs Form 3 stereolithography printer (Formlabs). Negative molds were then prepared by gluing the sprue of the 3D printed part to a Petri dish and pouring all around and above a two-component silicone rubber (Elite Double 8, Zhermack). After the curing of the silicone, performed at room temperature for about 30 min, the 3D printed parts were retrieved from the silicone, obtaining flexible silicone molds.

Several materials were selected to be casted using either a thermal approach or a solution casting method. Thermal casting was performed by using PCL, the blend PCL30K-PEG1450 (1:1), Isomalt and the blend

PEO200K-Soluplus®(0.75:0.25), whereas solution casting was carried out by using a commercial copolymer polyvinyl alcohol and polyethylene glycol graft (Kollicoat® IR) and HPMC. For the thermal method, pellets of the chosen polymer were poured into the rubber mold through the opening left by the sprue and heated up above their melting temperature T_m with a heat gun or by placing the mold in a lab oven. The silicone mold with the melted material inside was quickly put in a centrifuge, operated at 4000 rpm for about 10 min. After that time, the polymer was solidified inside the cavity, the part was demolded and the sprue was carefully cut off the part by using a razor blade. Likewise, for the solution casting method, Kollicoat® was dissolved in hot water (at 70 °C) by using a stirring plate and achieving a concentration of 30% wt/wt, whereas HPMC was dissolved in water at room temperature under continuous stirring at a concentration of 2% wt/wt. The solution was then poured into the sprue of the models and loaded into the centrifuge operating at 4000 rpm and these two steps were repeated few times until overfilling of the mold. The part inside the mold was let dry at air, or in a lab oven at 60 °C, for one week to enable solvent evaporation, before demolding the part and cutting the sprue. The whole fabrication method is sketched in Figure 5.10b.

Manufacturing of the needle arrays

Needle arrays were manufactured by employing subtractive manufacturing methods, such as abrasive waterjet cutting with a waterjet cutting machine (MicroMAX JetMachining Center, OMAX, available at the MIT Hobby Shop) and laser cutting. Nitinol sheets, from 0.25 to 0.5 mm thick (Kellogg's Research Labs), were used. Drawings for the needle arrays were exported as .dxf and imported in the machine software (OMAX Layout and OMAX MAKE Software) to define the cutting path using the best quality of cut. The Nitinol sheet was taped to a wood ply inside the machine bed. Once the sheet was cut, a purposely developed fixture was employed to set the sheet in a curved shape fitting the curvature of the spring arm. The fixture was designed as a two part clamping device and it was produced both by 3D printing employing the Grey resin (Formlabs) and the Formlabs Form 3 sterolithography printer and by machining Aluminum plates purchased from McMasterr-Carr with a desktop-sized milling machine (Othermill, Bantham Tools). Nitinol shape memory sheets (with transition temperature of 80°C) were deformed by placing the sheet inside the 3D printed plastic fixture, whereas superelastic Nitinol sheets were set in the deformed shape by placing them in the milled fixture

and performing a heat treatment at 500 °C for 30 min, followed by quenching in a water bath. The CAD models for the fixture and a schematic for the deformation treatment is shown in Figure 5.14.

Penetration-Retraction tests of needle arrays on tissue

The planar needle arrays, before being curved, were tested to evaluate the penetration and removal forces on gastric tissues from a Yorkshire pig. A uniaxial testing machine (Instron 5942 Series Universal Testing System) with a 50-N load cell, equipped with a grip attached to the crosshead and with a plate attached to the bottom of the machine, was used. Each needle array was clamped between the two faces of the grip in the clamping area, *i.e.* the strip area at the top of the needles, at a section 1.5 mm higher than the base of the needle. On the compression plate attached to the bottom, a purposely laser-cut acrylic plate (McMasterr-Carr) was fixed by using double-sided tape and was replaced by a new one for each test. Stomach tissue, harvested from terminal experiments at the animal facility at MIT, was cut in pieces of 1 x 1 cm^2 and glued to the acrylic plates with the inner mucosa layer exposed to the needles. The testing machine crosshead was carefully placed near to the tissue, avoiding contact and set to follow this displacement history. In the first step, it was set to move down at a rate of 1 mm/s until a maximum displacement reflecting the length of the needles (4 or 5 mm depending on the design) and taking into account possible elastic deformation of the tissue before the needle actual penetration; afterwards a period of stress relaxation was set in which the displacement was kept constant for 10 s; finally the crosshead was moved at a rate of 0.033 mm/s, up to a position about 5 mm higher than the starting one. In fact, for some needle geometries, dragging of the tissue together with the needle occurred during the retraction phase. The tissue during the testing was kept moist with PBS. Each needle geometry was tested 5 times on different pieces of tissues in order to take into account the variability and non-homogeneity of the gastric tissue. Replicates were performed also on multiple samples having the same geometry.

5.4 Preliminary results

In this section, the results related to the design activity are presented. A gripping system that is completely autonomous and administered through a capsule, without the need of an endoscope is described. The principle of its working mechanism is outlined in Figure 5.7. It consists of a multi-component system which i) can be delivered in a folded shape by simply swallowing a purposely developed capsule, without the need of an endoscope; ii) is capable of correctly lying on the stomach mucosa (step 1 in Figure 5.7) thanks to a self-orienting feature resulting from a proper distribution of weight and from a studied curvature; iii) can be actuated to unfold in a completely untethered way, by exploiting a time-dependent mechanism based on specific material kinetics dissolution inside the acid environment of the stomach iv) and grasp the tissue providing the anchor attached to the mucosa tissue (step 2 in Figure 5.7).

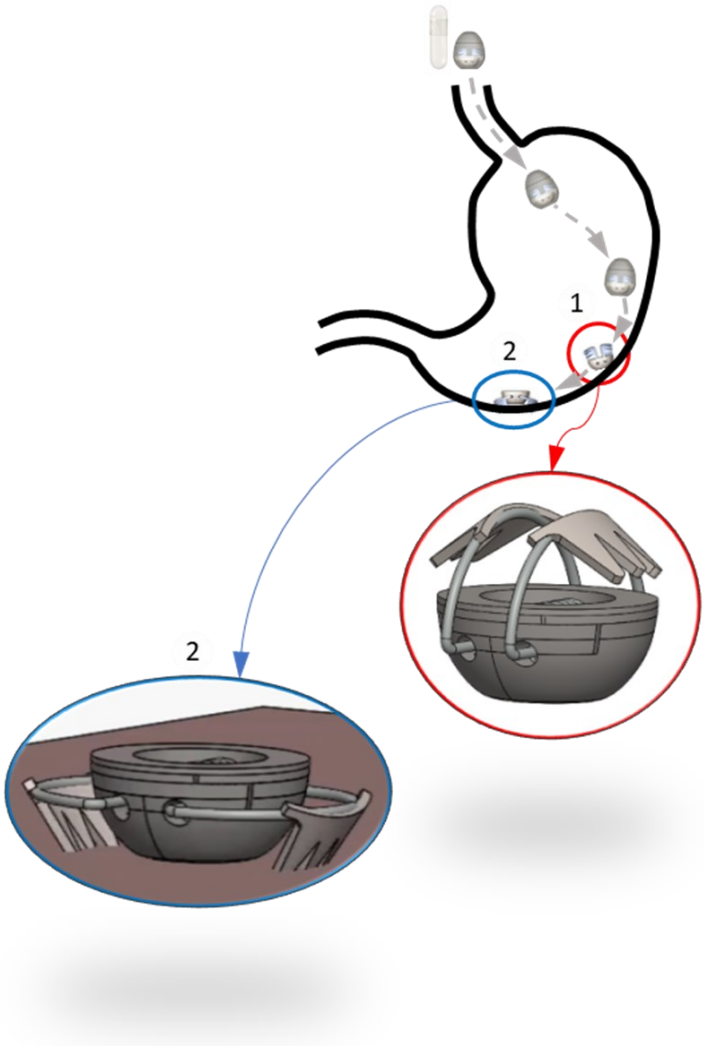

Figure 5.7. Sketch of the working mechanism for the ingestible autonomous milli-gripper. Upon ingestion, the capsule is capable to self-orient on the stomach walls (1); after dissolution of the capsule, the acidic environment triggers the deployment of the torsion spring pushing the attached needles inside the tissue to provide the gripping anchor (2).

A 3D model of the whole assembly in its configuration ready for delivery and after actuation is shown in Figure 5.8 for two different designs.

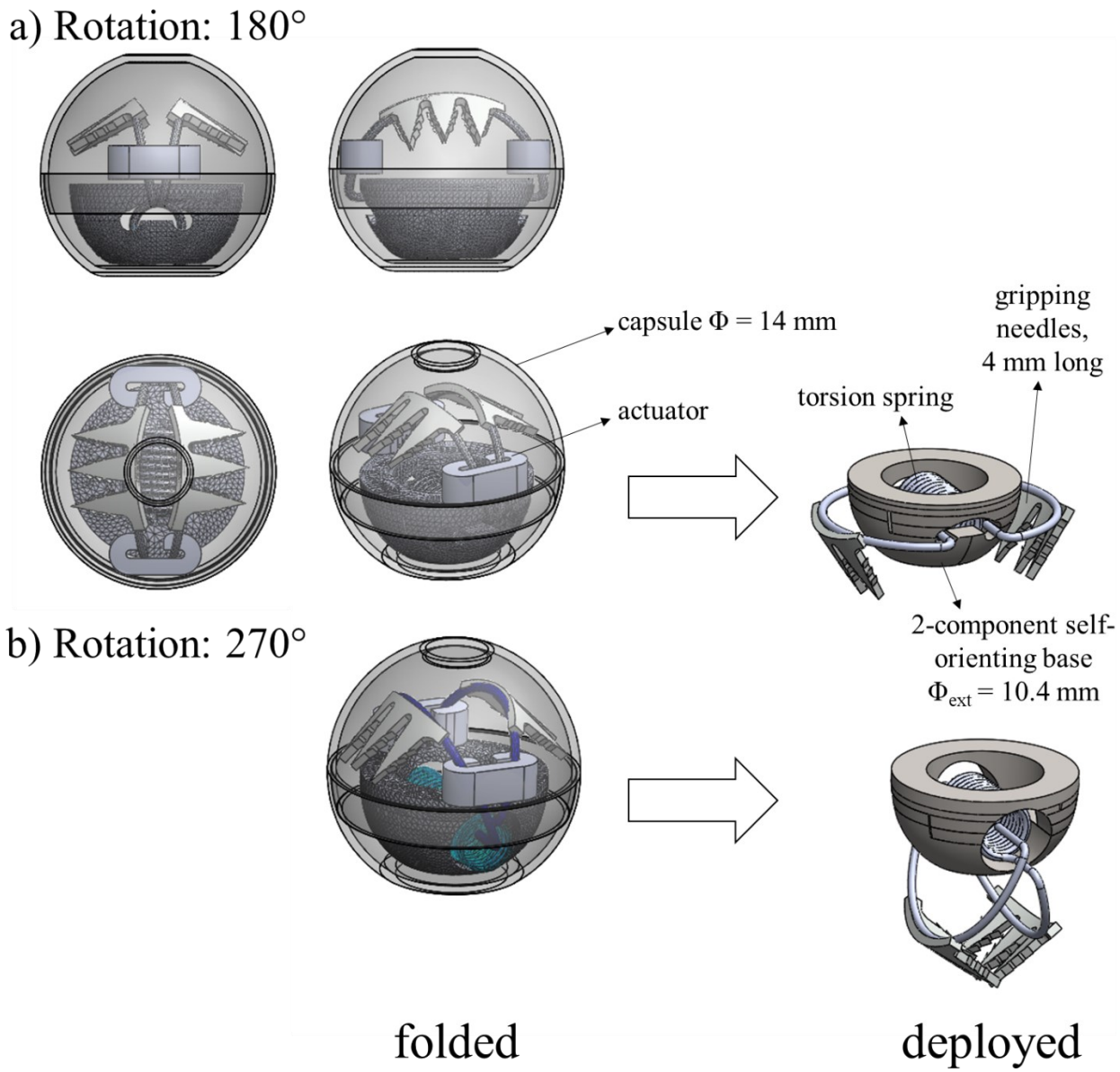

Figure 5.8. Design of the multi-component milli-gripper in two versions varying the total angle of rotation of the arms of the spring: 180° in a) (each arm rotates 90°) and 270° in b) (each arm rotates 135°). CAD

drawings are presented in the side and top views for the version a) and with a 3D view for both the versions. In the encapsulated state, the gripper has the torsion spring held vertically in a folded shape thanks to the presence of two C-shaped holders, placed on the sides. The shape of the springs in their folded configuration are predicted from finite element analysis (FEA) starting from their relevant unfolded/deployed shape (the base part is set as a discrete rigid body, *i.e.* a body that cannot deform in contact analyses, and a surface-to-surface contact was applied). After capsule dissolutions, the holding elements are triggered and release the springs which reach their deployed shape (*i.e.* their initial, as-manufactured, unfolded shape).

Both designs are composed by a thin polymeric capsule covering a stainless steel base embedding a customized torsion spring. Attached to the arms of the spring there are a pair of needle arrays characterized by micro-barbed features. The torsion spring is exploited as a mechanism to store elastic energy and it allows to fold the arm with the needles attached, by a 90° (as shown in Figure 5.8a) or 135° (as shown in Figure 5.8b) rotation for each side, in a vertical configuration, suitable for the encapsulation inside the egg-shaped capsule and thus for a safe administration *via* the oral route. Thanks to an additional holding and triggering element, the folded configuration is kept until the trigger is actuated, enabling the spring to release the stored energy and to return to its unfolded configuration. In this way, the needles attached to the spring arms are pushed inside the tissue providing a tight mechanism for anchoring the tissue. The trigger relies on the dissolution of the C-shaped holders that surround the spring arms in the folded configuration. It is designed to occur after the self-orientation of the capsule, thanks to a thickness-dependent dissolution process. The capability of correctly targeting and lying onto the stomach tissue in the direction effective for the spring deployment and hence for the gripping task is assured by a self-orienting system, modified form a self-righting element, previously developed in this research group[38].

The next paragraphs give a deeper description of each component.

Design of the self-orienting base

The self-orienting approach developed by Abramson *et al.*[38] is here exploited in order to give the device a way to control its orientation into the stomach. This feature allowed to design a unidirectional gripping system

which has needles only in the direction pointing towards the tissue. This represents an advantage for the safety profile with respect to bi- or omni-directional systems, *i.e.* with needles disposed in two or all directions, respectively. In fact needles exposed inside the organ could interfere for example with food intake or could be harmful for surrounding tissue during peristaltic wave contractions. In order to allow the assembly of the self-orienting base with the other components of the systems, the base was designed to place the torsion spring inside, and manufactured by CNC-machining (Protolabs Inc, Maple Plain, MN, US). For the design shown in Figure 5.8a, two parallel slots, with a circular cross section having 0.6 mm of radius, were cut throughout all the diameter of the base ending with four 1.2 mm diameter holes on the surface base, to obtain the space for the torsion spring arms to sit and to come outside from it. On both side, the two holes were connected with a arc-shaped slot to allow the motions of the arms during folding and unfolding. For the design shown in Figure 5.8b, a 4 mm hole was cut throughout all the diameter of the base to leave space for the spring to be folded for encapsulation and to freely deploy after capsule dissolution. For both the designs, the inner space inside the base was also machined to allow space for the coils of the spring. Finally, the bases were cut into two halves with an horizontal plane in order to allow the insertion of the spring, afterwards the base can be closed thanks to interlocking features present on the two halves and/or attached together with a medical-grade glue. The distribution of the mass was carefully checked for both the designs in order to ensure a low center of mass, that is the key feature, together with the shape of the base, to ensure the self-orienting feature.

Design of the torsion spring

A torsion spring was chosen as a robust and reliable way to store and release the elastic energy needed to fold the assembly in a compact shape for the delivery inside a capsule and capable of unfolding once in the stomach in order to release and push the needles inside the tissue. The torsion spring was designed in a customized shape with arms in the coil axial direction instead of the standard radial direction. This modification allowed to design a specific path for the arms following an arc shape, on which it is possible to mount the needle arrays.

The key design constraint to satisfy is to have a maximum safe deflection angle to fold the spring in such a way that, once the spring is released, the arms of the spring from a folded vertical configuration are capable to reach a position in contact with the underlying tissue, *i.e* the sum of both arms rotation during both folding and

unfolding has to be at least equal to 180°. This condition can be written, exploiting Castigliano's theorem, as in Equation 1

$$\beta_{max} = 64\frac{NDT_{max}}{d^4E} \geq \pi \quad (1)$$

where β_{max} is the maximum total deflection angle expressed in rad, N the number of active coils, D the diameter of the coil at the middle cross section, T_{max} the maximum torque applicable, d the wire diameter and E the Young modulus of the material. All dimensions are in the metric system.

In addition, the maximum torque that can be applied in correspondence to β_{max} is given by the spring theory, as it is reported in Equation 2

$$T_{max} = \frac{\sigma_y \pi d^3}{32 k_w} \quad (2)$$

where σ_y is the bending moment inside the fibers of the material which is equal to the yield stress of the material in the case of the maximum torque, d is the wire diameter and k_w is a stress-correction factor included to take into account the maximum stress experienced for the inner fiber of the coil and it is defined for a round wire as in Equation 3

$$k_w = \frac{4C^2 - C - 1}{4C(C-1)} \quad (3)$$

being C the ratio between the diameter of the coil D and the diameter of the wire d.

Due to the small size of the gripper, which has to be fitted inside the base and encapsulated for delivery, there exist some geometrical constraints to be satisfied for the spring, which mainly regard the coil outer diameter D_{out}, that as maximum could be equal to 3.5 mm, and the wire diameter, that has to be equal or smaller than 0.51 mm. Given these conditions and with the aim of obtaining a maximum torque suitable for pushing the needles inside the tissue, the number of coils for the two designs was obtained by satisfying Equation 1 and it was found to be 10.5 and 12.125 for a total deflection equal to 180° and 270°, respectively. A 270° total deflection was chosen since considered more promising in order to anchor the tissue in a tighter fashion, resembling the one achieved by the over-the-scope clips described in the Design Concept section.

All the parameters either used as inputs for Equation 1 and 2 or obtained as a result of the calculations are shown in Table 5.1 for the two designs considered.

	Design 1 (Figure 8a)	**Design 2** (Figure 8b)
Maximum deflection β_{max} [rad]	π	$3\pi/2$
Outer coil diameter D_{out}[mm]	3.5	3.5
Wire diameter d [mm]	0.5100	0.4318
Yield strength σ_y[MPa]	1735	1900
Number of coils	10.500	12.125
Maximum torque T_{max} [Nmm]	19.9	13.4
Maximum force at R [N]	3.3	2.2

Table 5.1. Geometrical parameters, maximum deflection, maximum torque and maximum force at the length R for the two designs. R is the moment arm and it is equal to 6 mm, *i.e.* the position in which the needle arrays are mounted, for both the designs. The Young modulus E, given the choice of a single material, is constant equal to 190 GPa.

The 3D model of the two designs and a picture of the obtained springs are shown in Figure 5.9.

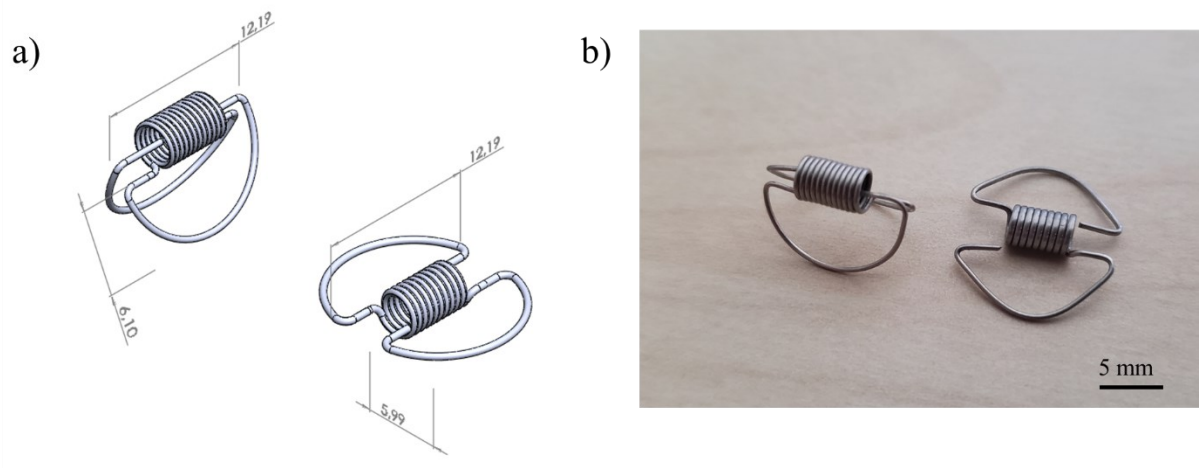

Figure 5.9. CAD drawings a) and pictures b) of the two spring designs (left: design 2 capable of 270° total deflection; right: design 1 capable of 180° total deflection). In a) only the two dimensions, in mm, relevant for fitting inside the base and the capsule, not listed in Table 1, are shown.

Design of the capsule

The capsule was designed with an egg shape to help the self-orienting feature. In fact the modifications done to the original self-orienting system[38] would have left exposed the end of the spring wire coming outside the base interrupting the curvature of the shape. The capsule was designed with a small wall-thickness (0.5mm, due to manufacturing constraints) in two parts, as shown in Figure 5.10a, and with an interlocking mechanism in order to resemble the commercially available 000 gelatin capsule. The manufacturing was carried out with a molding-casting approach, as outlined in Figure 5.10b, but it can be scaled up, by simply employing industrial manufacturing methods such as injection molding[39].

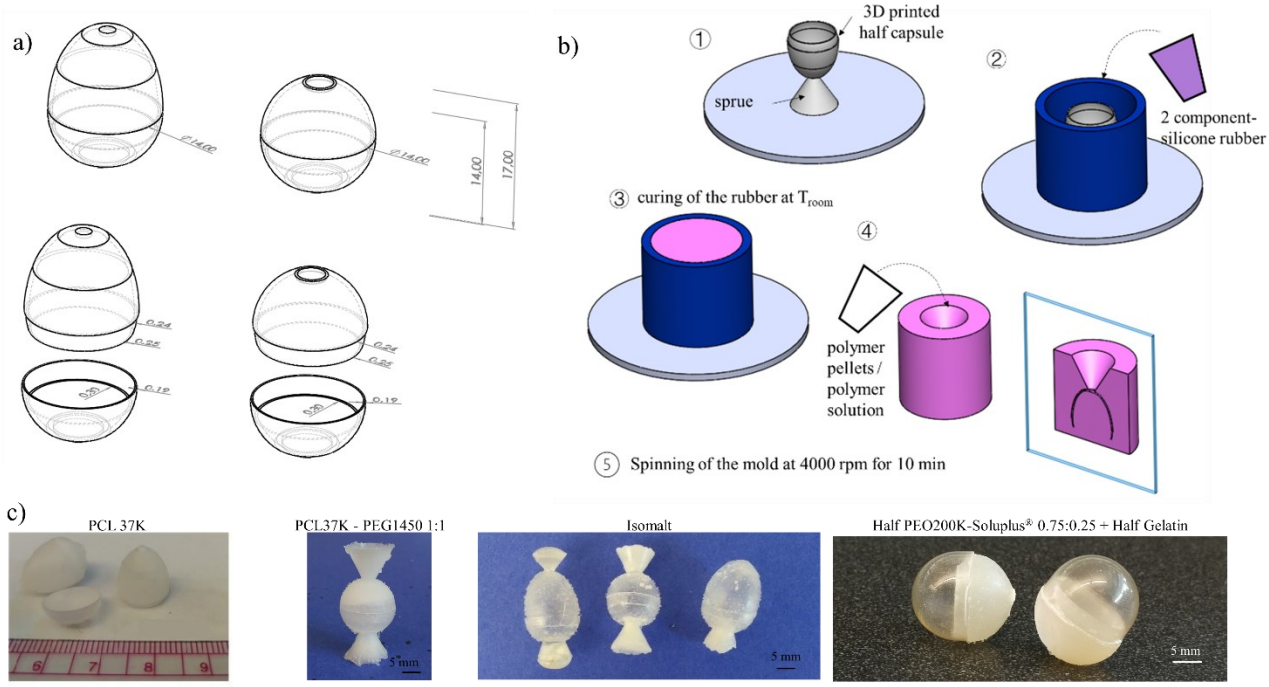

Figure 5.10. a) CAD drawings for two designs of the capsule. Dimensions are in mm. b) Sketch of the molding process: ① the capsule, modified with the attachment of a conical sprue, is 3D printed and glued to a support; ② a plastic ring (in blue) is placed around the 3D printed part and glued on the support; afterwards, a two-component silicone rubber is poured inside the space defined by the ring; ③ the rubber is left to set for approximately 30 min at room temperature T_{room}; ④ the negative rubber mold is demolded, the 3D printed part is removed from its inside and the selected material to cast is poured in the opening left by the sprue. Casting is accomplished by a thermal method by using an oven or a heat-gun or by preparing and

using a polymer solution; ⑤ the mold containing the melted material / the polymer solution is spinned inside a centrifuge at 4000 rpm for approximately 10 min.

c) Pictures of some of the casted capsules, selected from a library of materials including PCL 37K (as a control), a 1:1 blend between PCL37K and PEG1450, Isomalt, a 0.75:0.25 blend between PEO200K and Soluplus®.

Several material formulations were used for casting to find a good balance between a too quick dissolution (as in the case of isomalt), not desired since the capsule has to start dissolving only upon reaching the stomach and a too long latency period (as in the case of the long degradation for PCL) which would cause to delay the activation of the trigger. Some of the capsules obtained are shown in Figure 5.10c.

A similar casting approach based on a negative rubber mold was used also to obtain the C-shaped holder/actuator introduced in Figure 5.8, and later shown in Figure 5.15a.

Design of the needle arrays

The needle arrays are the features that come in contact with the tissue and have to penetrate it efficiently. Based on previous works inspired by the easy penetration but difficult removal characterizing porcupine quills or honeybee stingers thanks to the presence of microstructured barbs[40-43], a selection of shapes in terms of needle profile (flat, concave, with a sharp tip and with microfeatures) and needle numbers (3, 5 and 7) was produced and tested to evaluate penetration and removal forces from the tissue. CAD drawings and relevant pictures of the arrays obtained by either waterjet-cutting or laser-cutting of Nitinol thin sheets are shown in Figure 5.11.

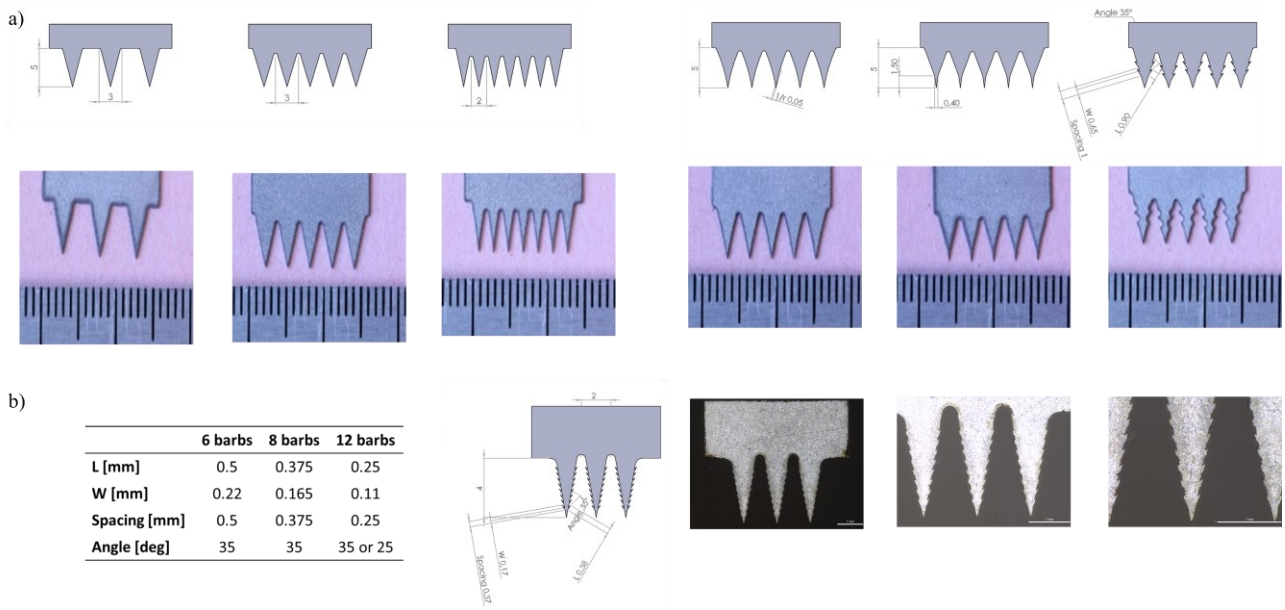

	6 barbs	8 barbs	12 barbs
L [mm]	0.5	0.375	0.25
W [mm]	0.22	0.165	0.11
Spacing [mm]	0.5	0.375	0.25
Angle [deg]	35	35	35 or 25

Figure 5.11. a) CAD drawings (top line) and pictures (bottom line) of waterjet-cut needle arrays from 0.5 mm thick shape memory Nitinol sheets. From left to right: flat profiles (with 3, 5 and 7 needles), concave profile, profile with a sharp tip and profile with microfeatures. Dimensions are in mm. b) From left to right: tables with geometrical parameter, CAD drawing and pictures taken at the microscope at different magnitudes of the laser-cut needle array.

Pig muscle tissue was used in a first test aimed at understanding the effect of the number of needles and their shape on the penetration of the needles and their removal from the tissue. The force required for penetration into the tissue for the whole length of the needles (ranging from 4 to 5 mm) was evaluated in correspondence of the peak of the force-displacement curve in the penetration ramp and it was defined as penetration force. The minimum negative force found in the force-displacement curve for the removal of the needles from the tissue was defined as pull-out force and the corresponding values are reported in the following in terms of their absolute value.

Both the penetration and pull-out force were found to increase by increasing the number of needles from 3 to 7, as shown in Figure 5.12a and 5.12b.

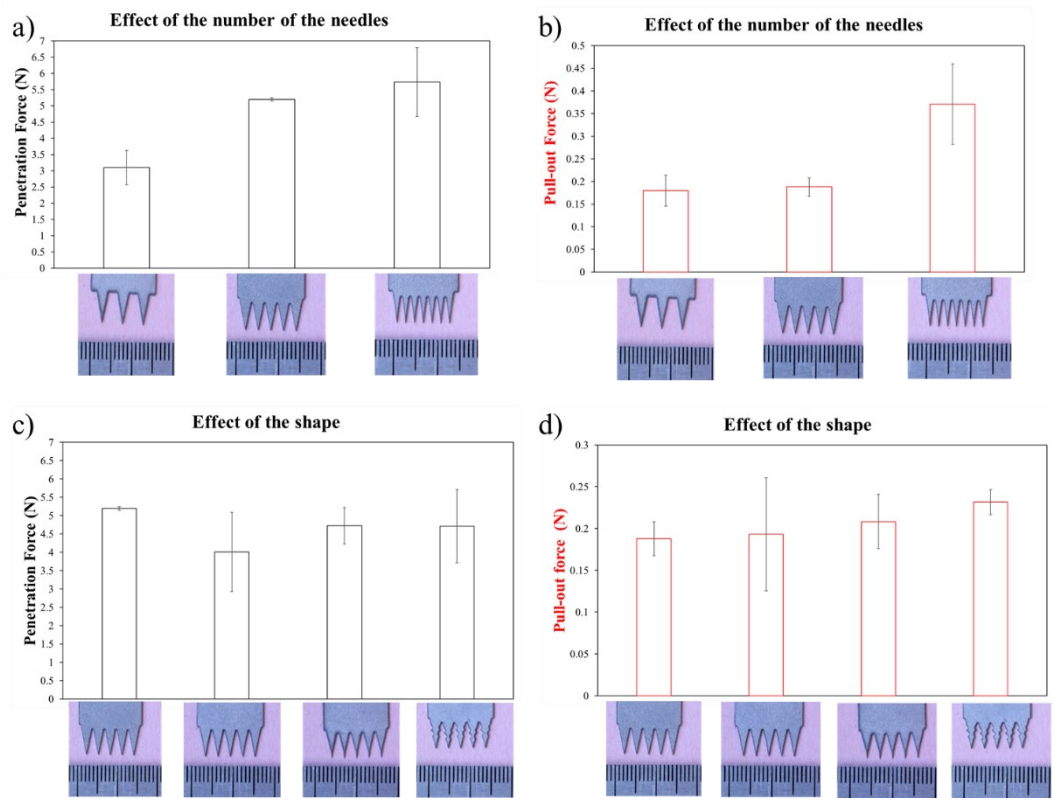

Figure 5.12. Results of the penetration/removal tests for waterjet-cut needles from 0.5 mm thick shape memory Nitinol sheets on pig muscle tissue. Penetration force a) and pull-out force b) varying the number of needles (3, 5 and 7). Penetration force c) and pull-out force d) varying shape (flat, concave, with sharp tip and with microfeatures). Tests were done on five replicates.

Conversely, the aim is to simultaneously obtain a reduced penetration force, to ease the insertion of the needles as a consequence of the deployment of the spring, and an enhanced pull-out force so as to decrease the likelihood of early detachment of the needles from the tissue. Therefore, also the various shapes were compared and the results are shown in Figure 5.12c and 5.12d in terms of the penetration force and the pull-out force, respectively. No statistical difference was found among the performances of the various shape; only a slightly increase in the pull-out force of the profile with microfeatures was obtained compared to the flat profile, not consistent with the significantly improved results of barbed-profiles reported in literature[40-43]. This response was ascribed to the low resolution of the barbed-profile obtained by waterjet cutting and therefore, laser cutting was employed in an attempt to improve the resolution of the cut.

Additional penetration and removal tests were performed on samples of stomach tissue, harvested from a Yorkshire pig, right after euthanasia, by using needle arrays with microfeatures manufactured by waterjet

cutting and by laser cutting and compared to their flat control. The results are shown in Figure 5.13a and 5.13b for waterjet-cut needles arrays featuring 5 needles and in Figure 5.13c and 5.13d for arrays featuring 3 needles.

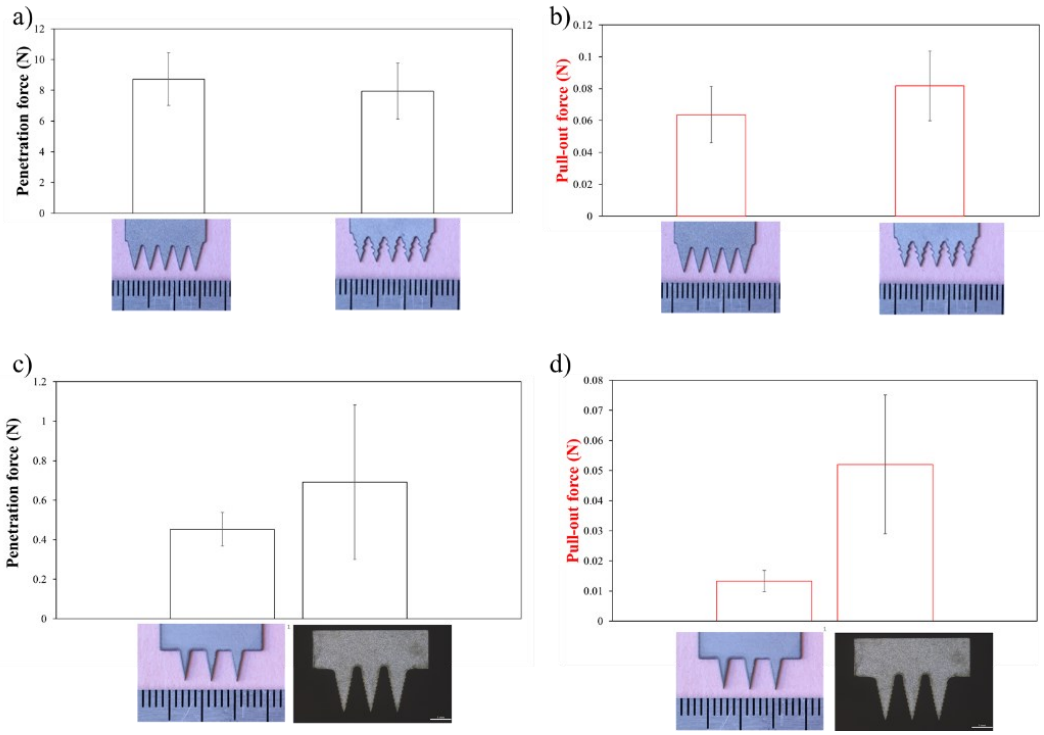

Figure 5.13. Result of the penetration/removal tests on pig stomach tissue. Penetration force a) and pull-out b) force for the waterjet-cut needle array with microfeatures compared to its control (flat profile). Penetration force c) and pull-out force d) for the laser-cut needles array with 8 microfeatures on each side compared to its control (waterjet-cut needle array with flat profile). Tests were done on five replicates

As expected, due to the low resolution of the cut for the microfeatures obtained by waterjet cutting, the pull-out force, reported in Figure 5.13b, is not shown to be significantly greater than the one evaluated for its control (flat profile). Furthermore, it is interesting to note that the penetration force needed to insert all the 5 needles inside the stomach tissue is in the order of 8 N, which is bigger than the maximum force provided by the deployment of either the springs, as evaluated in Table 5.1. Therefore, a smaller number of needles (3) is selected for the manufacturing with the laser cutter and in this way the penetration force obtained, shown in Figure 5.13c, is smaller than the one provided by the spring (being the maximum equal approximately to 3 N). Additionally, the measured value of the penetration force should be consistent with previously reported works[38], in not leading to any perforation of the tissue. Concerning the removal process, the pull-out force is found to

be increased in the laser-cut profile with microfeatures, even though improvements in the cutting process are needed in order to obtain more consistent results with less variation.

The planar needle arrays obtained by either waterjet-cutting or laser-cutting, need to be deformed into a curved shape so as to be suitable for assembly with the arc-shaped arms of the springs. The desired plastic deformation process is accomplished by using the purposely developed fixture shown in Figure 5.14.

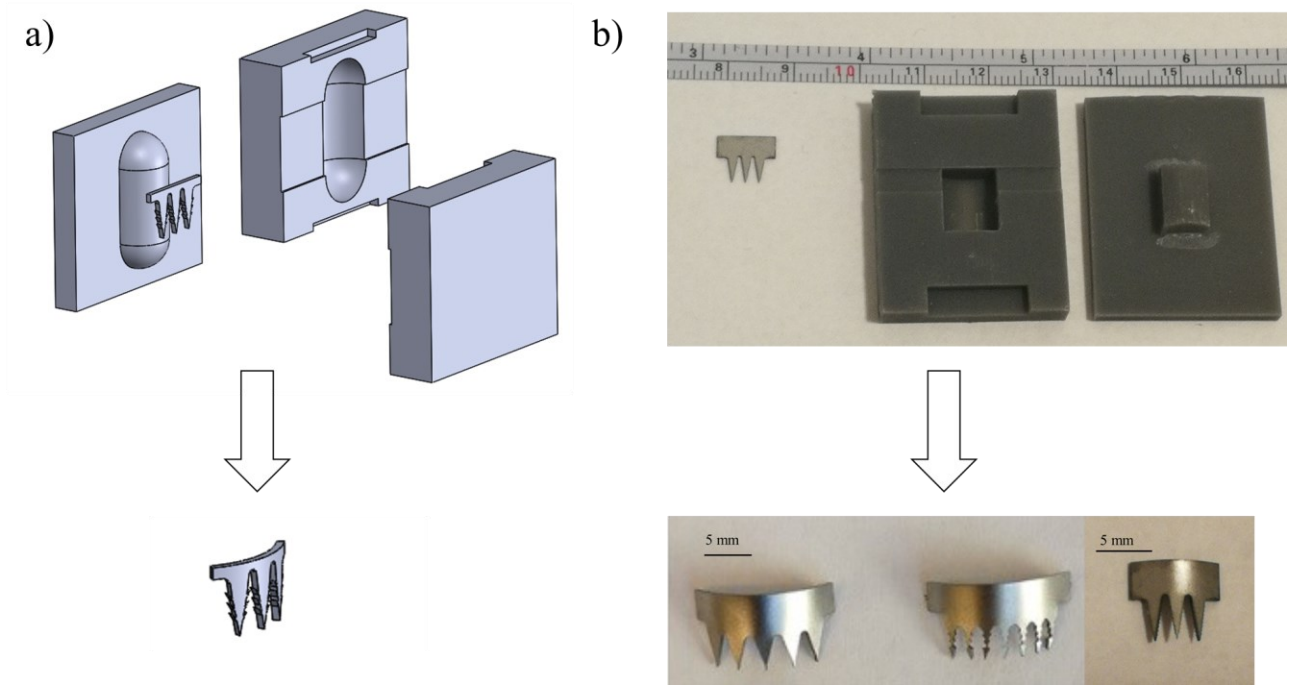

Figure 5.14. a) CAD drawing of the two-part fixture used to curve the needle arrays and outline of the deformation process. b) Picture of a 3D printed plastic fixture (top) and of some of the curved needle arrays obtained (bottom).

The fixture is obtained by either 3D printing a rigid polymeric resin or CNC-machining of an Aluminum stock, depending on the starting Nitinol sheet to be bend. In fact, if a shape memory alloy with a transition temperature significantly above room temperature is used, it is possible to set the deformed shape at room temperature by manually closing the two halves of the fixture; the resulting curve shape is maintained for temperature up to the transition one. On the contrary, when using a superelastic alloy, having its transition temperature significantly below room temperature, it is necessary to set the curve shape with a thermal treatment to be carried out at 500 °C for about 30 min, thus requiring the use of a metallic fixture.

In both ways, it is possible to obtain the curved needle arrays, as shown in Figure 5.14b, ready to be mounted over the arms of the spring. This assembly is performed by using a soldering kit which allows to achieve a strong bonding between the material of the needle arrays (Nitinol) and the one of the spring (stainless steel). The needle arrays are attached to the spring with an angle compliant to the capsule size as it was designed and presented in Figure 5.8 and shown in Figure 5.15a for one of the final prototype.

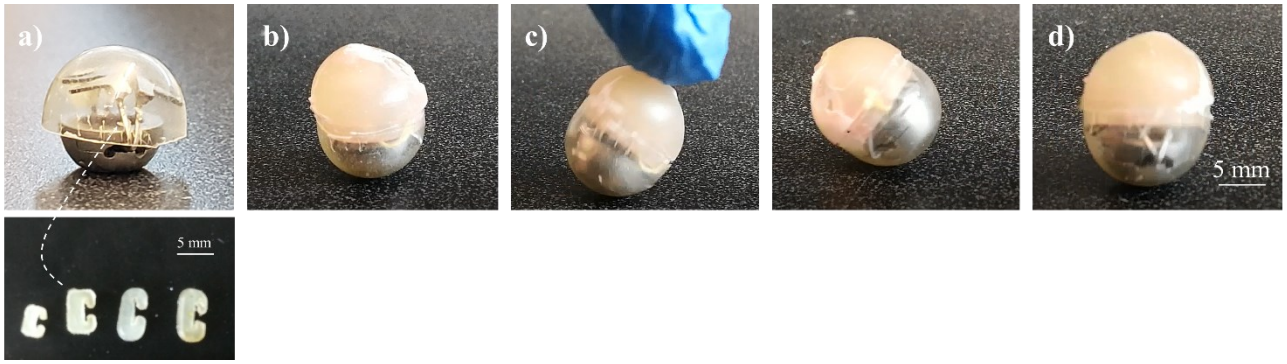

Figure 5.15. Picture of one of the prototypes for the autonomous milli-gripper, placed in a) inside a half of a gelatin capsule to show all the components (one or two C-shaped holders, shown in the bottom picture, are placed on the side to block the arms of the spring) and in b) inside a capsule bottom of gelatin and with a capsule top obtained by the blend PEO200K-Soluplus®. In c) a perturbation is applied on the top on the capsule and the gripper is shown to re-orient in its preferred orientation d).

Figure 5.15 shows pictures of the prototype including the torsion spring capable of 180° total rotation. The gripper is encapsulated and its self-orientation is proved to be effective, as the snapshots presented in Figure 5.15c and 5.15d highlight.

To conclude, the design of an autonomous capsule-sized gripper was here presented; future *in vitro*, *ex vivo* and *in vivo* testing will be performed to complete the characterization of the gripping performances.

5.5 References

1. M. Runciman, A. Darzi, G.P. Mylonas, *Soft Robot.* 2019, 6, 423-443.
2. M. Cianchetti, T. Ranzani, G. Gerboni, T. Nanayakkara, K. Althoefer, P. Dasgupta, A. Menciassi, *Soft Robot.* 2014, 1, 122-131
3. A. Arezzo, Y. Mintz, M.E. Allaix, S. Arolfo, M. Bonino, G. Gerboni, M. Brancadoro, M. Cianchetti, A. Menciassi, H. Wurdemann, Y. Noh, K. Althoefer, J. Fras, J. Glowka, Z. Nawrat, G. Cassidy, R. Walker, M. Morino, *Surg. Endosc.* 2017, 31, 264-273.
4. S. Russo, T. Ranzani, J. Gafford, C.J. Walsh, R.J. Wood, *IEEE International Conference on Robotics and Automation* 2016, 750-757.
5. S. Russo, T. Ranzani, C.J. Walsh, R.J. Wood, *Adv. Mater. Technol.* 2017, 2, 1700135.
6. T. Ranzani, S. Russo, F. Schwab, C.J. Walsh, R.J. Wood, *IEEE International Conference on Robotics and Automation* 2017, 1125-1131.
7. T. Ranzani, S. Russo, C.J. Walsh, R.J. Wood, *Proc. Of the 6th Hamlyn Symposium on Medical Robotics*, London, 2016.
8. R.P. Feynman, Plenty of Room at the Bottom, transcript of talk presented to the American Physical Society in Pasadena on December 1959, https://web.pa.msu.edu/people/yang/RFeynman_plentySpace.pdf last access on December 2020.
9. P. Valdastri, M. Simi, R.J. Webster III, *Annu. Rev. Biomed. Eng.* 2012, 14, 397-429.
10. F. Munoz, G. Alici, W. Li, *Adv. Drug Delivery Reviews* 2014, 71, 77-85.
11. J.L. Toennles, G. Tortora, M.Simi, P. Valdastri, R.J. Webster III, *Proc. IMechE, Part C: J. Mechanical Engineering Science* 2016, 224, 1397-1414.
12. G. Ciuti, R. Caliò, D. Camboni, L. Neri, F. Bianchi, A. Arezzo, A. Koulaouzidis, S. Schostek, D. Stoyanov, C.M. Oddo, B. Magnani, A. Menciassi, M. Morino, M.O. Schurr, P. Dario, *J Micro-Bio Robot* 2016, 11, 1-18.
13. C. Steiger, A. Abramson, P. Nadeau, A.P. Chandrakasan, R. Langer, G. Traverso, *Nature Reviews Materials* 2019, 4, 83-98.
14. M. Simi, G. Gerboni, A. Menciassi, P. Valdastri, *J. Med. Devices*, 2013, 7, 041009.
15. H. Zhou, G. Alici, F. Munoz, *Biomed. Microdevices,* 2016, 18, 102

16. D. Son, H. Gilbert, M. Sitti, *Soft Robot.*, 2020, 7, 10-21.
17. P. Glass, E. Cheung, M. Sitti, *IEEE Transactions on Biomedical Engineering*, 2008, 55, 2759-2267.
18. C. Quaglia, S. Tognarelli, E. Sinibaldi, N. Funaro, P. Dario, A. Menciassi, *J. Med. Devices*, 2014, 8, 014503.
19. E.A. Klausner, E. Lavy, M. Friedman, A.Hoffman, *J. Control. Releas*e 2003, 90, 143-162.
20. D.H. Altreuter, A.R. Kirtane, T. Grant, C. Kruger, G. Traverso, A.M. Bellinger, *Expert Opin. Drug Deliv.* 2018, 15, 1189-1198.
21. N. Bassik, A. Brafman, A.M. Zarafshar, M. Jamal, D. Luvsanjav, F.M. Selaru, D.H. Gracias, *J. Am. Chem. Soc.* 2010, 132, 16314-16317.
22. K. Malachowski, J. Breger, H.R. Kwag, M.O. Wang, J.P. Fisher, F.M. Selaru, D.H. Gracias, *Angew. Chem. Int. Ed.* 2014, 53, 8045 –8049
23. J.C. Breger, C. Yoon, R. Xiao, H.R. Kwag, M.O. Wang, J.P. Fisher, T.D. Nguyen, D.H. Gracias, *ACS Appl. Mater. Interfaces* 2015, 7, 3398−3405.
24. K. Kobayashi, C. Yoon, S.H Oh, J.V. Pagaduan, D.H. Gracias, *ACS Appl. Mater. Interfaces* 2019, 11, 151−159.
25. S.R. Goudu, I.C. Yasa, X. Hu, H. Ceylan, W. Hu, M. Sitti, *Adv. Funct. Mater.* 2020, 30, 2004975.
26. A. Ghosh, L. Li, L. Xu, R.P. Dash, N. Gupta, J. Lam, Q. Jin, V. Akshintala, G. Pahaple, W. Liu, A. Sarkar, R. Rais, D.H. Gracias, F.M. Selaru, Sci. Adv. 2020, 6, eabb4133.
27. H. H. García, A. E. Gonzalez, C. A. W. Evans, R. H. Gilman; Cysticercosis Working Group in Peru, Taenia solium cysticercosis. Lancet 362, 547–556 (2003).
28. Centers of Disease Control https://phil.cdc.gov/Details.aspx?pid=5262 last access in December 2020.
29. Technology Status Evaluation Report, prepared by Technology Assessment Committee, Gastrointestinal Endoscopy 2006, 63, 746-750.
30. E.J. Shin, C.-W. Ko, P. Magno, S.A. Giday, J.O. Clarke, J.M. Buscaglia, G. Sedrakyan, S.B. Jagannath, A.N. Kalloo, S.V. Kantsevoy, Gastrointestinal Endoscopy 2007, 66, 757-761.
31. D. Cheriyan, R. Enns, Gastrointestinal Endoscopy 2014, 80, 623-625.
32. A. Schmidt, S. Gölder, M. Goetz, A. Meining, J. Lau, S. von Delius, M. Escher, A. Hoffmann, R. Wiest, H. Messmann, T. Kratt, B. Walter, D. Bettinger, K. Caca, *Gastroenterology* 2018, 155, 674-686.

33. E. Armellini, S.F. Crinò, M. Orsello, M. Ballarè, R. Tari, S. Saettone, F. Montino, P. Occhipinti, *World J. Gastroenterol.* 2015, 21, 13587-13592.
34. R.F. Durgin, M.O. Schurr, G. Buess, B. Vogel, H. Fischer, US6428548B1.
35. D. LaBombard, US9408594B2.
36. A. Schmidt, T. Beyna, B. Schumacher, A. Meining, H.-J. Richter-Schrag, H. Messmann, H. Neuhaus, D. Albers, M. Birk, R. Thimme, A. Probst, M. Faehndrich, T. Frieling, M. Goetz, B. Riecken, K. Caca, *Gut* 2018, 67, 1280-1289.
37. https://www.steris.com/healthcare/products/endoscopy-devices/gi-bleed-management-and-irrigation/padlock-clip-defect-closure-system last access in December 2020.
38. A. Abramson, E. Caffarel-Salvador, M. Khang, D. Dellal, D. Silverstein, Y. Gao, M. Revsgaard Frederiksen, A. Vegge, F. Hubálek, J.J. Water, A.V. Friederichsen, J. Fels, R. Kaae Kirk, C. Cleveland, J. Collins, S. Tamang, A. Hayward, T. Landh, S.T. Buckley, N. Roxhed, U. Rahbek, R. Langer, G. Traverso, *Science* 2019, 363, 611-615.
39. L. Zema, G. Loreti, A. Melocchi, A. Maroni, A. Gazzaniga, *J. Contol. Release* 2012, 159, 324-331.
40. W. Kyung Cho, J.A. Ankrum, D. Guo, S.A. Chester, S. Yun Yang, A. Kashyap, G.A. Campbell, R.J. Wood, R.K. Rijal, R. Karnik, R. Langer, J.M. Karp, *P. Natl. Acad. Sci. USA* 2012, 109, 21289-21294.
41. J. Ling, Z. Song, J. Wang, K. Chen, J. Li, S. Xu, L. Ren, Z. Chen, D. Jin, L. Jiang, *J. Mech. Beah. Biomed.* 2017, 68, 173-179.
42. Z. Cheng, Y. Lin, W. Lee, L. Ren, B. Liu, L. Liang, Z. Wang, L. Jiang, *ACS Appl. Mater. Interfaces* 2018, 10, 29338−29346.
43. D. Han, R.S. Morde, S. Mariani, A.A. La Mattina, E. Vignali, C. Yang. G. Barillaro, H. Lee, *Adv. Funct. Mat.* 2020, 30, 1909197.

Conclusions

In this PhD thesis, 3D printed shape memory polymers were studied in depth with specific attention to their potential applications in the biomedical field. The research can be placed in the framework of 4D printing, a novel research field interested in the manufacturing by 3D printing of smart active materials, capable of changing their shape over time, which represents the fourth dimension in the terminology related to 4D printing.

In particular, in this work special attention was devoted to the investigation, characterization and exploitation of complex shape changes pertaining to the response of stimulus-responsive materials and to time-dependent actuation mechanisms. This topic was thoroughly developed under three perspectives, here described.

First, in Chapter 2, 3D printing of shape memory polymers was approached from a materials science point of view in order to gain insight on a non-conventional shape memory effect enabling complex shape transformations. Sequential shape-shifting motions were achieved in a novel way by leveraging a purposely developed thermo-mechanical protocol based on specific material properties. This strategy was proved to be effective for self-locking and self-deployable structures and meta-structures, with potentiality to be further investigated for the design of novel metamaterial-based devices, such as stents.

Secondly, tailored shape changes were identified and purposely designed to develop novel solutions for the biomedical field, especially for drug delivery applications. The work performed was the first example for the application of a 4D printing approach to the design of novel pharmaceutical platforms, by demonstrating its feasibility in proof-of-concept prototypes. The approach was developed for a retentive intravesical drug delivery device in Chapter 3, whereas its exploitation for the design of a gastroretentive device was presented in Chapter 4. The shape memory effect in both cases is helpful to administer the device in a compact shape and to achieve retention capability inside the target organ, as a consequence of the programmed shape changes triggered by physiological stimuli.

Finally, an autonomous deployable device was designed in Chapter 5 as a multi-material, multi-component assembly, in which each element accomplishes a task, including autonomous activation thanks to a time-dependent dissolution mechanism. The deployable device was conceived for a specific application scenario, in order to fulfil the unmet need of a long-term residence system capable of gripping and acting as an anchor in the gastrointestinal tract. Disclosed results are covered by a provisional patent application.